Development of Shallow Viscous Oil Reserves in North Slope

ID Number: DE-FC26-01BC15186

Final Report

Reporting Period Start Date: 9-25-2001

Reporting Period End Date: 9-24-2004

Submitted to the

U.S. Department of Energy

Kishore K. Mohanty

Department of Chemical Engineering

University of Houston

4800 Calhoun Road

Houston, Texas 77204-4004

December, 2004

Disclaimer

Abstract

North Slope of Alaska has huge oil deposits in heavy oil reservoirs such as Ugnu, West Sak and Shrader Bluff etc. The viscosity of the last two reservoir oils vary from ~30 cp to ~3000 cp and the amount in the range of 10-20 billion barrels. High oil viscosity and low formation strength impose problems to high recovery and well productivity. Water-alternate-gas injection processes can be effective for the lower viscosity end of these deposits in West Sak and Shrader Bluff. Several gas streams are available in the North Slope containing NGL and CO_2 (a greenhouse gas). The goal of this research is to develop tools to find optimum solvent, injection schedule and well-architecture for a WAG process in North Slope shallow sand viscous oil reservoirs.

Coreflood, quarter 5-spot study, compositional simulation, wettability, relative permeability study and streamline-based simulation were conducted in this project. 1D compositional simulation results agree reasonably well with those of the slim tube experiments. Injection of CO2-NGL is preferable over that of PBG-NGL. MME is sensitive to pressure (in the range of 1300-1800 psi) for the injection of PBG-NGL, but not for CO2-NGL. Three hydrocarbon phases form in this pressure range. As the mean thickness of the adsorbed organic layer on minerals increases, the oil-water contact angle increases. The adsorbed organic films left behind after extraction of oil by common aromatic solvents used in core studies, such as toluene and decalin, are thinner than those left behind by non-aromatic solvents, such as cyclohexane. The force of adhesion for minerals aged with just the asphaltene fraction is similar to that of the whole oil implying that asphaltenes are responsible for the mixed-wettability in this reservoir. A new relative permeability model for a four-phase, mixed-wet system has been proposed. A streamline module is developed which can be incorporated in an existing finite-difference based compositional simulator to model water flood, gas flood and WAG flood.

Horizontal wells increase well deliverability over vertical wells, but sweep efficiency can decrease. The well performance depends on the well length, position, heterogeneity, and viscosity ratio. The productivity increase due to electromagnetic heating is a function of power intensity, flow rate, and frequency etc. The productivity of a well can be doubled by electromagnetic heating. A high-pressure quarter 5-spot model has been constructed to evaluate the sweep efficiency of miscible WAG floods. WAG displacement reduces bypassing compared to gas floods and improves oil recovery in cores. As the WAG ratio decreased and slug size increased, oil recovery increased. Oil was recovered faster with increased slug size and decreased WAG ratio in the simulations for field cases studied.

TABLE OF CONTENTS

List of Graphical Materials

Page

Executive Summary

North Slope of Alaska has huge oil deposits in heavy oil reservoirs such as Ugnu, West Sak and Shrader Bluff etc. The viscosity of the last two reservoir oils vary from ~30 cp to ~3000 cp and the amount in the range of 10-20 billion barrels. High oil viscosity and low formation strength impose problems to high recovery and well productivity. Water-alternate-gas injection processes can be effective for the lower viscosity end of these deposits in West Sak and Shrader Bluff. Several gas streams are available in the North Slope containing NGL and CO_2 (a greenhouse gas). The goal of this research is to develop tools to find optimum solvent, injection schedule and well-architecture for a WAG process in North Slope shallow sand viscous oil reservoirs.

Coreflood, quarter 5-spot study, compositional simulation, wettability, relative permeability study and streamline-based simulation were conducted in this project. 1D compositional simulation results agree reasonably well with those of the slim tube experiments. Injection of CO2-NGL is preferable over that of PBG-NGL. MME is sensitive to pressure (in the range of 1300-1800 psi) for the injection of PBG-NGL, but not for CO2-NGL. Three hydrocarbon phases form in this pressure range. As the mean thickness of the adsorbed organic layer on minerals increases, the oil-water contact angle increases. The adsorbed organic films left behind after extraction of oil by common aromatic solvents used in core studies, such as toluene and decalin, are thinner than those left behind by non-aromatic solvents, such as cyclohexane. The force of adhesion for minerals aged with just the asphaltene fraction is similar to that of the whole oil implying that asphaltenes are responsible for the mixed-wettability in this reservoir. A new relative permeability model for a four-phase, mixed-wet system has been proposed. A streamline module is developed which can be incorporated in an existing finite-difference based compositional simulator to model water flood, gas flood and WAG flood.

Horizontal wells increase well deliverability over vertical wells, but sweep efficiency can decrease. The well performance depends on the well length, position, heterogeneity, and viscosity ratio. The productivity increase due to electromagnetic heating is a function of power intensity, flow rate, and frequency etc. The productivity of a well can be doubled by electromagnetic heating. A high-pressure quarter 5-spot model has been constructed to evaluate the sweep efficiency of miscible WAG floods. WAG displacement reduces bypassing compared to gas floods and improves oil recovery in cores. As the WAG ratio decreased and slug size increased, oil recovery increased. Oil was recovered faster with increased slug size and decreased WAG ratio in the simulations for field cases studied.

Introduction

North Slope of Alaska has huge oil deposits in heavy oil reservoirs such as Ugnu, West Sak and Shrader Bluff etc (Foerster et al., 1997). These reservoirs overlie existing productive reservoirs such as Kuparak and Milne Point. The viscosity of the West Sak and Shrader Bluff oils vary from ~30 cp to ~3000 cp and the amount is approximately 16 billion barrels. High oil viscosity and low formation strength impose problems to high recovery and well productivity. These challenging reservoirs are the largest undeveloped accumulations in North America. With even modest recoveries, reserves must be considered substantial (a few billion barrels).

Waterflood pilots have been attempted in both West Sak starting in 1984 and Shraeder Bluff in 1991 (Bidinger & Dillon., 1995). Initial well productivity of approximately 300 BOPD in a ~19 API oil is considered low by North Slope standards. The goal of this research is develop the new technology to increase the well productivity as well as the reservoir recovery efficiency. Water-alternate-gas injection processes and modern well architectures can be effective in recovery of the low viscosity (<100 cp) of these deposits in West Sak and Shredder Bluff. Several gas streams are available for the WAG process in the North Slope that contain NGL and CO_2. The disposal of (a few trillion cubic feet of) CO_2 will be an added benefit because CO_2 is a greenhouse gas and the sequestration of a significant amount of greenhouse gas is a challenge for the mankind in the twenty first century.

This report summarizes our results for the period of September 2001 through September 2004. The five tasks for the project are: (1) Compositional model, (2) Relative permeability, (3) Reservoir simulator, (4) Well Architecture, and (5) WAG optimization. The activities are described in the next section.

Experimental

Materials

Core. A Berea core was used to perform linear WAG floods. The core had a porosity of about 18% and a permeability of about 116 mD. The core properties are shown in Table 1.

Core				
	D (cm)	5.050	A (cm^2)	20.03
	L (cm)	25.100	V (cm^3)	502.74
N2	K (md)	386.59	V_p (cm^3)	91.00
Brine	K (md)	116.34	ϕ	18.10

Table 1 – Properties of the Berea core.

Oil. A dead crude oil was obtained from the Shraeder Bluff reservoir. Live oil was prepared in our laboratory by adding methane with a live oil viscosity of about 50 cp.

Solvent. The solvent was prepared in such a way that its composition is the same as the mixture of 50% NGL (natural gas liquid) with 50% PBG (Prudhoe Bay Gas). This fluid is multi-contact miscible from slimtube and simulation studies. The composition of the solvent is shown in Table 2.

Component	Mol %
CO2	6.09
C1	38.29
C2	3.12
C3	3.76
C4	22.24
C5	12.88
C6	3.10
C7	3.10
C8	3.71
C10	3.71

Table 2 – Composition of gas solvent.

Substrates. Silicon and mica were used as two different substrates in our wettability experiments. Both mica and silicon surfaces are atomically smooth and well suited for AFM imaging. Silicon was used because silica is a major component of sandstones. Being alumino silicate, mica has properties similar to clay minerals in sandstones. Mica, obtained from Ted Pella Inc. was in the form of slip disks of diameter 9 mm. Silicon, obtained from Silicon Inc. as wafers of 20 cm in diameter with a single polish side of 2.4 μm thick SiO_2 layer, was cut to small (10 mm) square plates. These substrates were glued on 15 mm metal disks for AFM imaging and contact angle measurements.

Chemicals. Distilled, de-ionized water was passed through Milli Q cartridge filters to obtain water of resistivity 18.2 MΩ/cm and pH 7. This ultra pure water was used to prepare synthetic brine. Toluene, decalin, cyclohexane, methanol and isopropyl alcohol, obtained from Mallinckrodt, Sigma Aldrich, and EM Science, were used without any further purification. Two different reservoir oils, designated as Crude A (Shraeder Bluff) and Crude B were used for wettability tests.

Procedure

Treatment of substrates with crude oils. Mica/Silicon substrates were first immersed in synthetic brine for 24 hours. After removal from brine, most of the water on the surface of the substrate was removed by using a tissue to withdraw water at the edge of the sample. Care was taken to ensure that the tissue did not touch the mica or silicon surface and that the tissue papers did not have any surfactant. The substrate was then immersed in oil and aged in oil for 7 days at approximately 80^{o}C. The aging was carried out in a closed container at an elevated temperature to enhance the kinetics of adsorption of crude oil components. After aging in oil, the substrate was rinsed by dipping it in a solvent for a few minutes. Three different solvents were tested:

toluene, decalin and cyclohexane. The substrate was subjected to 3 different solvent washings for about 10 minutes each. It was seen that after around 30 minutes no adsorbed oil was visible to naked eye.

In order to remove the excess solvent, two different methods were followed which are designated as “dry mode” and “wet mode”. For the dry mode, the sample was air dried for a day to evaporate away the solvent (Buckley & Lord, 2003) and then imaged with the AFM. It was observed under an optical microscope that as the sample dried, there were some changes in the appearance of the surface. In order to avoid these drying effects, we followed another procedure called the “wet mode”. In the wet mode, the substrate after treatment with the solvent was rinsed with IPA followed by methanol and finally by water. Care was taken not to let the sample dry at any point of time. The samples were scanned under water (not brine) to avoid salt deposition on the cantilever tip.

Treatment of substrates with SARA Fractions. The SARA fractions (Saturates/Aromatics/Resins/Asphaltenes) were obtained for the crude oil A using an ASTM technique (Mohammed et al., 2003). In order to deposit SARA fractions onto the surface of the substrates, we first dissolved these fractions in toluene at 70^{o}C. The solutions were prepared separately for resins, aromatics and asphaltenes. Mica and silicon substrates were aged in these individual SARA solutions in the same way as aging in the crude oil. Cyclohexane was not used as a solvent for these SARA fractions because asphaltenes do not dissolve completely in cyclohexane even at elevated temperatures.

Contact Angles: A contact angle goniometer was used to measure the advancing and receding water/oil contact angles by the sessile drop method. An optical glass cell, filled with the aqueous phase, was placed between a light source and a microscope. A horizontal mica/silicon plate was placed inside the aqueous phase. A U-shaped stainless steel needle attached to a motor driven

syringe was used to introduce an oil droplet at the bottom surface of the plate. Decane was used as the probe oil. The volume of oil droplet was increased until the contact line moved outwards. A video frame grabber captured the image of the drop and contact angles were measured by fitting the drop shape to a solution of the Young-Laplace equation (Hirasaki, 1991). The contact angle measured was the receding angle. The volume of the oil droplet was later decreased using the motor driven syringe until a neck forms. The angle formed by the droplet just before the detachment from the tip of the syringe is known as the advancing angle. On further reducing the volume of the oil droplet, the neck got thinner and finally broke. The contact angle at that moment, known as secondary relaxed advancing angle by Freer et al. (2003), was measured. The secondary relaxed advancing contact angle was found to be very close to the advancing angle. The oil volume was increased or decreased slowly in order to reduce the effect of viscous forces.

AFM images: The topography of the sample surfaces was imaged using an AFM (Nanoscope III A, manufactured by Veeco, Santa Barbara, CA). The AFM was mounted on a vibration isolation table. All the topography images were obtained using the tapping mode in air or in water. This mode is better suited over the contact mode for studying soft samples because it exerts very little lateral force as compared to the contact mode. The probes used were aluminum coated silicon probes for tapping in air and Olympus oxide-sharp silicon nitride probes for tapping in fluid. Both kinds of probes were obtained from Veeco. The drive frequency for imaging in water was around 8 kHz whereas that for imaging in air was around 300 kHz. A fluid cell, also from Veeco, was used for imaging in water.

The AFM images are typically quantified by three numbers at the microscopic scale: mean roughness, RMS value and Z scale. The mean roughness, R_a of an AFM image is defined as,

$$R_a = \frac{\sum_{i=1}^{N} \left| h_i - \bar{h} \right|}{N} \quad (1)$$

where h_i denotes the elevation of a data point i, $\bar{h}$ is the mean elevation and N is the number of data points in the image. The image RMS, R_q is the root mean square average of the height deviations taken from the mean data plane and is expressed as

$$R_q = \sqrt{\frac{\sum_{i=1}^{N} \left| h_i - \bar{h} \right|^2}{N}} \quad (2)$$

The Z scale gives the vertical distance between the highest and the lowest point in the image. The topography images can give an idea of the adsorbed film thickness if there is an area with no adsorption. To get a film thickness, we scratched away some of the organic coating from the silicon surface and then imaged the scratched sample at the boundary of adsorbed layer adjacent to the bare silicon surface. The silicon surface is very hard and does not get damaged when the adsorbed oil layer is scraped. This technique cannot be applied on the mica surface because it is soft and gets scratched very easily.

Force Measurements: In AFM force measurements, a tip is brought close to a surface and the deflection of the cantilever is measured as a function of tip-sample distance as shown in Fig. 1. At large tip-sample separations (1), there are no detectable interaction forces. As the separation distance decreases (2), forces such as electrostatic, van der waals, specific interactions etc. come into play. As the tip is brought closer to the sample, at some point (3) the gradient of the attractive force exceeds the spring constant of the cantilever and the cantilever tip jumps into contact with the sample (4). This vertical distance between (3) and (4) gives us a measure of the jump to contact force. From position (4) to (5), the tip and the sample remain in contact with

each other until the tip starts to retract. As the tip retracts, at a particular point (6) the spring constant exceeds the gradient of the force of adhesion between the tip and the sample and the tip suddenly breaks away from the sample to its equilibrium position (7). The value of the spring force at 6 is called the force of adhesion or pull-off force or jump-off contact force. This force of adhesion can be related to the surface energy using the JKR theory of adhesion mechanics as (Schneider et al., 2003)

$$F_{adh}=(3/2)\pi R W_{abc} \quad , \qquad (3)$$

where W_{abc} is the work of adhesion to pull the tip off the sample, R is the radius of curvature of the tip, a represents the cantilever tip, b represents the medium and c is the surface. W_{abc} can be expressed as a function of surface energies as $W_{abc}= W_{ab} +W_{bc} -W_{ac}$, where W_{ab} is the tip surface free energy in equilibrium with the medium, W_{bc} is the sample surface free energy in equilibrium with the medium and W_{ac} is the interfacial free energy of the tip-sample contact interface.

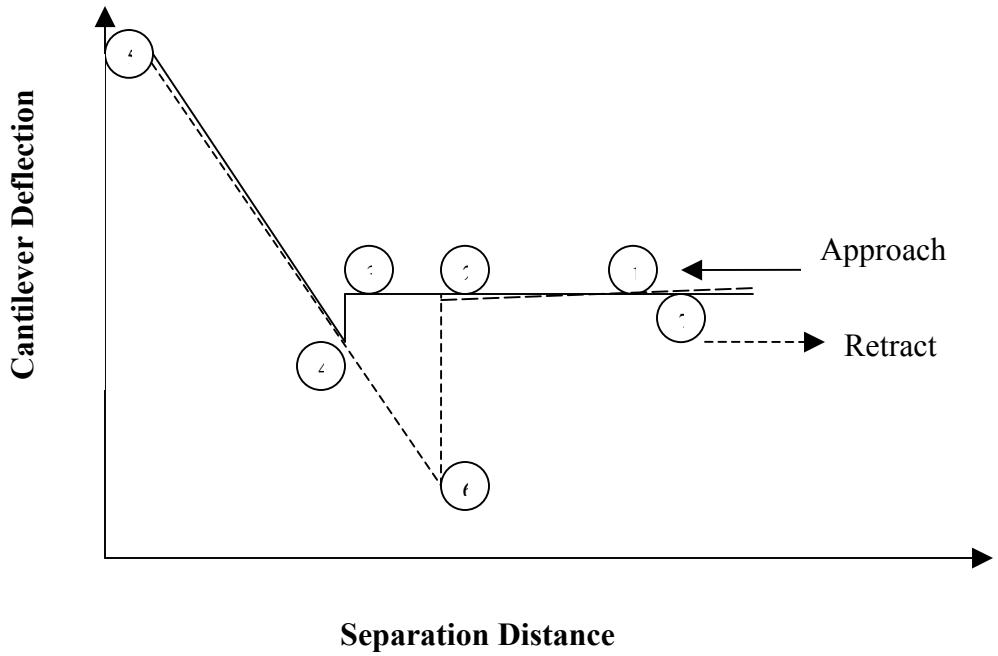

Fig. 1 - A typical cantilever displacement vs. separation distance plot as obtained by AFM.

The interaction forces in water between chemically modified spherical tips and the oil treated surfaces in water were measured using the AFM. Cantilevers with 1μm diameter, COOH-terminated borosilicate spherical tips (from Novascan Technologies Inc.) were used. These cantilevers had a nominal spring constant of 0.32 N/m. When the spherical tip is brought close to the sample, there are issues of water drainage from the thin water film and when the tip retracts, we have water suction into the film. The dynamics of the film is quite complicated to model. As an alternative, we use the adhesion force or pull-off force to characterize the surface. Force Measurements were done in the contact mode. While measuring the interaction forces, the whole tip was kept inside water in the fluid cell. Moreover, the tip was wetted with water before it was placed on AFM in order to avoid trapping of any air bubble at the tip or capillary effects. The force of adhesion also depends on Z scan rate, which was taken to be 0.199 Hz in our experiments. The scan rate is kept low in order to minimize the effects of viscosity. Force measurements were also attempted when both the tip and the sample surface were dry but the force of adhesion between the tip and the mineral surface was very large. Capella & Dietler (1999) have also observed that the attractive and the adhesion forces become almost 10 times smaller in water as compared to that in air. Another disadvantage of force measurements in air is that meniscus forces need to be included in the interpretation.

WAG Floods: The experimental apparatus is shown in Fig. 2. The Berea core had a residual water saturation of 28.6%. It was flooded with live oil at a constant flow rate of 0.15 mL/min until reaching steady state. The gaseous solvent or water-alternating gas slugs were then injected into the core at the same rate. Pressure drop and effluent composition were monitored.

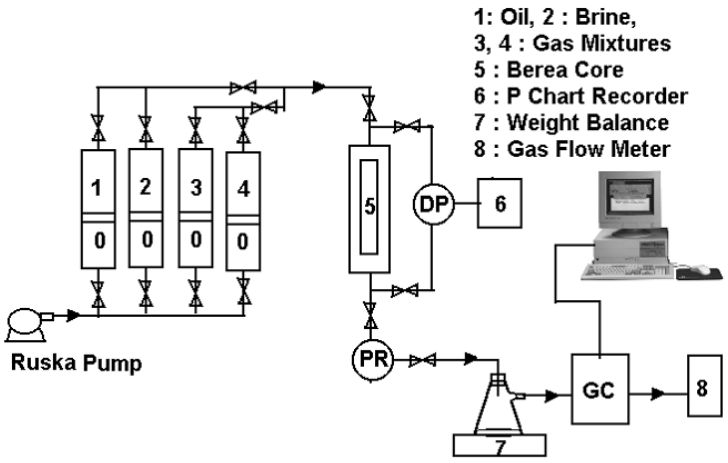

Fig. 2 – Experimental apparatus used in WAG floods

A quarter 5-spot high-pressure cell has been built to mimic the areal sweep of an oil reservoir. WAG floods have been conducted in this 5-spot cell using the same flow loop as shown in Fig. 2 where the core is replaced by the 5-spot cell. The 5-spot high-pressure cell consists of three stainless steel circular plates. The top and bottom plates are identical. Each has a cut-in section for the overburden liquid. The middle plate has a cut-off section of 10" x 10" x 1" at the center for the packing porous media. Two circular sheets of Buna N rubber are used to sandwich the packing media and prevent channeling effect when liquid is flowing through the media. The other side of the rubber faces the overburden liquid when the three plates are put together. The center plate also has two o-ring slots on each face to prevent leaking overburden liquid to the packing section and to the outside gaps when the three plates are bolted together.

There are 12 outlet ports for various well configurations and to distribute the oil effectively at the beginning of each experimental run. There are 5 ports each on two opposite sides (A1-A5 and B1-B5) and two ports at the other two corners. For vertical well configuration, the solvent is injected at port A1 and the production is collected at port B1 while other ports are shut. For horizontal production well, the solvent is injected at port A1 and the production is

collected at ports B1 - B5. The difference between ports A1 to A5 and B1 to B5 is the elevation. By injection from port B1 and collection from port A2 to A5, we can examine the gravitational effects on oil recovery when the bottom holes are lower or higher than the injecting hole for horizontal well. To distribute the oil effectively at the beginning of each run, the cell is placed at different orientations. Fig. 3 shows the side view of the porous section when oil is injected. First, oil is injected from port A1 until breakthrough at port C while other ports are shut. Extra amount of oil is pumped in to make sure that oil is swept out the water from previous run. Then the flow path is varied by closing port C and opening port D. After water stops coming out from port D, ports B1 to B5 are opened respectively while port D is closed. The injection port is then shifted to port C to complete sweeping out most of the water in the porous section. The cell after mostly filled with oil is set back to normal operating condition. Figures 4-6 show the front view, side view and top view digital images of the 5-spot high-pressure cell.

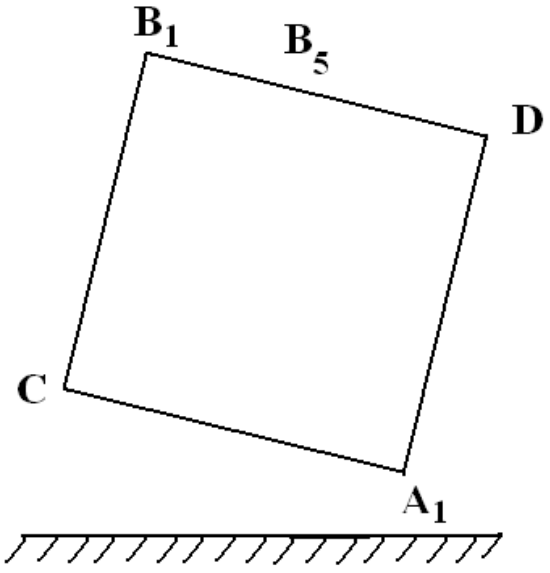

Fig. 3 - Oil injection sequence to saturate the medium with oil uniformly

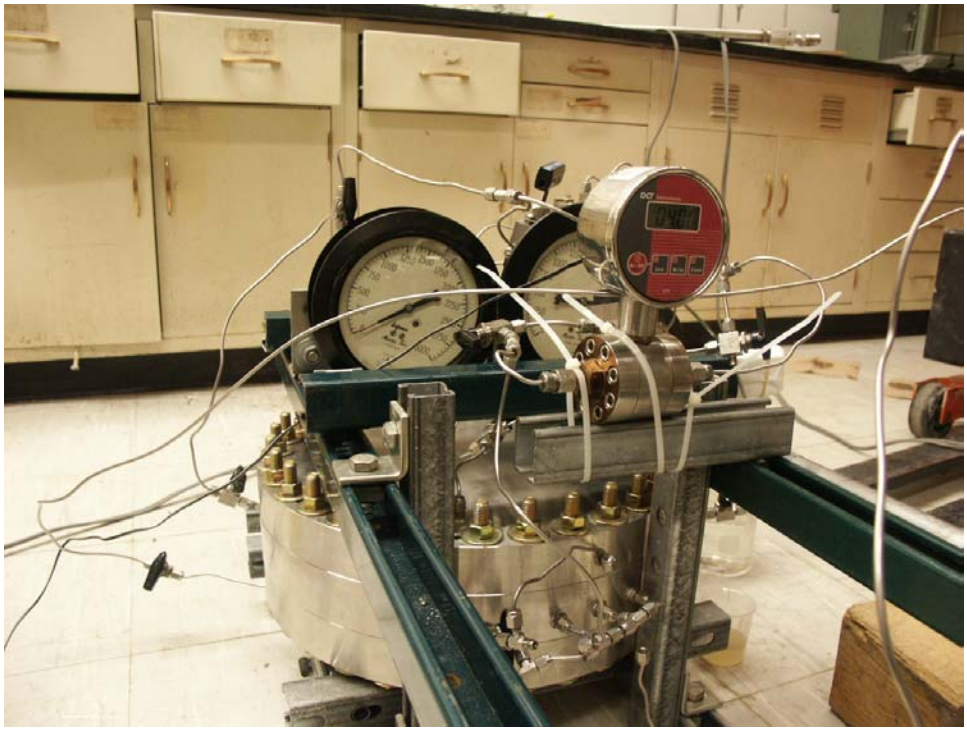

Fig. 4 - Front view of the 5-spot high-pressure cell

The middle plate is wet-packed with sand of mesh size ranging from 50 to 200. The measuring devices and regulators are hooked up and tests were performed to check for leakage. The safe operating pressure for the porous section is about 2000 psi while the overburden pressure is maintained at 2500 to 2600 psi. The cell is then hooked up to the flow loop and WAG floods are being conducted.

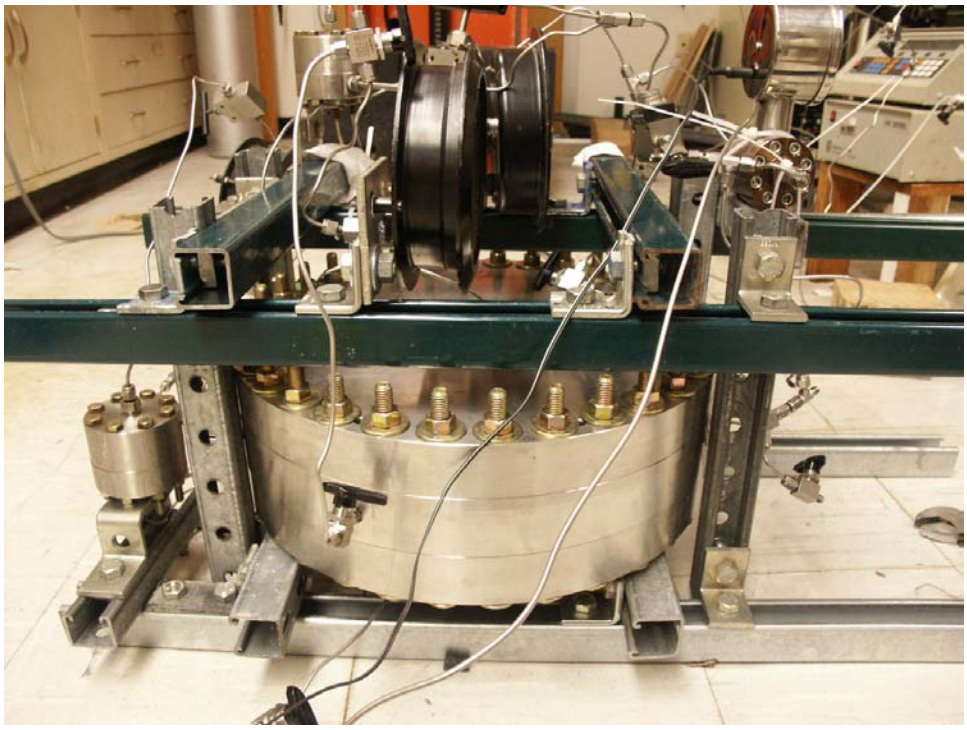

Fig. 5 - Side view of the 5-spot high-pressure cell

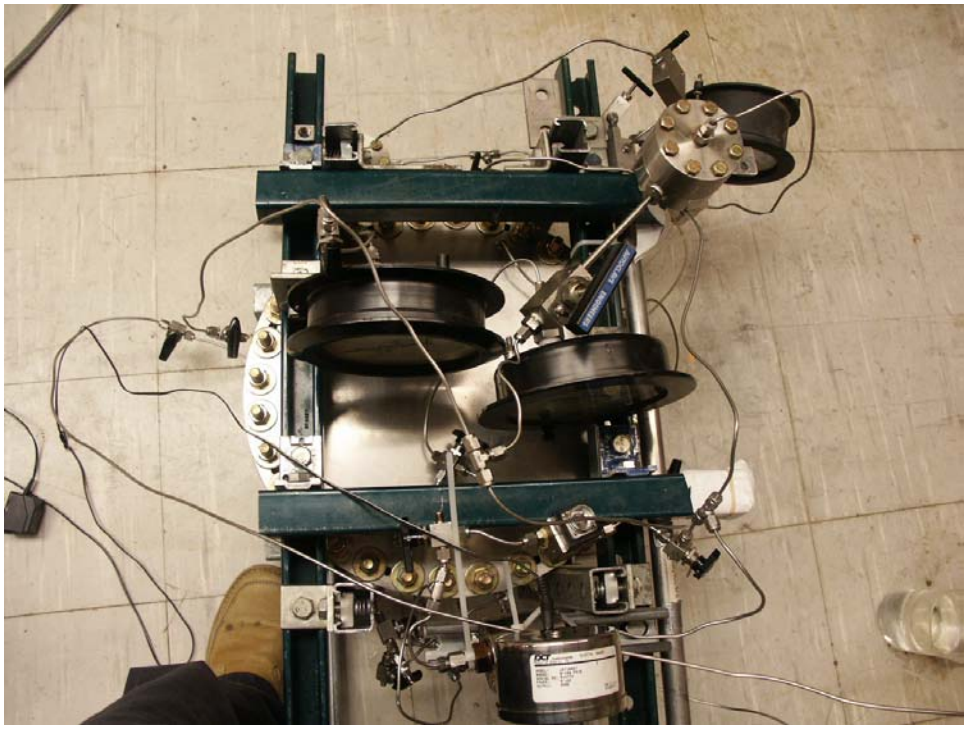

Fig. 6 - Top view of the 5-spot high-pressure cell

Modeling Methods

Compositional Model

Several North Slope gas streams may be available for injection into shallow sands reservoirs in the North Slope, e.g., Prudhoe NGL, Kuparak NGL, and Prudhoe lean gas. Prudhoe gas streams contain a significant amount of CO_2. CO_2 cannot be put into potential gas pipelines and is a greenhouse gas. However, mixtures of CO_2 and NGL can make effective miscible injectants for shallow viscous reservoirs. The complicating issue in the displacement calculations of these gases is the presence of L1-L2-V phases. Three fluid phases, i.e. a vapor and two liquid phases, have long been observed in hydrocarbon and CO_2 mixtures (Meldrum & Nielsen 1955; Mohanty et al. 1995). Three hydrocarbon phases occurs at relatively low temperatures and pressures. The shallow sands temperature is about 60-100 °F and pressure about 1200-1800 psi. Thus a compositional simulator is needed that can handle three hydrocarbon phases and water for WAG flood simulations. We have installed a version of UTCOMP, a three-dimensional, equation-of-state compositional simulator (Courtesy: Prof. Gary Pope, University of Texas) which can incorporate three hydrocarbon phases (Chang et al., 1990). A series of slimtube displacements of Shrader Bluff oil by different injectants were simulated and the recoveries were compared with the slimtube experiments of Kahatniar et al. (1999).

Relative Permeability Formulation

Modeling flow of four fluid phases (water, oil, gas, and the second non-aqueous liquid) is important to the water-alternating-gas (WAG) floods. However, four-phase systems cover a large number of saturation paths. The relation between phase saturation and pressure is also delicate. It is prohibitively expensive if not impossible to experimentally measure relative permeabilities for a four-phase system.

Experimental data are not collected regularly for three-phase systems for a similar reason. Pore-scale mechanistic models[4-7] (Fenwick & Blunt, 1998; Van Dijke et al., 2002) have been developed for three-phase flow, but lack of pore-scale structure and wettability data makes them impractical. Instead, empirical models are often used which estimate three-phase relative permeabilities from experimental two-phase relative permeabilities: water-oil and oil-gas. Two empirical models proposed by Stone (Stone, 1970; Stone, 1973) are widely used in the oil industry even though comparisons with experiments (Fayers & Matthew, 1984; Delshad & Pope, 1989) have shown many inconsistencies. Baker (1988) has proposed a simple three-phase model based on saturation-weighted interpolation of two-phase relative permeabilities. These models are primarily for water-wet media and do not take trapping of non-wetting phases into account. Jerauld (1997)has developed a three-phase relative permeability model for Prudhoe Bay reservoir, which accounts for mixed-wettability, trapping, capillary number effects, and compositional consistency. Blunt (2000) has used the saturation-weighting technique and proposed a new model that accounts for trapping and oil layer flow at low saturations.

Guler *et al.* (2001) are the first to suggest a four-phase relative permeabilities based on the Baker model (1988) for three-phase flow. This model lumps oil and second phase saturations into one pseudo phase, which reduces the four-phase system to a three-phase system. It applies the Baker model to get the lumped relative permeability of the pseudo phase and then distributes it to the oil and the second liquid phase in proportion to their flowing saturations. This model presumes the medium to be water-wet and it does not account for gas phase hysteresis.

In this project, we have developed a new model, which is more appropriate for the saturation paths encountered during WAG floods in mixed-wet reservoirs. Gas phase hysteresis and compositional consistency are addressed. In our case studies (described in the results section), it was observed that many cells had three phases: water (phase 1), oil (phase 2) and

second liquid phase (phase 4, according to UTCOMP convention) (Chang, 1990). Some cells had all four phases. Very few cells had water, oil and gas (phase 3). Therefore, in this work, the gas phase (phase 3) and the second liquid phase (phase 4) are treated as one combined pseudo-phase (g).

Streamline-based Models

The computational time required for simulation of four phases during WAG floods of 3-D reservoirs is prohibitively expensive in traditional finite difference simulators. If large grid blocks are used, then numerical dispersion is large and the results are not accurate. In contrast, streamline method is much faster. Compared with conventional finite difference simulation, streamline simulation is much younger in terms of commercial usage. While finite difference simulation was commercialized in 1960's, the streamline simulation was used in commercial simulators in the 1990's (Osako *et al.*, 2003).

Based on the scheme developed by Batycky (1997), we have incorporated analytical and numerical streamline methods for flux updating into UTCOMP. The analytical methods can be used for water flooding and gas flooding with appropriate approximations. Numerical method is required for the WAG flooding. We have incorporated the numerical method for water, gas as well as WAG flooding. Fig. 7 illustrates the computational steps for water flooding; the steps for WAG floding are similar.

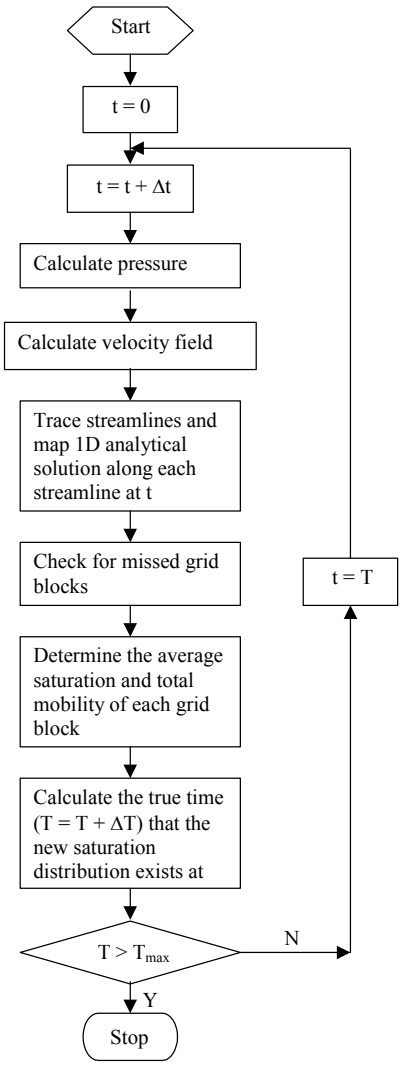

.

In Fig. 7, at the (n+1)st time step, true ΔT, is calculated by (Batycky, 1997)

$$\Delta T^{n+1} = \frac{W_{ini} - W_r^{n+1} + W_I^n - W_P^n}{Q^{n+1}(\bar{f}^{n+1} - 1)}, \tag{4}$$

where W_I^n is the total cumulative water injection at the nth time step, W_p^n is the total cumulative water production at the nth time step, W_{ini} is the initial amount of water, and W_r^{n+1} is total amount of water still remaining in the reservoir at the (n+1)st time step, Q^{n+1} is the water injection rate at

the (n+1)th time step, $\bar{f}^{n+1}$ is the average fractional flow at the nth and (n+1)th time steps. The average saturation for a grid block is calculated as (Batycky, 1997)

$$\bar{S}_{gb} = \frac{\sum_{i=1}^{n_{gb}^{sl}} \Delta\tau_i \bar{S}(\bar{\tau})_i}{\sum_{i=1}^{n_{gb}^{sl}} \Delta\tau_i}, \tag{5}$$

where n_{gb}^{sl} is the number of streamlines passing through a grid block, i is streamline index, $\bar{\tau}$ is the average time of flight for the streamline i that passes the grid block, $\bar{S}$ is the average saturation, $\Delta\tau$ is the difference between the time of flight for inlet and that for outlet. Streamlines are traced by using the method put forward by Pollock (1988).

Instead of mapping water saturation from 1D solutions, we map overall compositions of hydrocarbon components for gas or WAG injection. At T (the nth time step), the total cumulative injection of component i is

$$N_{i,I}^n = N_{i,p}^n + N_{i,r}^n - N_{i,ini}, \tag{6}$$

where $N_{i,I}^n$ is the total cumulative injection of component i at the nth time step, $N_{i,p}^n$ the total cumulative production of component i at the nth time step, $N_{i,ini}$ is the initial amount of component i, and $N_{i,r}^n$ is total amount of component i still remaining in the reservoir at the nth time step. Similarly for the (n+1)st time step, we have

$$N_{i,I}^{n+1} = N_{i,p}^{n+1} + N_{i,r}^{n+1} - N_{i,ini}. \tag{7}$$

The total cumulative injection of component i at the (n+1)st time step, $N_{i,I}^{n+1}$, can be written as

$$N_{i,I}^{n+1} = N_{i,I}^n + Q_I^{n+1} z_{i,I} \Delta T^{n+1}, \tag{8}$$

where Q_I^{n+1} is the solvent injection rate at the (n+1)st time step, $z_{i,I}$ is overall composition of component i in the solvent, and ΔT^{n+1} is the true time step at the (n+1) time step. The total cumulative production of component i at the (n+1)st time step, $N_{i,p}^{n+1}$, can be found as

$$N_{i,p}^{n+1} = N_{i,p}^{n} + Q_p^{n+1} \sum_{j=2}^{4} x_{i,j,p} \left(\frac{f_{j,p}^{n} + f_{j,p}^{n+1}}{2} \right) \Delta T^{n+1}, \tag{9}$$

where $f_{j,p}^{n}$ is the production fractional flow of phase j at the nth time step, $f_{j,p}^{n+1}$ is the production fractional flow of phase j at the (n+1)st time step, Q_p^{n+1} is production rate at the (n+1)th time step, and $x_{i,j,p}$ is composition of component i in phase j in the production fluid. So, from Eqs. 7 - 9, we get

$$\Delta T^{n+1} = \frac{N_{i,init} - N_{i,r}^{n+1} + N_{i,I}^{n} - N_{i,P}^{n}}{Q_I^{n+1} z_{i,I} - Q_p^{n+1} \sum_{j=2}^{4} x_{i,j,p} \left(\frac{f_{j,p}^{n} + f_{j,p}^{n+1}}{2} \right)}. \tag{10}$$

The true time step is incremented by the above ΔT^{n+1} in the (n+1)st time step.

Well Architecture Evaluation

Effect of horizontal production wells on sweep efficiency is studied by numerically modeling quarter 5-spot displacements. A three-dimensional streamline simulator is used to evaluate sweep efficiency. Pressure drop in the horizontal well due to frictional losses is an important issue. If the pressure drop in the well is comparable to drawdown at the heel, then it plays a significant role in determining the productivity from the well. Productivity generally increases as the horizontal well length increases. The increased length may, however, decrease sweep efficiency. The length of the horizontal well can be optimized on the basis of these two factors.

A 3-D black oil streamline simulator consisting of 2 phases (oil and water) is used for waterflooding. Corey model is assumed for relative permeability functions. No skin effects are considered around the wellbore region. Peaceman (1991) model is used for calculating the equivalent well radius and well factors. Pressure drop in the horizontal well is calculated assuming frictional pressure drop only. Pressure drop due to acceleration is very small and hence neglected Economides et al. (1990).

For a single-phase fluid flow, pressure drop in a pipe is given by (Penmatcha et al., 1997)

$$\Delta P = \frac{f_m \, 8 \, Q^2 \, \Delta X \, \rho}{\pi^2 D^5} \tag{11}$$

where fm is the friction factor, Q is the volumetric flow rate, D is the well diameter, and ρ is the fluid density. The friction factor is given by,

$f_m = 64/\mathrm{Re}$ for Re <2300 (laminar), (12)

$$f_m = \frac{.3164}{\mathrm{Re}^{.25}} \text{ for } 2300 <= \mathrm{Re} < \mathrm{Re1}, \tag{13}$$

$$f_m = .0032 + \frac{.221}{\mathrm{Re}^{.237}} \text{ for } \mathrm{Re1} <= \mathrm{Re} < \mathrm{Re2}, \tag{14}$$

and

$$\frac{1}{\sqrt{f_m}} = 2\log\left(\frac{2.51}{\mathrm{Re}\sqrt{f_m}} + \frac{1}{3.71}\frac{\varepsilon}{D}\right) \text{ for Re> Re2.} \tag{15}$$

The Reynolds number, Re, is defined as,

$$\mathrm{Re} = \frac{\rho v D}{\mu} \tag{16}$$

and

$$\mathrm{Re1} = 59.5\left(\frac{D}{\varepsilon}\right)^{1.143} \tag{17}$$

$$\mathrm{Re}\,2 = \frac{D}{2\varepsilon}\left(665.4 + 764.8\log\frac{D}{2\varepsilon}\right). \qquad (18)$$

After the water breakthrough in the production well, two phases (oil and water) flow through the well. We compute pressure drop assuming a pseudo-single phase flow of average density and viscosity. Same equations are used as in the single-phase flow, but the average density (ρ_m) and viscosity (μ_m) are used, i.e.,

$$\rho_m = \rho_w f_w + (1 - f_w)\rho_o \text{, and} \qquad (19)$$

$$\mu_m = \mu_w^{f_w} \mu_o^{1-f_w}. \qquad (20)$$

Electromagnetic Heating Evaluation

A simple steady state model has been derived to study the effect of electromagnetic heating on the well deliverability in a viscous oil reservoir. Electromagnetic waves can be absorbed by water leading to heating of the adjacent oil, which reduces oil viscosity and increases oil flow rate (Sahni et al., 2000). Some assumptions have been made to derive a simple set of equations that can be solved rapidly. These assumptions are as follows:

- Oil, water, and sand are at local thermal equilibrium,
- Oil flow and heat transfer are primarily radial, and
- Except viscosity all the other fluid properties are constant, such as, density, specific heat etc.

The thermal balance gives,

$$-r^{-1}\, d(rq_r)/dr + \rho C_p\, r^{-1}\, d(Tvr)/dr + P_0 \exp[-\alpha(r-r_w)] - h(T-T_i)/H = 0 \qquad (21)$$

where the heat conduction q_r is given by

$$q_r = -k\, dT/dr, \quad (22)$$

the oil radial velocity is given by the Darcy's law, i.e.,

$$v = -(K/\mu)\, dp/dr, \quad (23)$$

the viscosity μ is given by

$$\mu = A \exp (B/T), \quad (24)$$

where ρ is the oil density, Cp is the heat capacity of oil, α is the electromagnetic power attenuation coefficient of the rock, A and B are empirical coefficients modeling temperature dependence of viscosity, k is the thermal conductivity of the fluid saturated rock, K is the permeability to oil, h is the heat transfer coefficient between the reservoir rock and the over- and under-burden, and H is the thickness of the oil zone. The velocity field also satisfies the continuity equation,

$$r^{-1}\, d(rv)/dr = 0 \quad (25)$$

These equations are solved to calculate deliverability improvement by electromagnetic heating.

Results and Discussion

Compositional Modeling

A series of slimtube displacements of Shrader Bluff oil by different injectants were simulated and the recoveries were compared with the slimtube experiments of Khataniar et al. (1999). Khataniar et al. had simulated these displacements with a simulator that can incorporate only two hydrocarbon phases. The solvents used are listed in Table 3 and consist of mixtures of CO2 - NGL and Prudhoe Bay gas (PBG) – NGL. The NGL, PBG and crude oil composition were taken from the experimental values (Guler et al., 2001). The C7+ composition was modeled by five pseudocomponents. NGL is predominantly butane-pentane. PBG is predominantly methane-CO2. All simulations were conducted at a temperature of 82 °F. Enrichments were varied in two different kinds of injection mixtures: CO_2-NGL and PBG-NGL. Simulations were run for two different initial reservoir pressures: 1300 and 1700 psi in order to investigate the pressure effect on different injection mixtures. 40 grid blocks were used to represent the 40 ft long slimtube. Conditions for the slimtube simulations are listed in Table 4.

Table 3 - Schrader Fluid Compositions

Component	Live Oil	PBG	NGL
CO2	0.000436	0.12179	0
C1	0.272149	0.76587	0
C2	0.004128	0.06242	0
C3	0.010484	0.03133	0.0439
C4	0.021230	0.01108	0.4337
C5	0.020020	0.00329	0.2543
C6	0.022566	0.00422	0.1198
C7-9	0.098746	0	0.1483
C10-13	0.100533	0	0
C14-19	0.145138	0	0
C20-35	0.164159	0	0
C36P	0.140411	0	0

Table 4 - Conditions for the Slim Tube Experiments[2]		
Parameters	Value	Unit
P_i	1300	psi
T	82	^oF
K	5000	md
ϕ	0.352	unitless
D	0.252	in
L	40	ft

Displacement of oil by CO2 was found to be immiscible at 1300 psi and 82 °F. Fig. 8 shows the in situ saturation profile at 0.6 PV injection. It shows an oil-solvent displacement front; 30-40% of the oil is left behind this front. A tiny three-phase region is detected ahead of the oil-solvent displacement front. The recovery at 1.2 PV injection is 79% compared to 71.6% in the experiments. Some of this difference can be ascribed to the relative permeability used. We did not have the experimental relative permeability for the sand pack used in the slim tube.

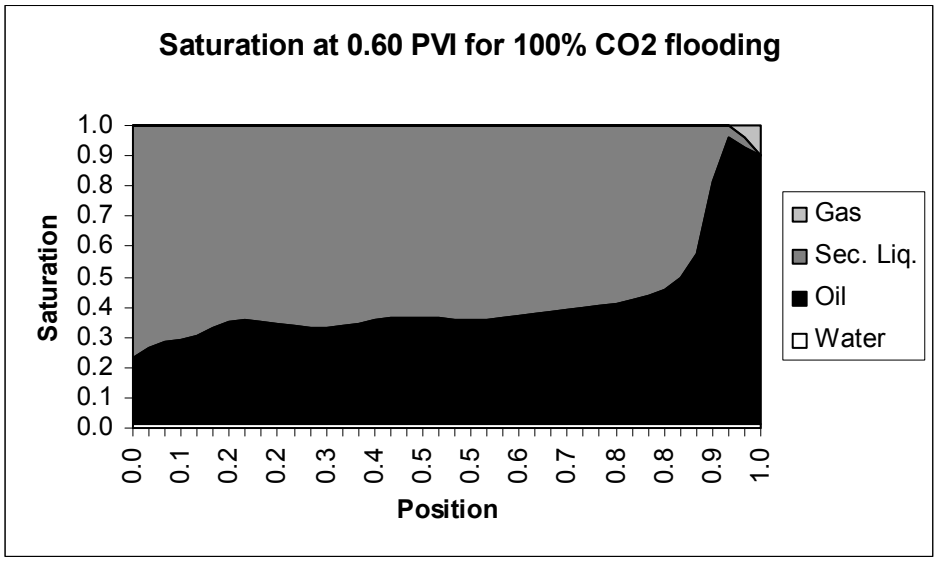

Fig. 8 - In situ saturation profile along the length of the slimtube at 0.6 PV injection of CO2.

Displacement of oil by 90%CO2-10%NGL was found to be immiscible at 1300 psi and 82 °F. Fig. 9 shows the in situ saturation profile at 0.6 PV injection. It shows an immiscible oil-solvent displacement front; 20-30% of the oil is left behind this front. A small (Sg~10%) methane bank forms ahead of the oil-solvent displacement front. The recovery at 1.2 PV injection is 88.3% compared to 88.5% in the experiments. The oil-phase left behind the displacement fronts appear to be larger than the oil not recovered, because the oil left behind is swollen with solvent components.

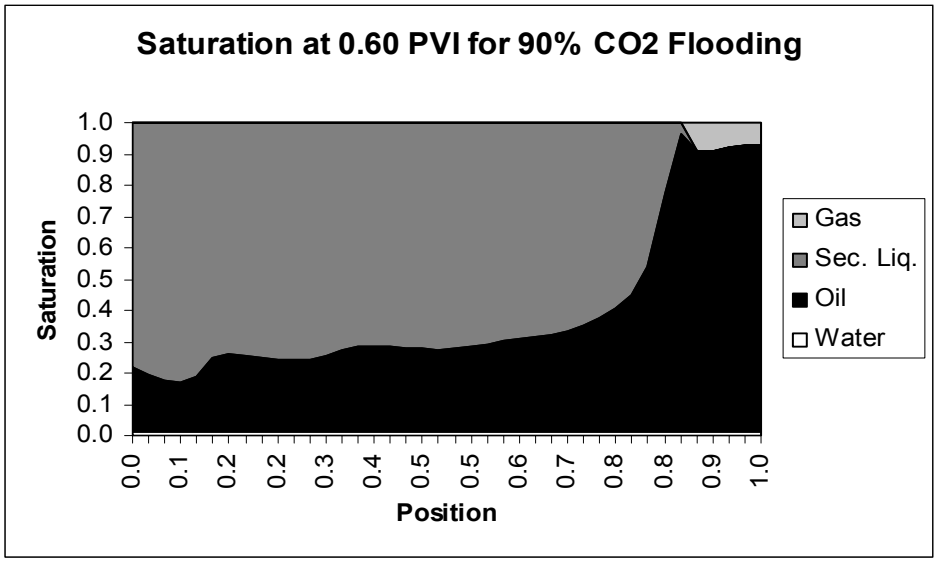

Fig. 9 - In situ saturation profile along the length of the slimtube at 0.6 PV injection of 90%CO2-10%NGL.

Displacement of oil by 85%CO2-15%NGL was found to be close to miscible at 1300 psi and 82 °F. Fig. 10 shows the in situ saturation profile at 0.6 PV injection. The recovery at 1.2 PV injection is 91.9% compared to 98% in the experiments. In the experiments, miscibility was developed at this enrichment of the solvent. Fig. 11 shows the in situ saturation profile at 0.6 PV

injection of 70% CO2-30%NGL. The recovery is 100% in the simulation; experimental data was not available for this case. Simulations show that MME is approximately 15-20% for NGL-CO2; which is consistent with 15% found experimentally.

Displacement of oil by PBG was found to be immiscible at 1300 psi and 82 °F. Fig. 12 shows the in situ saturation profile at 0.6 PV injection. The oil-solvent displacement front is gradual; the oil saturation decreases from 80% to 40% along the length of the slimtube, typical of immiscible displacement at high mobility ratio. There is no second hydrocarbon liquid phase. The recovery at 1.2 PV injection is 47.3% compared to 45% in the experiments.

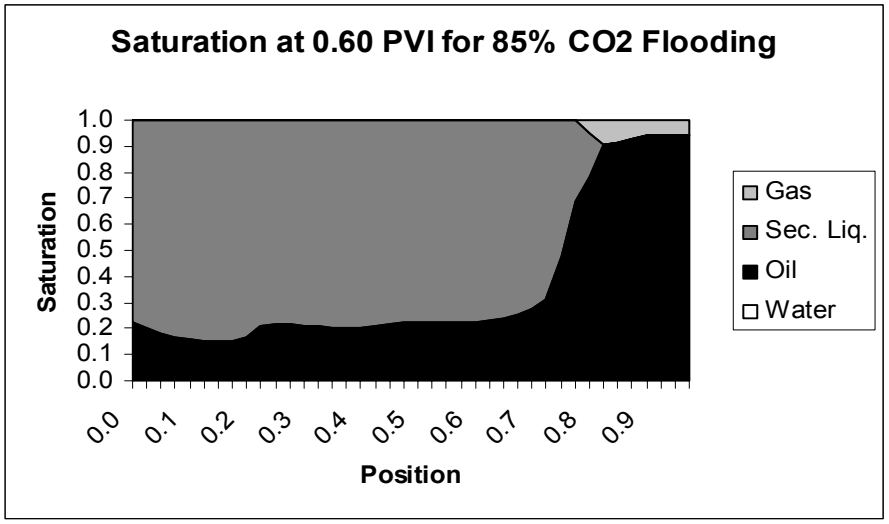

Fig. 10 - In situ saturation profile along the length of the slimtube at 0.6 PV injection of 85%CO2-15%NGL.

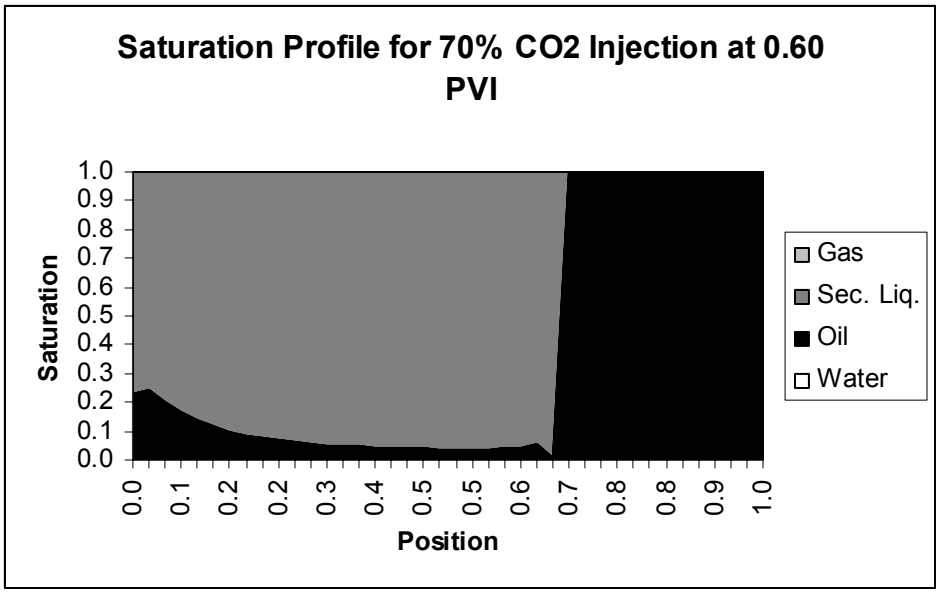

Fig. 11 - In situ saturation profile along the length of the slimtube at 0.6 PV injection of 70%CO2-30%NGL.

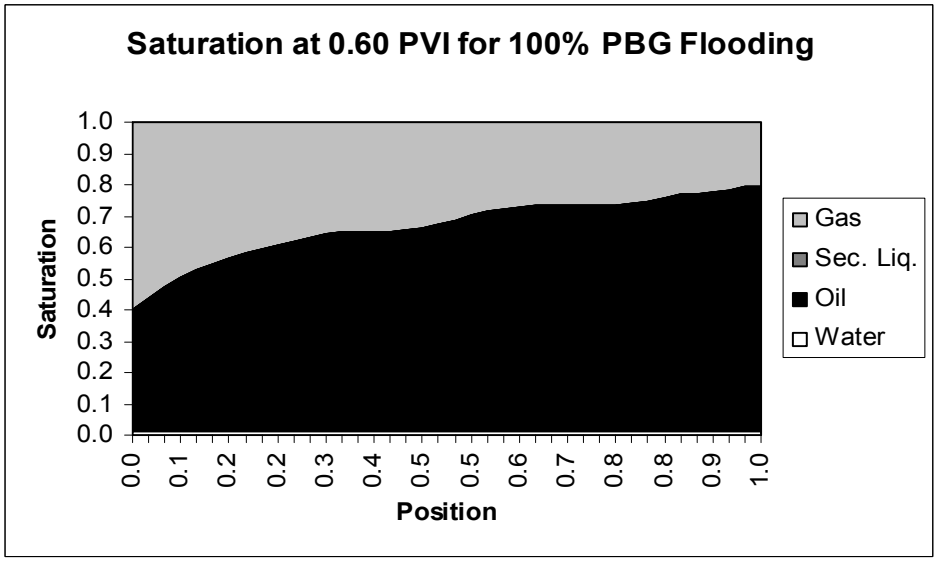

Fig. 12 - In situ saturation profile along the length of the slimtube at 0.6 PV injection of PBG.

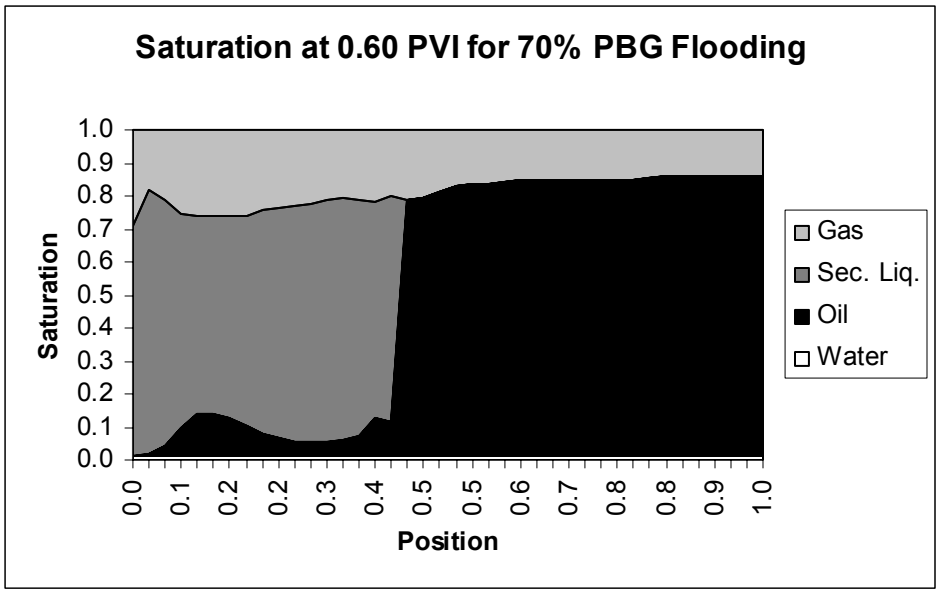

Fig. 13 - In situ saturation profile along the length of the slimtube at 0.6 PV injection of 70%PBG-30%NGL.

Displacement of oil by 70%PBG-30%NGL was found to be close to miscible at 1300 psi and 82 °F. Fig. 13 shows the in situ saturation profile at 0.6 PV injection. At this pressure and temperature, the injectant forms two phases by itself. The gas phase persists through out the length of the slimtube. Three phases exist behind the oil-solvent displacement front. The liquid from the injectant displaces the oil almost miscibly (this front is very sharp). The immiscible flow of the gas phase slows down the oil recovery somewhat. The recovery at 1.2 PV injection is 91.3% compared to 86.6% in the experiments. In the experiments, miscibility was developed at enrichment of the solvent. Fig. 14 shows the in situ saturation profile at 0.6 PV injection of 60% PBG-40%NGL. The recovery is 100% in the simulation vs. 92.6% in the experiment. The displacement is very similar to the last case. The injectant is again two-phase, but the gas saturation is lower.

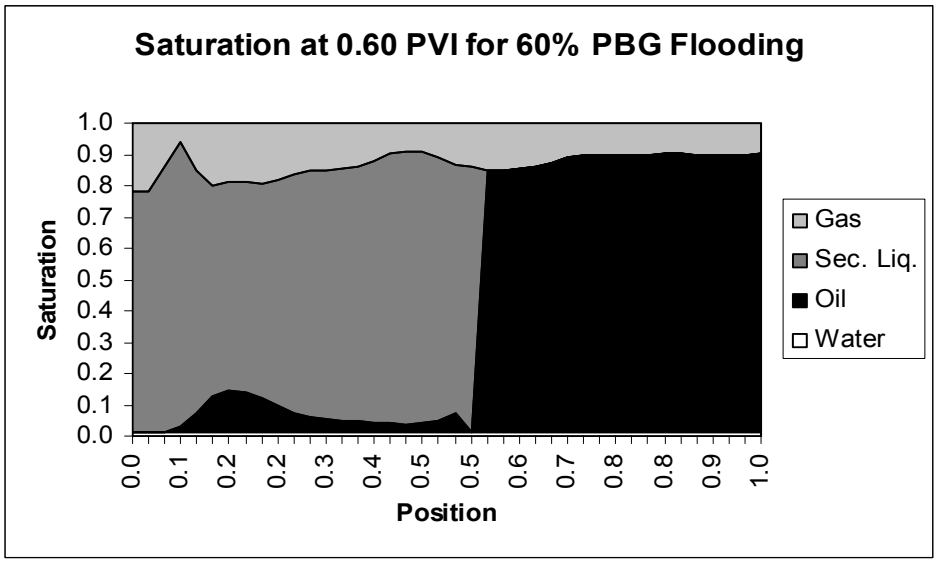

Fig. 14 - In situ saturation profile along the length of the slimtube at 0.6 PV injection of 60%PBG-40%NGL.

Displacement of oil by 50%PBG-50%NGL was found to be miscible. At this enrichment, the injectant is single-phase. Fig. 15 shows the in situ saturation profile at 0.6 PV injection of 50% PBG-50%NGL. The second liquid phase displaces the oil miscibly. Three hydrocarbon phases occur only near the displacement front. The recovery is 100% in the simulation vs. 99% in the experiment. Simulations show that MME is approximately 40% for PBG-NGL, which is consistent with 50% found experimentally.

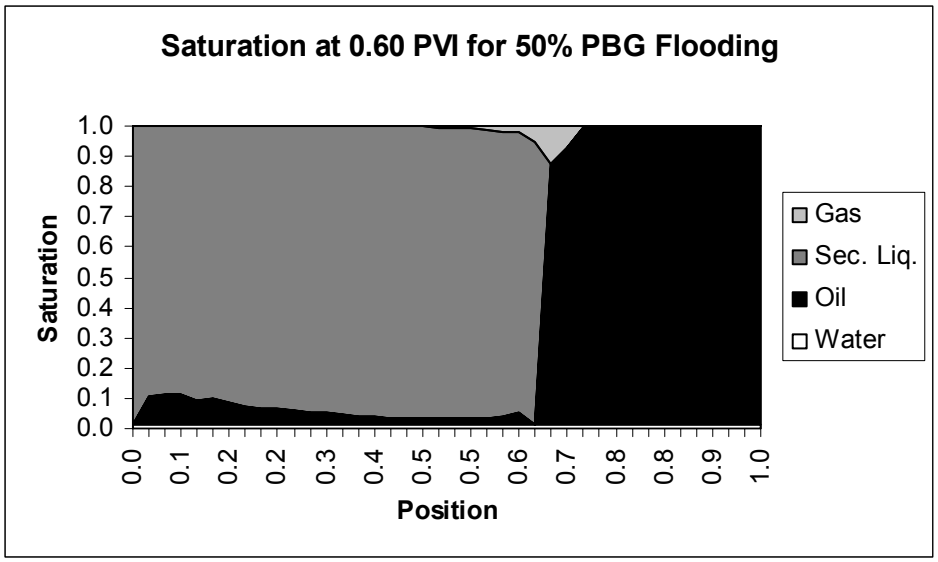

Fig. 15 - In situ saturation profile along the length of the slimtube at 0.6 PV injection of 50%PBG-50%NGL.

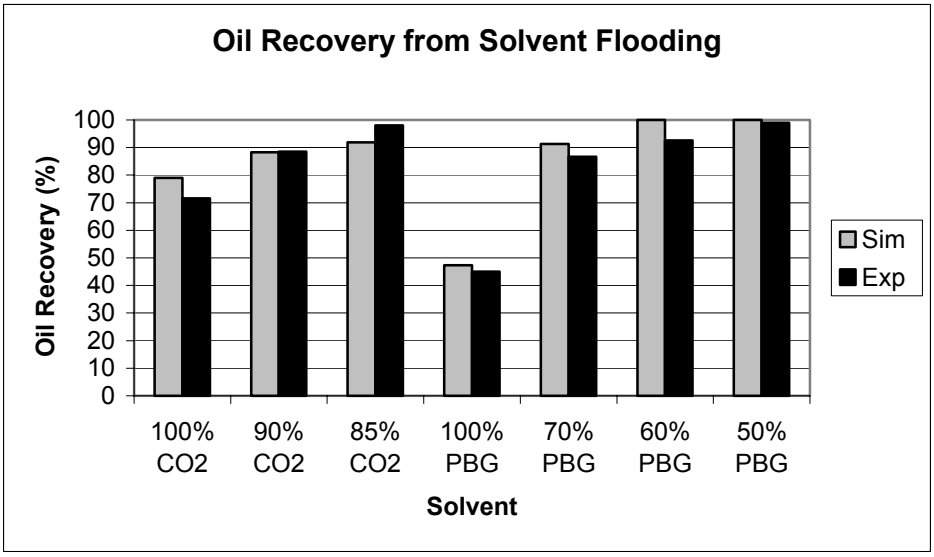

Fig. 16 - Comparison of simulated and experimental slimtube Shrader Bluff oil recovery at 1.2 PV injection for various CO2-NGL and PBG-NGL solvents at 82 F and 1300 psi.

Fig. 16 shows the comparison of the 1.2 PV injection recoveries between simulations and experiments. The simulation results compare quite well considering that arbitrary relative permeability functions are used. The slimtube simulator is also used to study the sensitivity of

gas injection to pressure, since the pressure in the reservoir varies between 1300 and 1700 psi. Fig. 35 compares slimtube oil recovery at 1.2 PVI at 1300 and 1700 psi at different levels of NGL enrichment. The oil recovery by CO2+NGL solvent is not very sensitive to pressure in this range. The oil recovery by Prudhoe Bay lean gas + NGL solvent is quite sensitive. The recovery increases and the minimum miscibility enrichment decreases by 10%. This simulator has also been used to identify simplified solvents and phase saturation paths relevant to WAG floods for laboratory studies. The goal of future research is to make these calculations more efficient to enable mechanistic simulation of WAG displacements in 3-D reservoirs.

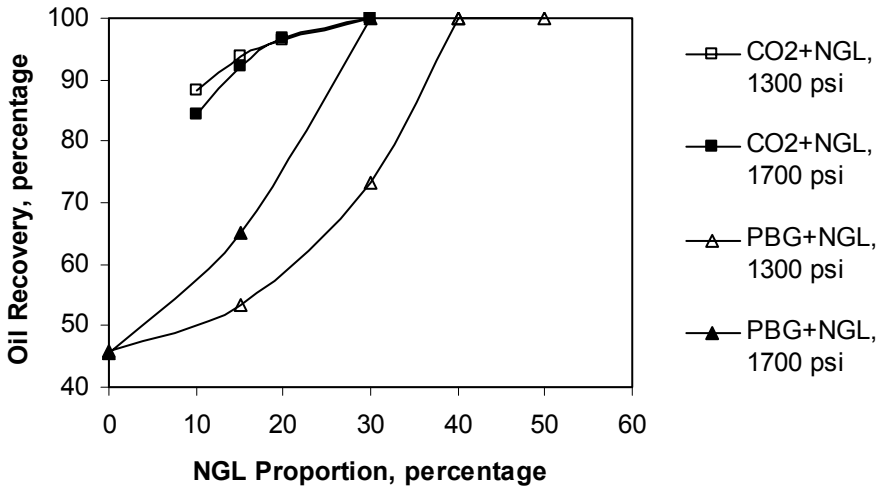

Fig. 17 - Pressure sensitivity of oil recovery by gas injection

Relative Permeability

Contact Angles in Dry Mode. Water/decane contact angles were measured for mica/silicon substrates treated with Crude A (Shraeder oil) and washed with different samples. Fig. 18 shows a typical drop of decane surrounded by water under a mica plate treated with Crude A. All the contact angles were measured through the water phase. Table 5 shows the contact angles measured for samples treated in the dry mode (i.e., the excess solvent was removed by drying in open air). The contact angles are the highest for the cyclohexane-washed surface implying that it is the most oil-wet.

Fig. 18 - A decane drop surrounded by water on a mica sample treated with Crude A

Contact Angles in Wet Mode. The advancing and receding contact angles for the three differently treated substrates in the wet mode for Crude A are also listed in Table 5. Both the advancing and receding contact angles are the lowest for toluene, in the middle for decalin and the highest for cyclohexane. These contact angles also signify that the cyclohexane-washed samples are more oil-wet than toluene and decalin-washed samples. Table 6 shows the contact angles for samples treated in wet mode for Crude B. A similar trend is also observed in contact angles in this case (i.e., the contact angle being the highest for cyclohexane). For Crude A, the contact angles were higher for the silicon substrate for toluene and decalin whereas for the case of Crude B, the opposite was observed.

Dry Mode						
	Toluene-treated		Decalin-treated		Cyclohexane-treated	
	Advancing	Receding	Advancing	Receding	Advancing	Receding
Mica	118	180	110	180	180	180
Wet Mode						
Mica	105	32	112	41	146	68
Silicon	114	52	115	56	125	67

Table 5 - Contact angles for minerals aged in Crude A and washed with different solvents

Wet Mode						
	Toluene-treated		Decalin-treated		Cyclohexane-treated	
	Advancing	Receding	Advancing	Receding	Advancing	Receding
Mica	116	37	123	47	145	60
Silicon	69	30	87	33	128	50

Table 6 - Contact angles for minerals aged in Crude B and washed with different solvents

AFM images of substrate. The most important requirement for a substrate to be analyzed by AFM is that it should be molecularly smooth. Both mica and silicon used for this study satisfy this criterion. The mica surface was found to have a surface roughness of 0.125 nm which is quite close to the value reported in the literature (Yang et al., 1999). The silicon surface was found to have a mean surface roughness, R_a of 0.176 nm.

Dry imaging in air. The oil-aged mica substrate was first washed with a solvent, the excess solvent was removed by letting the sample dry in open air for 24 hours, and then the substrate was scanned using the tapping mode in air. It was observed that toluene and decalin-removed the oil from the samples more efficiently than cyclohexane. Figs. 19-21 show the 50 x 50 μm scans for the mica surface treated with the three different solvents, respectively. Figs. 37a-39a show the height images or the amount of material adsorbed whereas Figs. 19b-21b show the phase images or the kind of material adsorbed. The white regions in the height images represent the peaks of adsorbed materials and the dark regions represent the bare mica surface or valleys. The statistics for these images are summarized in Table 7. The mean roughness and RMS was found to be the lowest for cyclohexane. The toluene-washed sample had the highest mean roughness whereas the decalin-washed sample had the highest RMS. A lot of bare mica could be seen in the images for the toluene and decalin-treated samples. This can be one of the reasons for the high mean roughness and RMS for the toluene-washed samples. For all the cases, it was seen that some crystal like structure form on the surface. These structures are more distinct in the phase images of Figs. 19b-21b. A possible explanation could be that when the solvents evaporate they leave behind some of the dissolved material which sort of crystallize or aggregate to form these structures. This evaporation is not typical of the oil reservoir conditions; therefore we conducted studies in the wet mode in this work.

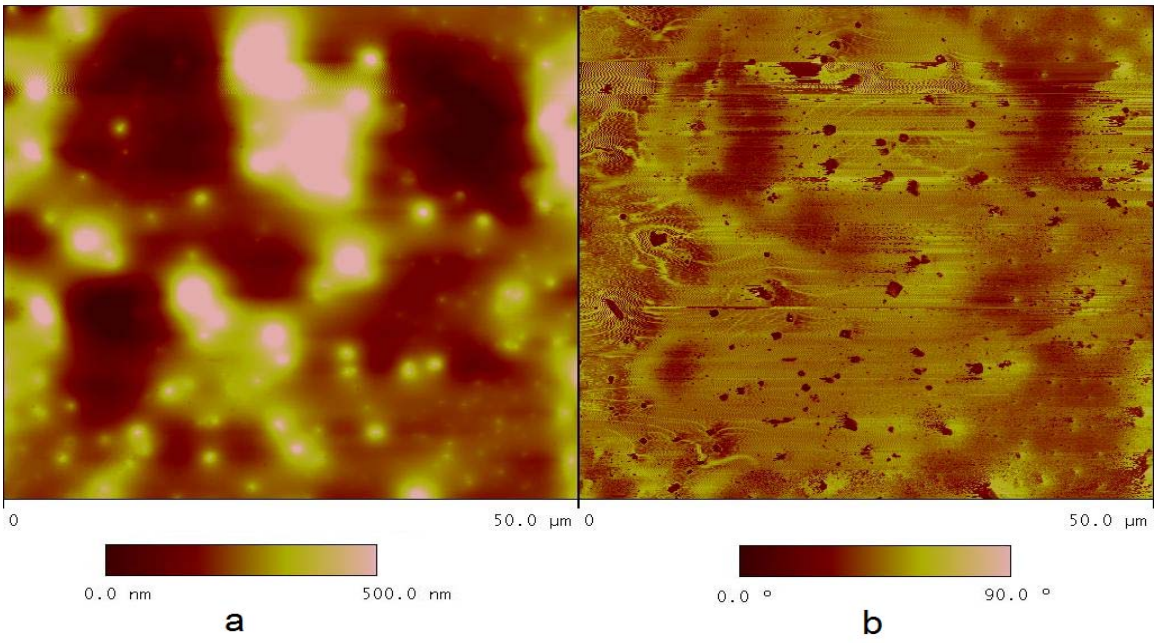

Fig. 19 - a) Height image and b) phase image of the toluene-washed mica surface

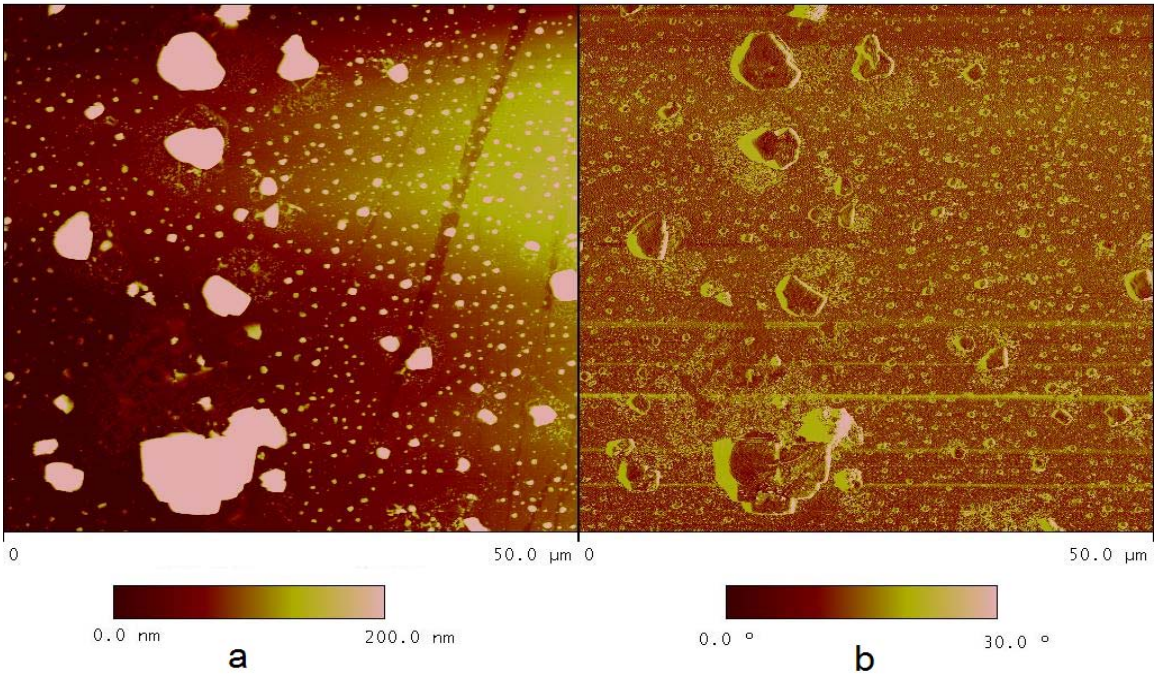

Fig. 20 - a) Height image and b) phase image of the decalin-washed mica surface

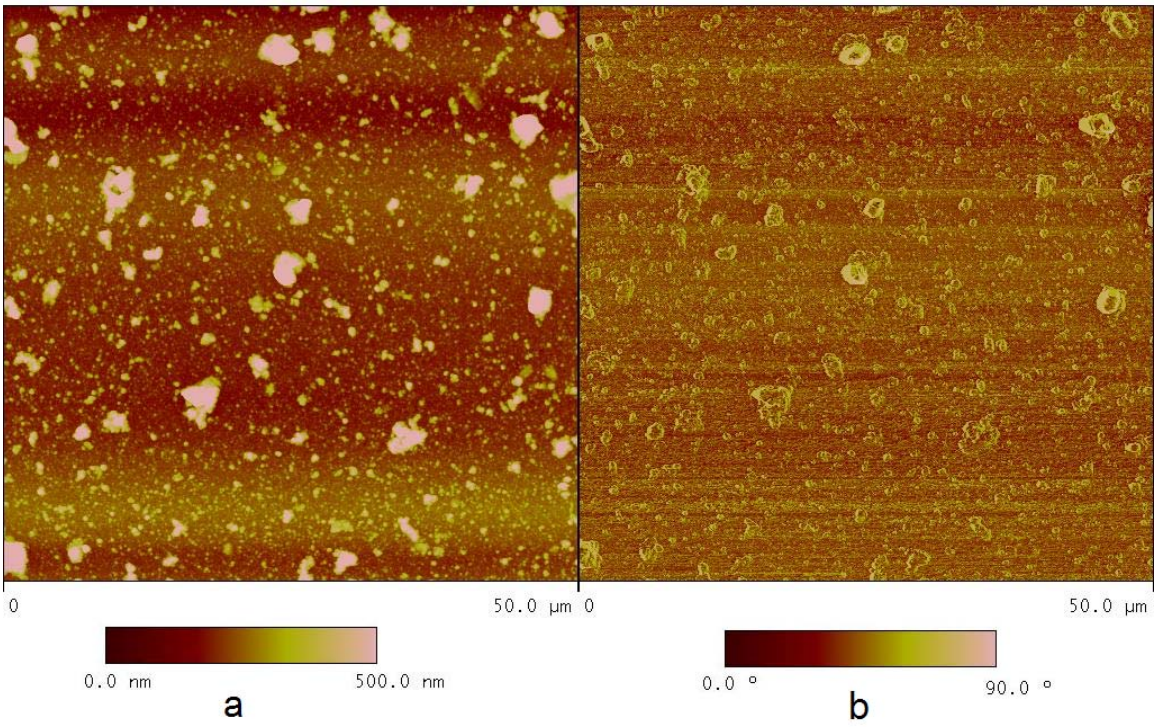

Fig. 21 - a) Height image and b) phase image of the cyclohexane-washed mica surface

	Mean Roughness (nm)	RMS (nm)	Z scale (nm)
Toluene	93.69	127.91	1157
Decalin	74.23	149.85	1645
Cyclohexane	55.77	111.75	1847

Table 7 - Roughness analysis of the samples imaged in Dry Mode

An attempt was made to relate the contact angles with mean roughness of the sample but we could find no correlation. Fig. 22 shows the graph of dry mode contact angles vs. mean surface roughness. Yang et al. (1999) also tried to relate the mean roughness with contact angles. They found that one of the oils they used, had a semi-logarithmic dependence of contact angle on mean surface roughness but the other oil did not show any such dependence.

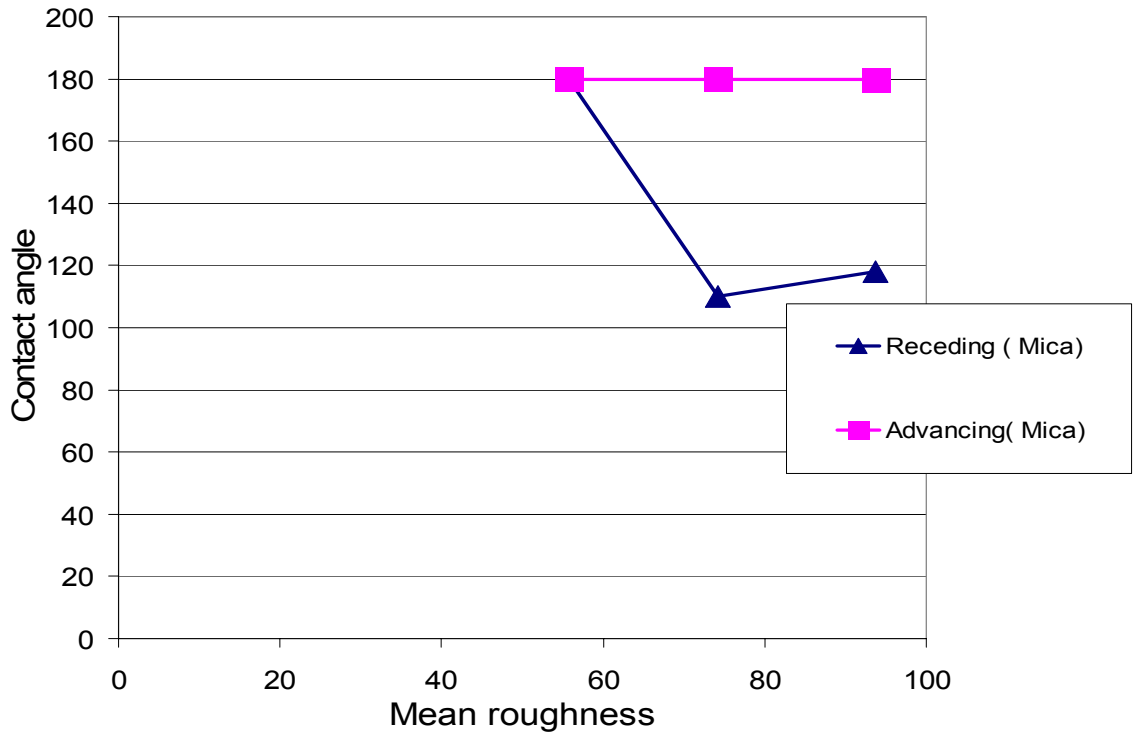

Fig. 22 - Advancing and receding contact angles vs. mean roughness (Dry Mode)

Imaging in water. After removing the excess solvent by drying, these samples were placed in water for a day and then imaged in water. When a small drop of water was introduced on the samples, there appeared to be some changes on the sample when viewed under an optical microscope. These images seem to have different topographical features as compared to the dry scans. Fig. 23 shows the toluene-treated sample imaged in water. Compared to Fig. 19, the height (and width) of the peaks are smaller. A lot of small peaks (white dots) are seen when imaged in water as compared to imaging in air. A lot of bare mica surface is visible in Fig. 23

and the image roughness and RMS goes down substantially. A similar change is observed in the case of the decalin-washed sample. The large crystal-like structure (Fig. 20) seems to get smaller in size. However, for the case of cyclohexane the peaks get larger. The images in water do not have sharp peaks as seen in the height images scanned in air, i.e., the tips of the adsorbed material were blunt. Buckley and Lord (2003) also found similar differences in the images when scanned in air and water. The roughness analysis of these images has been summarized in Table 8. The mean roughness and RMS was found to be highest for cyclohexane followed by decalin and toluene unlike the dry mode.

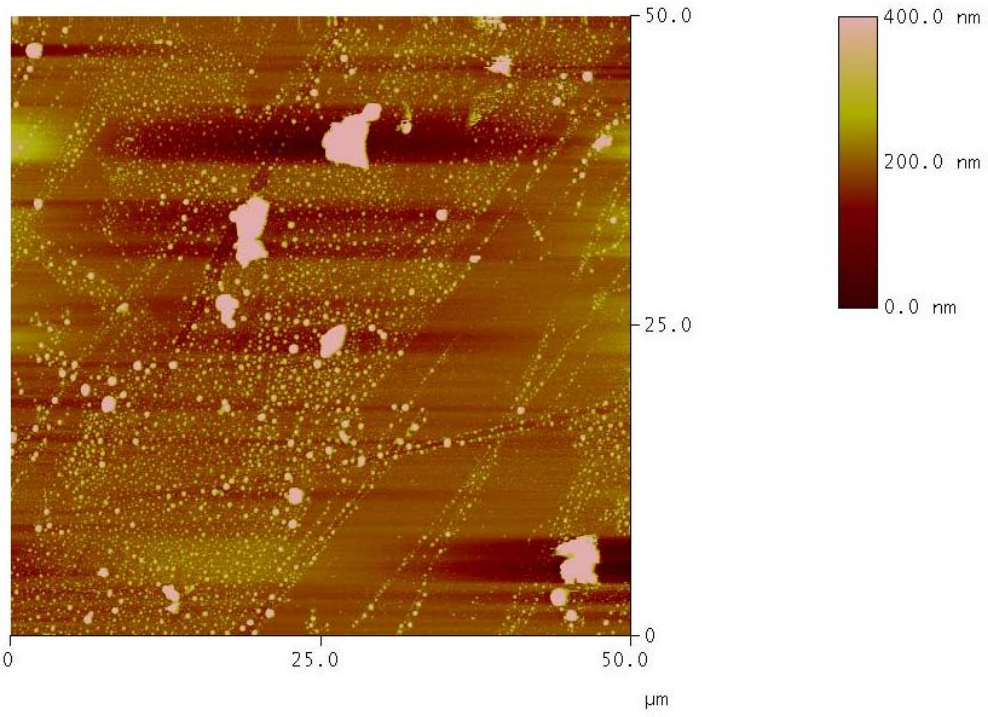

Fig. 23 - Toluene-washed sample imaged in water

	Mean Roughness(nm)	RMS (nm)	Z-scale (nm)
Toluene	37.63	87.22	1874
Decalin	97.05	134.55	2908
Cyclohexane	100.7	139.7	1200

Table 8 - Roughness analysis of images viewed in water (for Crude A)

Wet Mode. In order to overcome the effects of drying off the solvent, we followed a different procedure (wet mode) as detailed in the section 2. For each sample, 2 scans of sizes 1 x 1μm and 5 x 5μm were done at 4 different spots to have a better understanding of the surface; only the 1 x 1μm scans are shown here. Fig. 24 shows the toluene-treated sample imaged in the wet mode. The deposition is very uniform with peaks of height of approximately 60nm and diameter of approximately 25 nm though the adsorption is not continuous. Heights of the peaks are substantially lower in this wet mode as compared to the dry mode imaged in air or water. This suggests that drying off the solvent leaves behind some extra material. This extra deposition might be the solubilized material which is left behind during the evaporation of the solvent. It is also possible that because of capillarity, the adsorbed material may concentrate at few spots during drying and this might be the reason for the large non-uniformity in the dried samples.

Fig. 25 shows the decalin-treated sample. The adsorption in this case is not as uniform as in the case of toluene. Most of the peaks were approximately 40 nm in diameter with a few peaks of about 100 nm. The higher peaks could also be the result of accumulation of water from the thin film present between the sample and crude oil. The cyclohexane-treated sample (Fig. 26) showed deposits of approximately 100 nm in diameter. Table 9 lists the statistics of the adsorbed

material. The mean roughness, RMS and z scale are the highest for cyclohexane, followed by those for decalin and toluene. The roughness analysis and the AFM images both indicate that toluene and decalin are better solvents than cyclohexane. A possible explanation could be that asphaltenes molecules/aggregates are often surrounded by resin molecules, which render its solubility in oil. When these asphaltenes molecules adsorb on to the mineral surface and are subjected to different solvents, the resin molecules surrounding these asphaltenes dissolve better in toluene and decalin than in cyclohexane. This may be because of the aromatic nature of toluene and decalin. So the amount of the adsorbed components may be inversely related to the oil solubilizing capacity of the solvents.

Mica- Crude A	Mean Roughness (nm)	RMS (nm)	Z Scale (nm)
Toluene	5.1	3.9	54.7
Decalin	7.8	5.3	79.3
Cyclohexane	23.7	18.4	258

Table 9 - Roughness analysis of the mica samples imaged in the wet mode (for Crude A)

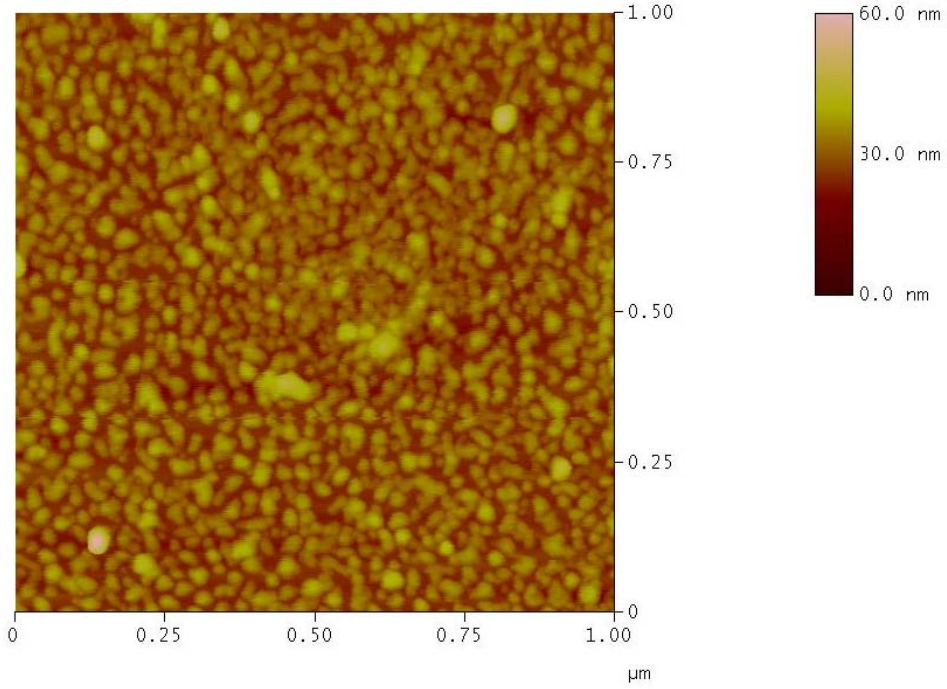

Fig. 24 - Toluene-washed sample (mica) imaged in the wet mode (for Crude A)

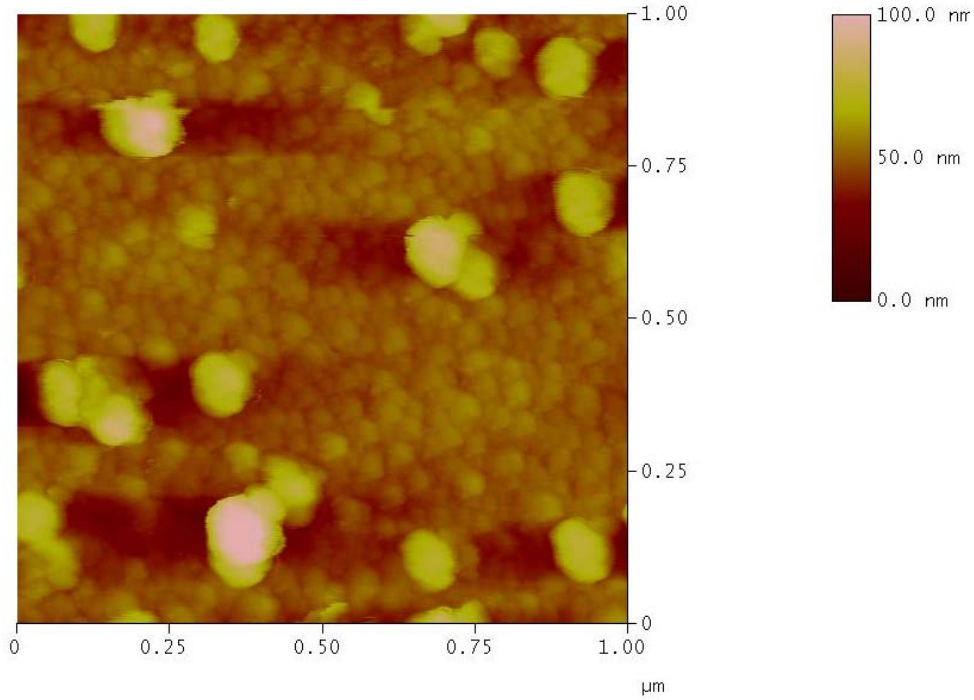

Fig. 25 - Decalin-washed sample (mica) imaged in the wet mode (for Crude A)

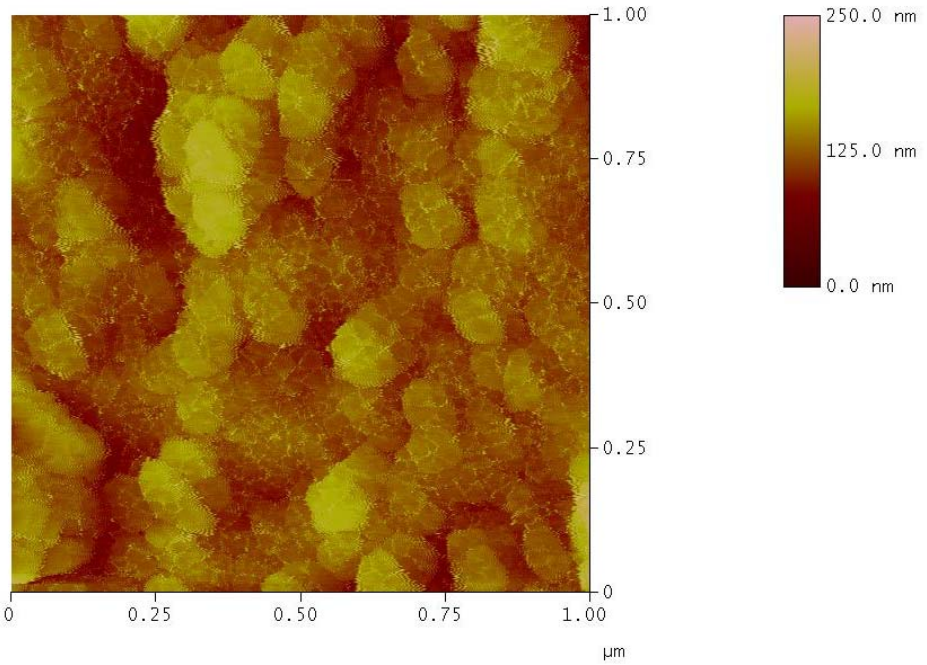

Fig. 26 - Cyclohexane-washed sample (mica) imaged in the wet mode (for Crude A)

A similar set of experiments was carried out with silicon as the substrate. Fig. 27 shows the toluene-treated silicon sample. The height and the diameter of the peaks are very similar to the toluene-treated mica surface (approximately 25 nm diameter). Fig. 28 shows the decalin-washed sample. The topography is close to the toluene-treated sample except for a few peaks which seem to connect to form bigger oil patches. When compared to the decalin-washed mica surface, the grain size is much smaller (almost half) in this case. Fig. 29 shows the cyclohexane-treated surface. The adsorbed oil patches are of different sizes varying from 20 nm to 100nm. All the three silicon samples show lower adsorption than the corresponding mica surfaces but they follow the same trend (i.e., the adsorption being the highest for cyclohexane and the lowest for toluene). Table 10 summarizes the roughness analysis for the silicon samples. Similar to mica surfaces, the mean roughness and RMS are highest for cyclohexane-washed sample followed by decalin and toluene-washed samples.

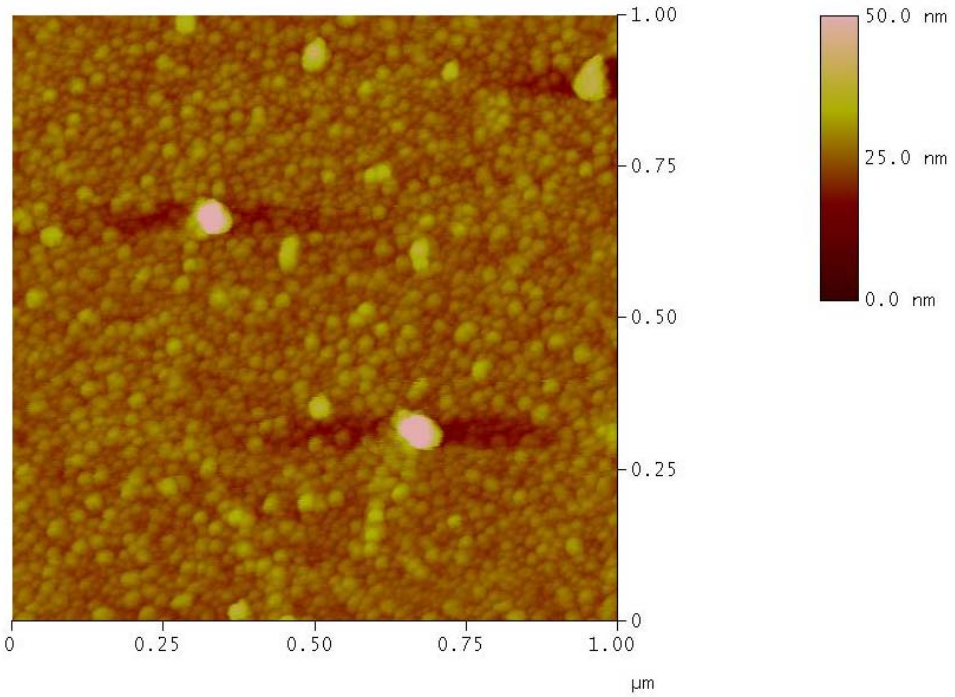

Fig. 27 - Toluene-washed sample (silicon) imaged in the wet mode (for Crude A)

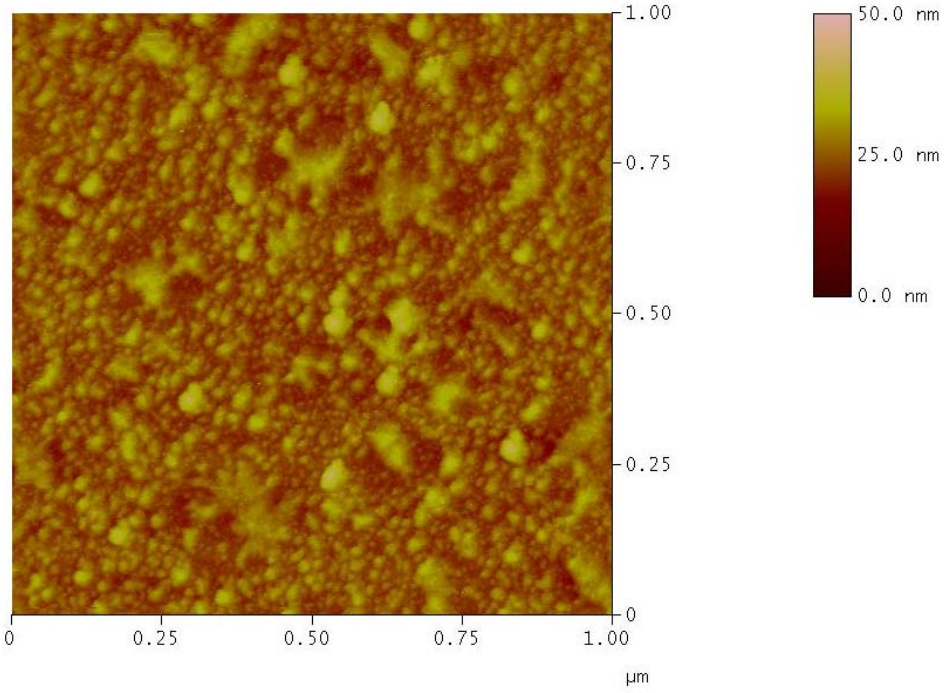

Fig. 28 - Decalin-washed sample (silicon) imaged in the wet mode (for Crude A)

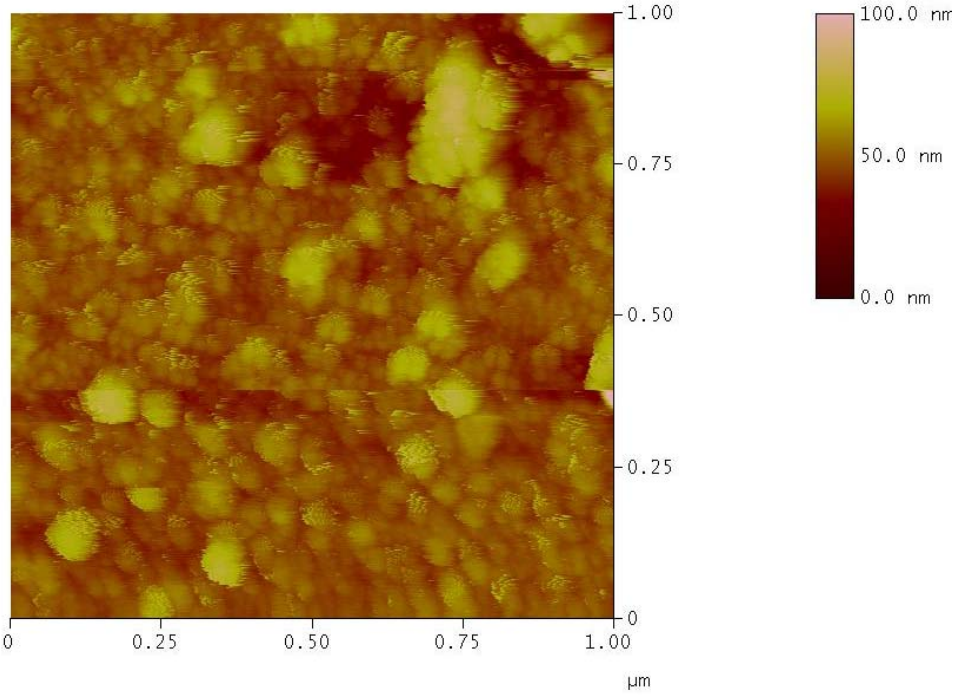

Fig. 29 - Cyclohexane-washed sample (silicon) imaged in the wet mode (for Crude A)

Silicon-Crude A	Mean Roughness (nm)	RMS (nm)	Z Scale (nm)
Toluene	3.4	2.0	52.3
Decalin	3.6	2.7	48.1
Cyclohexane	15.7	11.6	124

Table 10 - Roughness analysis of the silicon samples imaged in the wet mode (for Crude A)

The same set of experiments was repeated with a different crude oil, Crude B. Fig. 30 shows the height image of a mica sample aged in crude B and treated with toluene (wet mode). The sample exhibits uniform adsorption except for a few peaks which are shown as white patches. Fig. 31 shows a decalin-washed sample. The adsorbed materials have diameters varying from 25 nm to 75 nm. The cyclohexane-washed sample (Fig. 32) shows adsorption of large clusters and the peaks are larger. The roughness analysis of these figures has been summarized in Table 11. Similar to Crude A, the mean roughness, RMS and z-scale were found to be highest for cyclohexane followed by decalin and toluene. These experiments were also performed with silicon as the substrate and the trends observed were very similar to that of mica. The results are also summarized in Table 12.

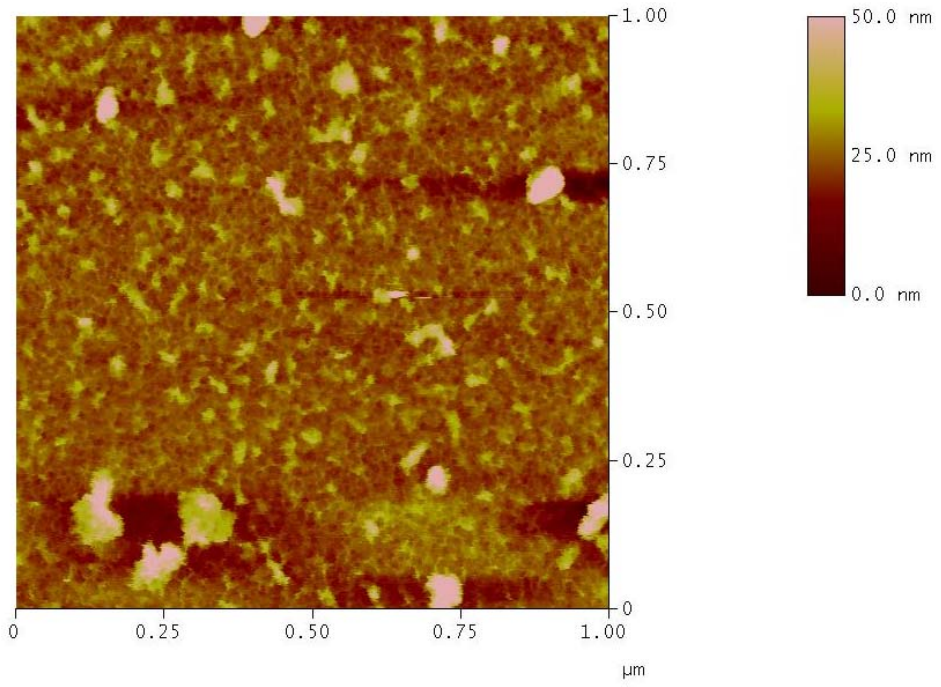

Fig. 30 - Toluene-washed sample (mica) imaged in the wet mode (for Crude B)

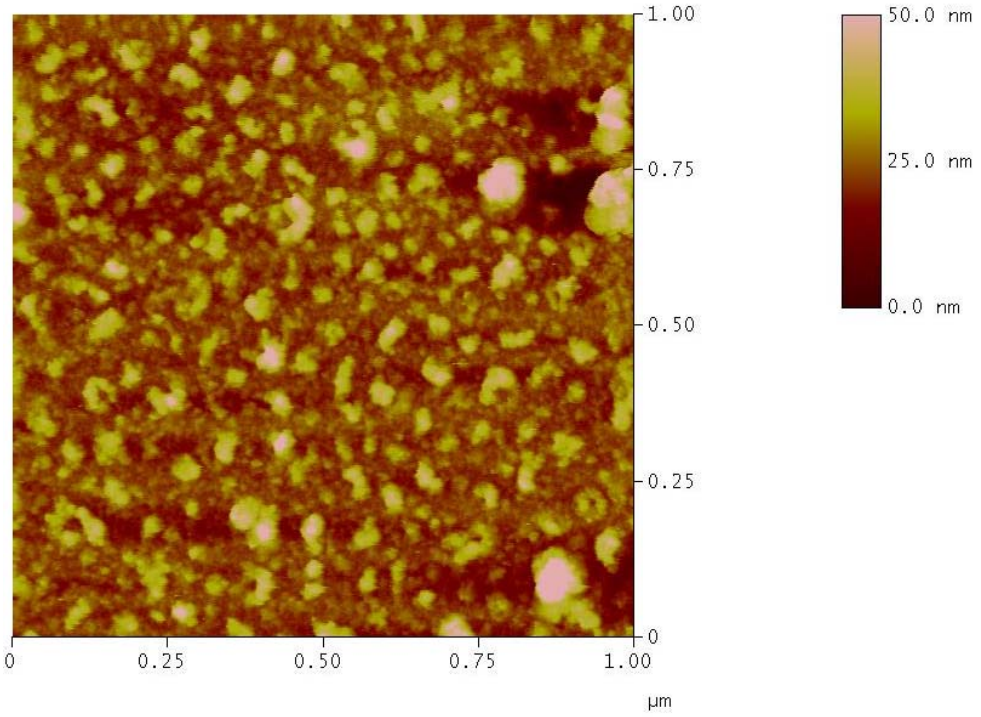

Fig. 31 - Decalin-washed sample (mica) imaged in the wet mode (for Crude B)

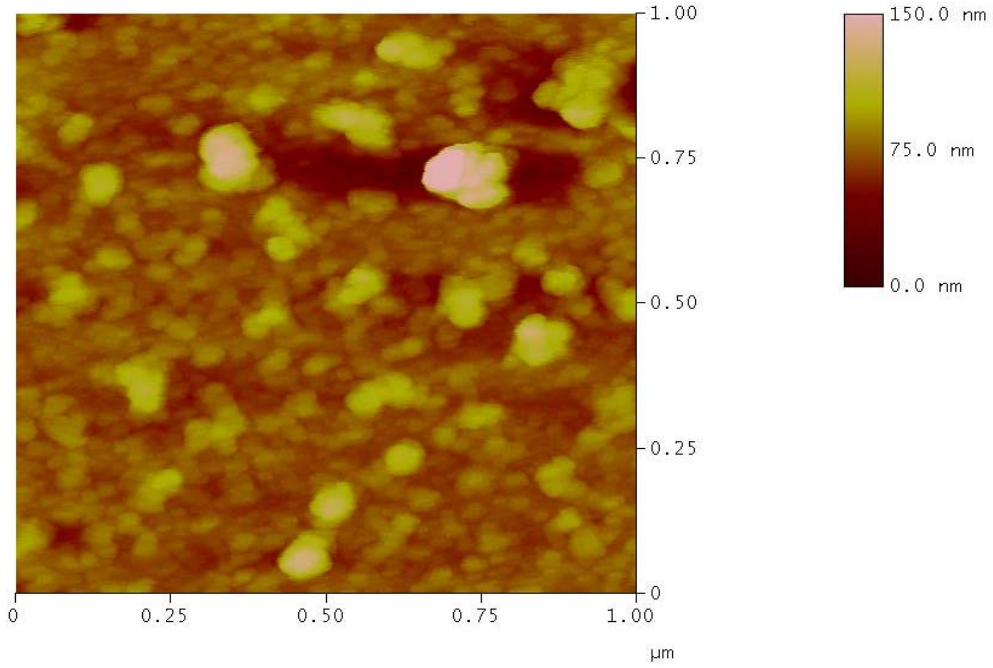

Fig. 32 - Cyclohexane-washed sample (mica) imaged in the wet mode (for Crude B)

Mica-Crude B	Mean Roughness (nm)	RMS (nm)	Z Scale (nm)
Toluene	8.5	5.6	98.6
Decalin	8.7	6.0	101.5
Cyclohexane	20.8	13.2	212

Table 11 - Roughness analysis of the mica samples imaged in the wet mode (for Crude B)

Silicon-Crude A	Mean Roughness (nm)	RMS (nm)	Z Scale (nm)
Toluene	5.5	3.9	67.8
Decalin	7.5	4.8	112.5
Cyclohexane	14.5	10.9	138

Table 12 - Roughness analysis of the silicon samples imaged in the wet mode (for Crude B)

For both Crude A and Crude B, it was seen that the diameter and the height of the adsorbed patches on both mica and silicon surfaces are higher for cyclohexane than for toluene and decalin. Also the roughness parameters (average height, RMS and Z scale) are highest for cyclohexane, followed by decalin and toluene. Figs. 33 and 34 show the contact angles as a function of surface roughness for Crude A and Crude B, respectively. As the mean roughness of the images in wet mode increases, the advancing and receding contact angles increase, for both

oils and both minerals. However, a unique correlation could not be developed. Also the hysteresis (difference between advancing and receding angles) could not be directly related to the mean roughness of the sample.

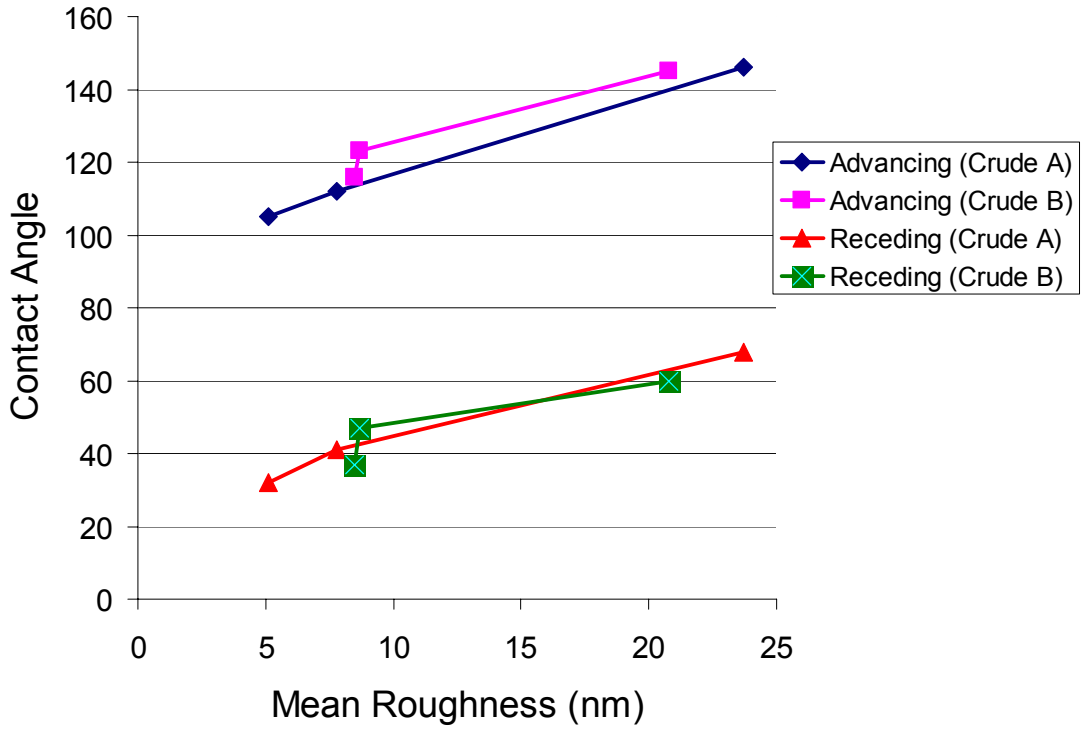

Fig. 33 - Contact angle vs. mean surface roughness of mica

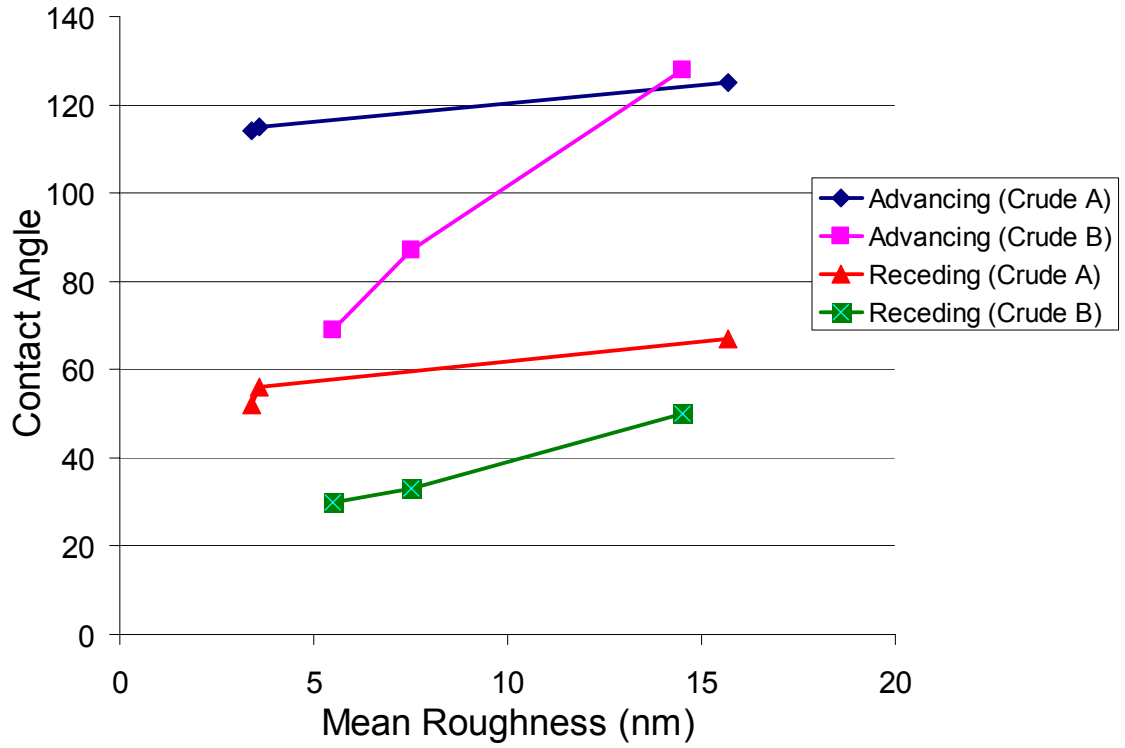

Fig. 34 - Contact angle vs. mean surface roughness of silicon

Silicon Scratch Technique. The roughness analysis is not a good measure of the adsorbed amount because roughness is defined as the average difference from the mean height. It is actually possible that the tip never sees the substrate (mica/silicon in this case) because there might be a continuous covering of the adsorbed organics on the substrate. In order to get the actual value of the thickness of adsorbed materials, we use the scratch technique as described before.

Fig. 35 shows the scratched silicon image for the toluene-treated silicon sample for Crude A. The top right of the image shows the scratched area which has no deposition. Section analysis at different spots on the image was used to get an average value of the thickness of the oil deposits. Table 13 shows the average thickness for the three differently treated samples. The average thickness of the oil patches was highest for the cyclohexane-washed sample, followed

by decalin and toluene, which implies that toluene is a better solvent as compared to decalin and cyclohexane. The state of adsorption is shown very well by Table 9 and 12 together.

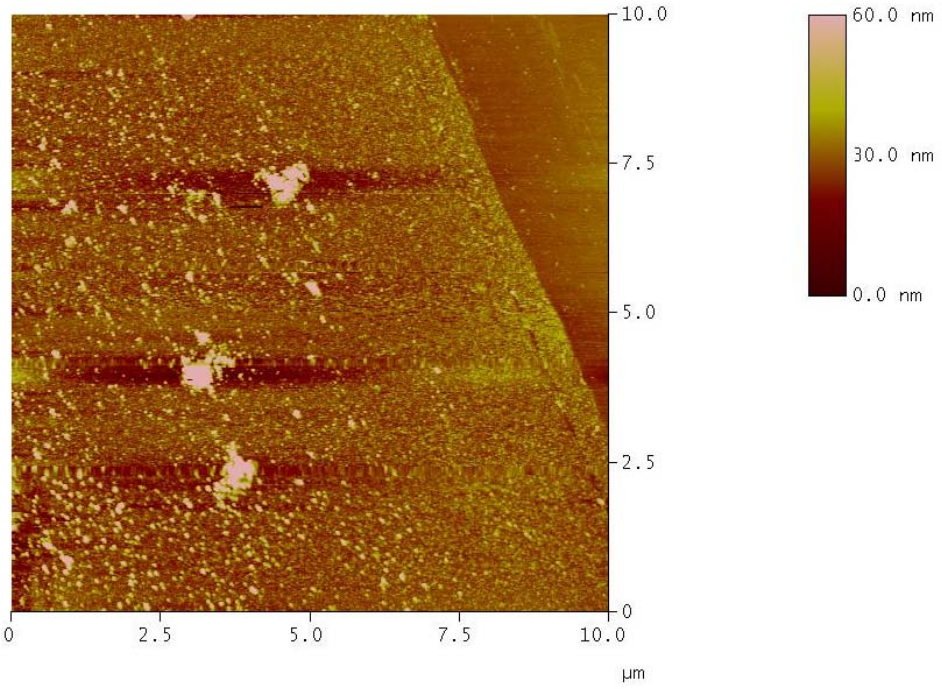

Fig. 35 - Scratched silicon sample which has been treated with Crude A and toluene.

Mica	Average height (nm)
Toluene-treated sample	9.11
Decalin-treated sample	29.1
Cyclohexane-treated sample	66.9

Table 13 - Average height of silicon substrates treated with Crude A.

Fig. 36 shows the contact angles as a function of the average height of the adsorbed films obtained form the silicon scratch technique. Both the advancing and receding contact angles

increase almost linearly with average height. The correlation with average height is better than that with the mean roughness shown in Fig. 34.

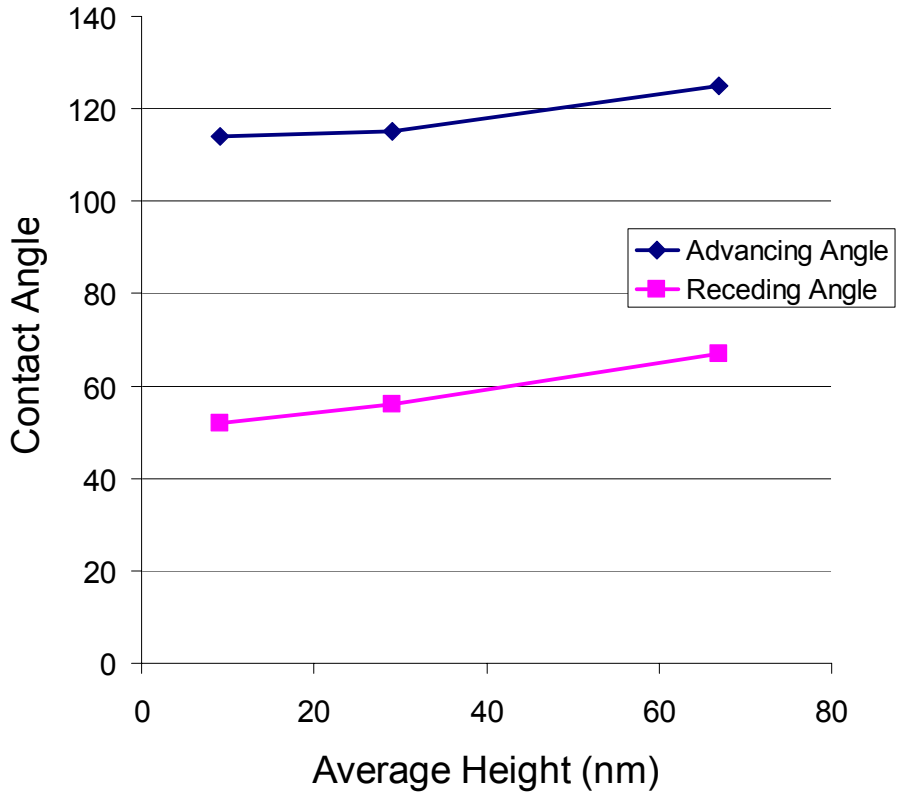

Fig. 36 - Contact angle vs. average height of adsorbed film on silicon (for Crude A)

Force Measurements. A large number of force measurements were conducted using a 1 μm COOH terminated borosilicate particle at several spots in order to get an estimate of the adhesive forces. Fig. 37 shows the force of adhesion for 6 treated samples and a COOH terminated mica surface, which was used as a reference. The force of adhesion or the jump-off contact force has been modeled as being proportional to the surface energy of the sample. Van der Vegte and Hadziioannou (1997) have measured the force of attraction between the COOH surface and COOH tip in ethanol and the surface energy was found to be 4.5mJ/m^2. We carried out a similar experiment and the surface energy was measured as 3.7mJ/m^2. The force of adhesion was found

to be the highest for decalin. This is observed for both mica and silicon surfaces. The adsorbed materials in case of decalin may have characteristics similar to that of resins, which have the highest force of adhesion among the different SARA fractions (shown in next section).

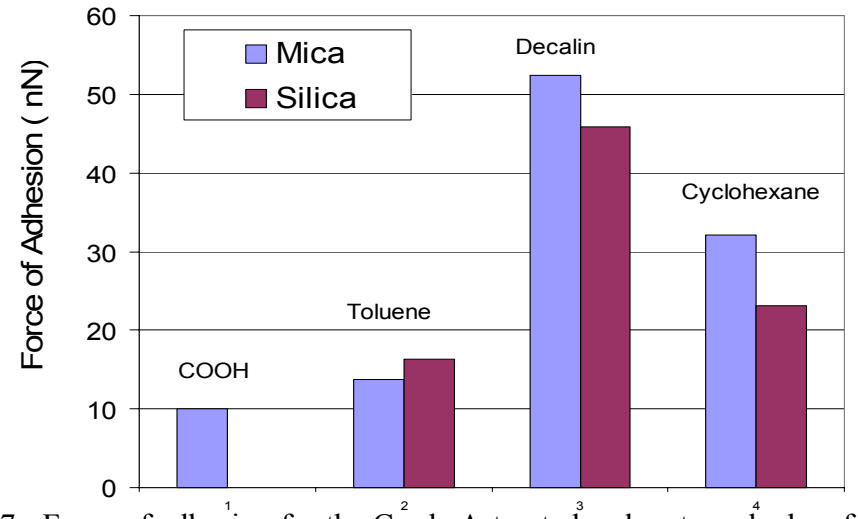

Fig. 37 - Force of adhesion for the Crude A-treated, solvent-washed surfaces

SARA Fractions. Fig. 38 shows the force of adhesion for the different SARA fractions (solubilized in toluene) along with that of the Crude A (washed subsequently in toluene). The force of adhesion for the case of the whole oil is very close to the one obtained from the apshaltene solution. It can be inferred that the adsorbed material left behind when the cores/samples are washed with toluene is primarily asphaltenic in nature.

Another important thing observed was that the force was the largest for the case of resins. It is believed that resins are more liquid like than asphaltenes. So, when the tip approaches the surface, resins engulf a larger area of the spherical tip than the other fractions and thus have a larger force of adhesion. This may be also due to the high compressibility of resin films adsorbed. Asphaltenes are envisioned as crystalline and thus have a relatively smaller area of contact. The force of adhesion for aromatics is the least. The trend is similar for mica and silicon

surfaces. The force of adhesion for asphaltenes was similar for both mica and silicon substrates. This might imply that the adsorbed asphaltenes on both mica and silicon are very similar. It was also observed that resins have the highest jump to contact force (not shown). For the case of asphaltenes and aromatics, the jump to contact force was negligible. For asphaltenes, small long range repulsive forces were also observed. AFM force measurements give us insights into the nature of adsorbed materials.

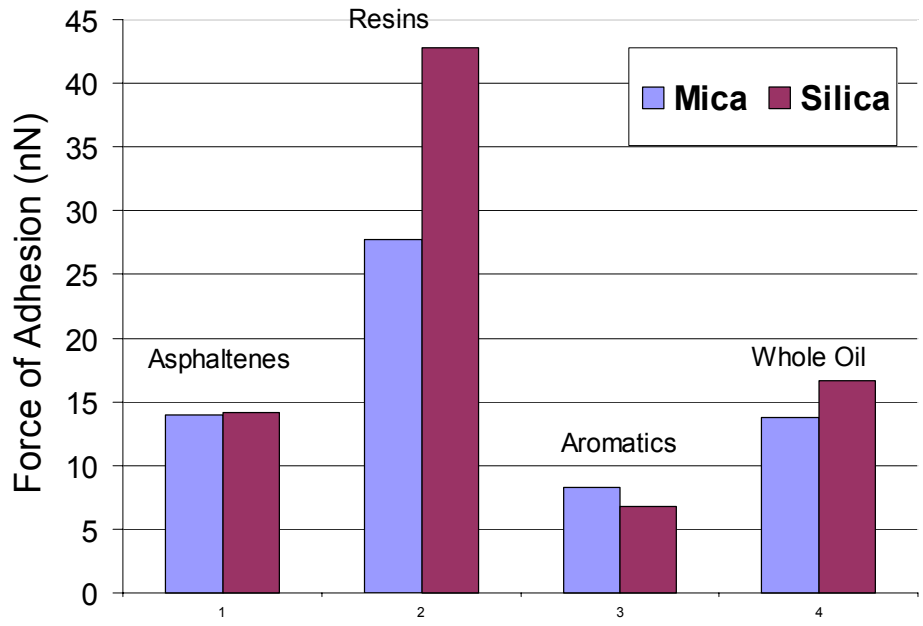

Fig. 38 - Force of Adhesion for the different SARA fractions

New Relative Permeability Model. The model is described in terms of its two-phase, three-phase and four-phase features.

Two-Phase Relative Permeability: Gas. We adopt the two-phase relative permeability for the gas phase proposed by Jerauld (1997), i.e.,

$$K_{rg} = \frac{(1+C_{g2})\,S_g^{*C_{g1}}}{1+C_{g2}S_g^{*C_{g1}(1+1/C_{g2})}}, \qquad (26)$$

where

$$S_g^* = \frac{S_g - S_{gt}}{1 - S_{gt} - S_{org} - S_{wr}}. \qquad (27)$$

Eq. 26 involves two parameters: C_{g1} and C_{g2} , which can be made functions of phase density for compositional consistency. If C_{g2} is assumed to be zero, then the gas relative permeability calculation is similar to that in the modified Corey model. It is apparent from the above equation that at low S_g values, the numerator dominates while at high S_g values, the second term in the denominator dominates. So the second term in the denominator can be treated as the contributions of the small pores to the relative permeability and is so designed that it gives a zero slope at S_g = 1. This is also consistent with the idea that the gas, being the most non-wetting phase, enters the big pores first and then the smaller pores. The capillary number dependence is ignored because either gas or the second liquid displaces oil or is displaced by water.

Eq. 27 involves the term S_{gt} (trapped gas saturation). The trapped gas saturation influences the amount of miscible injectant (gas) retained in the reservoir that is not available for oil displacement. S_{gt} is defined as (Jerauld, 1997):

$$S_{gt}(S_g^{\max}) = \frac{S_g^{\max}}{1 + (1/S_{gr} - 1)S_g^{\max 1+b(S_{gr}/(1-S_{gr}))}}, \qquad (28)$$

where $S_g^{\max}$ is the maximum gas saturation that has occurred at that location at any time and *b* is empirically determined. This equation reduces to Land's equation (Land, 1968) when *b* equals 0. However, *b* should be less than or equal to 1 due to physical constraints. The above equation also satisfies the physical constraints: the trapped gas saturation is always less than $S_g^{\max}$ At high values of $S_g^{\max}$, the trapped gas saturation approaches the residual gas saturation, S_{gr} while it approaches $S_g^{\max}$ at low $S_g^{\max}$ values. The problem associated with this model is that one has to keep track of maximum gas saturation in each grid block during simulation (but this can be

easily handled). So it is possible that two grid blocks having the same gas saturation can have different permeabilities as they can have different $S_g^{\max}$.

Two-Phase Relative Permeability: Oil. The oil relative permeabilities with respect to water and gas are given as:

$$K_{row} = K_{ro}^0 \left(\frac{S_o - S_{orw}}{1 - S_{wr} - S_{orw}} \right)^{C_{ow}} \tag{29}$$

$$K_{rog} = K_{ro}^0 \left(\frac{S_o - S_{org}}{1 - S_{wr} - S_{org}} \right)^{C_{og}}, \tag{30}$$

where S_{org}, S_{orw}, C_{ow} and C_{og} are functions of capillary number. At the miscible front in a multi-contact gas miscible process, the interfacial tension (IFT) becomes low resulting in high capillary number, which is needed to mobilize the residual oil in small pores. So, the change in IFT leads to changes in relative permeability.

Two-Phase Relative Permeability: Water. The water relative permeabilities with respect to oil and gas are calculated as,

$$K_{rwo} = K_{rw}^0 \left(\frac{S_w - S_{wr}}{1 - S_{wr} - S_{orw}} \right)^{e_{wo}}, \tag{31}$$

$$K_{rwg} = K_{rw}^0 \left(\frac{S_w - S_{wr}}{1 - S_{wr} - S_{org} - S_{orw}} \right)^{e_{wg}} \tag{32}$$

Capillary effects are not important for the flow of water. The exponents, e_{wo} and e_{wg} can be made functions of density such that as miscibility is reached, S_{org} tends to decrease and the relative permeabilities of water with respect to oil and gas approach each other.

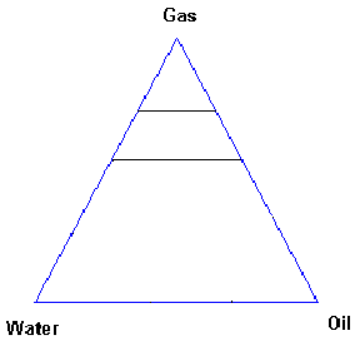

Fig. 39 - Isoperm sketches of gas relative permeability in a three-phase system.

Three-Phase Relative permeability: Gas. Gas is considered to be the most non-wetting phase with respect to oil and water. So K_{rg} is assumed to be a function of gas saturation only as given by Eq. 26. This implies that the isoperms will be horizontal, straight lines (if gas hysteresis is neglected) on a ternary diagram. Typical sketches of the gas isoperms are shown in Fig. 39.

Three-Phase Relative Permeability: Water. Water is considered to be non-wetting with respect to oil but wetting to gas. Water saturation both increases and decreases with respect to gas saturation during WAG floods. Because water is wetting with respect to gas, water will have little hysteresis. Water relative permeability, K_{rw} is assumed to be an arithmetic interpolation between K_{rwg} and K_{rwo} following Baker (1988) and Blunt (2000)

$$K_{rw} = \frac{S_o K_{rwo}(S_w) + S_g K_{rwg}(S_w)}{S_o + S_g}. \qquad (33)$$

This simple saturation-weighted approximation captures the basic features of water relative permeability in mixed-wet reservoirs. If either oil or gas saturation is zero, the three-phase water relative permeability equals two-phase relative permeability. Moreover, as the miscibility limit is reached, the resulting water permeability is a function of water saturation alone. Some typical isoperms are shown in Fig. 40.

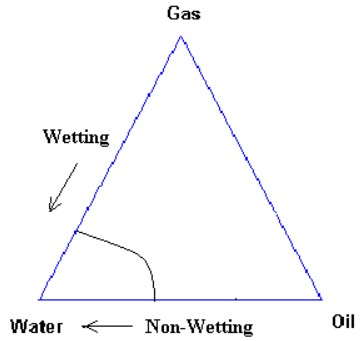

Fig. 40 - Isoperm sketches of water relative permeability in a three-phase system.

Three-Phase Relative Permeability: Oil. Oil is wetting with respect to gas and water except in the microporosity. At low oil saturations and sufficiently high water saturations, oil relative permeability depends only on the oil saturation because oil is the most wetting fluid. Howover, at low water saturations, water is present in the microporosity and competes with oil for the smaller-sized pores. Thus the oil relative permeability depends on the total liquid saturation in the limit of low water and high oil saturations. For purposes of simplicity, the oil permeability is approximated as,

$$K_{ro} = Min\,(K_{row}(S_o), K_{rog}(S_o+S_w)). \qquad (34)$$

The first term is lower than the second term in the right hand side of Eq. 34 in most of our simulations. Typical sketches of oil relative permeability are shown in Fig. 41.

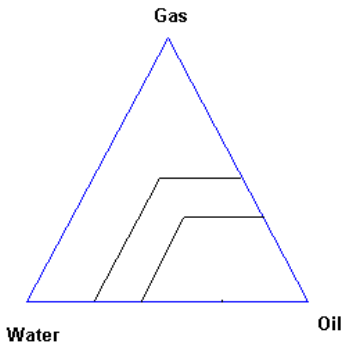

Fig. 41 - Isoperm sketches of oil relative permeability in a three-phase system.

Four-Phase Relative Permeability. In this work, the gas phase (phase 3) and the second liquid phase (phase 4) are treated as one combined pseudo-phase (g). The properties of the combined pseudo-phase is calculated and then divided between phases 3 and 4 based on their saturations as follows:

$$S_g = S_3 + S_4 \tag{35}$$

$$\rho_g = (\rho_3 * S_3 + \rho_4 * S_4)/S_g \tag{36}$$

$$K_{r3} = K_{rg}(S_g)* S_3 / (S_3 + S_4) \tag{37}$$

$$K_{r4} = K_{rg}(S_g)* S_4 /(S_3 + S_4) \tag{38}$$

In Guler *et al.* (2001) model, a similar approach was applied; however, the second liquid was combined with oil. That approach would decrease the importance of the nonlinearity in relative permeability because many cells contained water, oil and second liquid in our case studies.

Comparison of the New Model with the Guler *et al.* (2001) Model. The relative permeabilities of different phases were calculated using the new model and compared with those of Guler *et al.* model (2001). The dependence of oil relative permeability on capillary number has been ignored in these examples for the sake of simplicity. The relative permeabilities for the three phases were calculated along the path shown in Fig. 42.

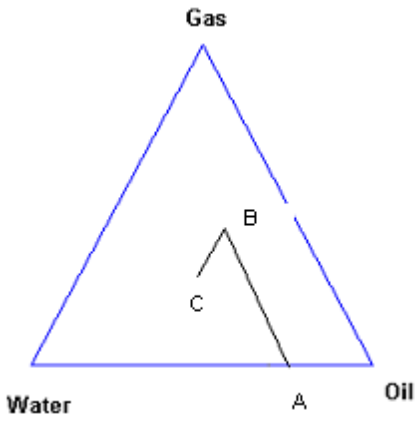

Fig. 42 - Saturation path in a three-phase system.

From A to B, the value of water saturation was held constant at 0.3. And in this case, the value of *Sg* was varied from 0.05 to 0.39. At point B, the value of oil saturation was held constant and the gas saturation was varied from 0.39 to 0.21. The values computed from the two different models are plotted in Figs. 43-45. The comparison illustrates only the three phase relative permeabilities and not the four phase effects. The various parameters used in the comparison are listed in Table 14. It is also assumed that the endpoint relative permeabilities are the same for both two-phase and three-phase flows.

Table 14 - Dimensionless Parameters Used to Compare the Guler *et al*. and New Models

S_{org}, S_{orw}	0.2
S_{wr}	0.25
S_{gr}	0.05
K_{ro}^{0}	0.71
K_{rw}^{0}	0.21
K_{rg}^{0}	1
C_{ow}, C_{og}	2.5
e_{wo}, e_{wg}	1.5
C_{g1}	2.5
C_{g2}	0
b	0

Fig. 43 shows the values of oil relative permeability for the two different models. As seen from the graph, the values predicted by the new model is lower than that by the Guler *et al.*

model possibly due to the fact that the Guler *et al.* model is more suitable for the water-wet rocks. It can also be seen from Eq. 34 that the value of $K_{row}(S_o)$ is always the smaller value of $K_{row}(S_o)$ and $K_{rog}(S_o+S_w)$, which implies that K_{ro} depends only on the oil saturation along the path used for the calculations. Moreover, along BC the value of oil saturation is constant, so the K_{ro} is seen as a horizontal line. Fig. 44 compares the values of water relative permeability. For the Guler *et al.* model, from A to B, the values are constant. This is typical of a water-wet rock, where the water relative permeability depends on the water saturation alone, which is not the case in the new model. The values from the new model are a little higher as compared to the Guler *et al.* model. This is expected because the rock is water-wet in the Guler *et al.* model whereas in the new model the rock is mixed-wet. Fig. 45 compares the values of K_{rg}. The values from both models are similar. Note that when these values were calculated by using the new model, C_{g2} was taken to be zero and C_{g1} was assumed to be independent of gas density. Therefore, the gas relative permeabilities were handled in a way similar to that in the Guler *et al.* model.

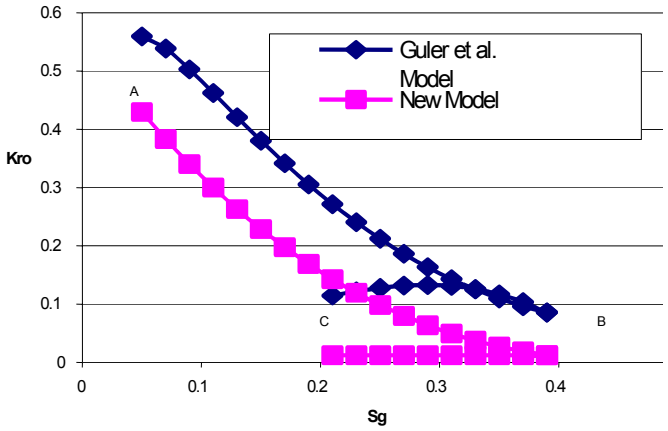

Fig. 43 - Comparision of oil relative permeabilitity from the Guler *et al.* and new relative permeability models.

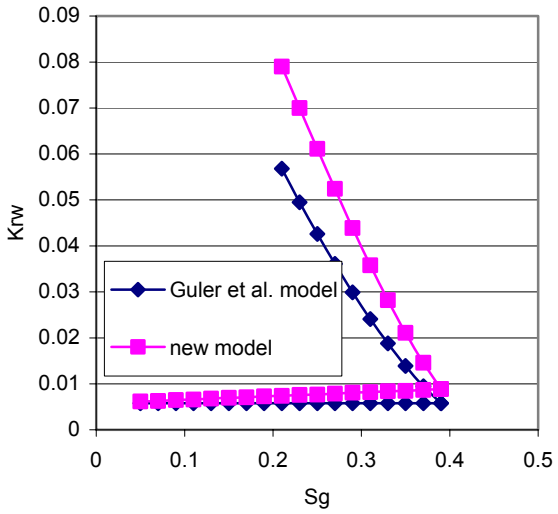

Fig. 44 - Comparision of water relative permeabilitity from the Guler *et al*. and new relative permeability models.

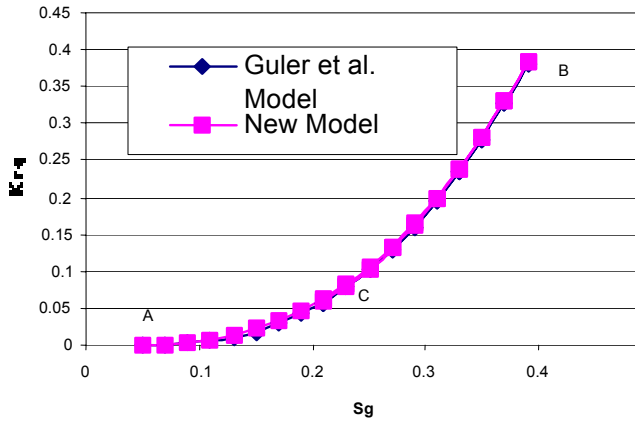

Fig. 45 - Comparision of gas relative permeabilitity from the Guler *et al*. and new relative permeability models.

Relative Permeability Formulation Effect. The new relative permeability model was incorporated into simulator UTCOMP. Oil recoveries for 100% CO2 and 85% CO2-15% NGL from the Guler *et al.* model is compared with their counterparts from the new model in Fig. 46 which indicates that the new model is more conservative than the Guler *et al.* model in the prediction of oil recoveries. Fig. 43 shows that the values of oil relative permeabilities from the new model are lower than their counterparts from the Guler *et al.* model because the new model

represents a more oil-wet rock. The difference in oil recovery is higher for 100% CO2 injection because it is more immiscible than the other injectant.

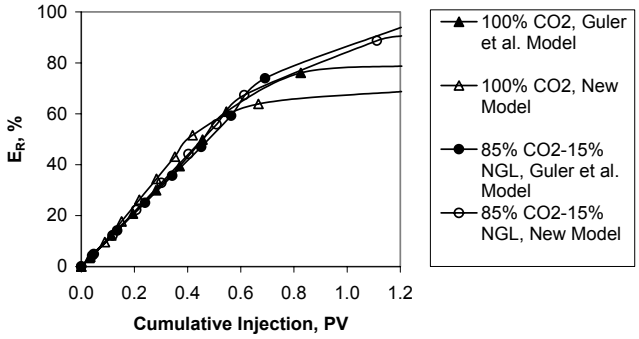

Fig. 46 - Oil recoveries at various times for 100% CO2 and 85% CO2 plus 15% NGL injections by using the Guler *et al.* and new relative permeability models.

Streamline Simulation

Waterflood. The developed streamline simulator (Strator) was verified both externally and internally for water injection. Externally, results from the Strator were compared with experimental data reported in the literature; internally, results at a certain dimensionless time from the Strator by using two different time steps were compared. After the Strator was verified, it was used to model waterflood at three different viscosity ratios.

The streamline simulation was run by using 20 by 20 grid blocks for time steps of 0.05 PV and 0.003 PV. Saturations along the diagonal direction are compared in Fig. 47, which shows that the curves are almost identical for 0.05 PV and 0.003 PV time step. The relative difference of the saturation values for certain grid blocks along the diagonal direction ranges from –1.05% to 0.00%, except for the first grid block at the front. The simulation results can be considered to be independent of the used time steps. Therefore, the streamline simulator for waterflooding is internally verified after time step has been decreased to be about one-seventeenth (about 0.003 PV) the initial one (about 0.05 PV).

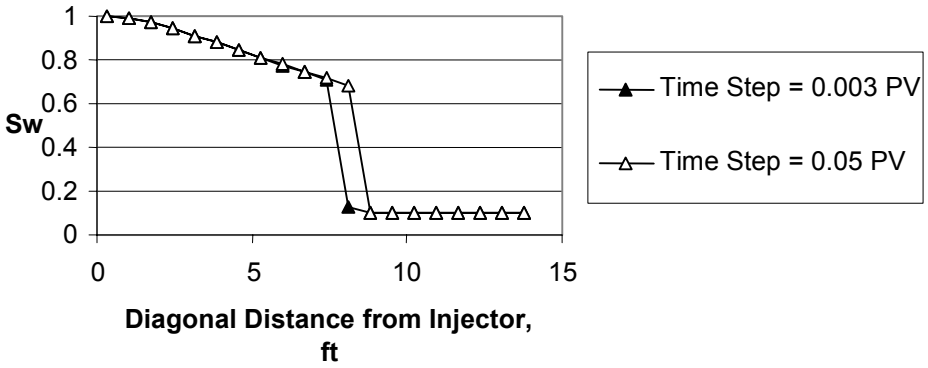

Fig. 47 - Water saturation along the diagonal direction at 0.33 PVI.

Mobility ratio was defined here as

$$M = \frac{k_w}{\mu_w} \cdot \frac{\mu_o}{k_o}, \qquad (39)$$

where k_w is the water relative permeability at the average water saturation of the water-contacted zone and k_o is the oil relative permeability ahead of the flood front. At the breakthrough, at the water-contacted zone, the average water saturation was found to be 0.83. In this example, the viscosity ratio is 1, so mobility ratio is

$$M = 0.88. \qquad (40)$$

Experimentally, the areal sweep efficiency at the breakthrough is 0.72 at this mobility ratio (Craig *et al.*, 1955). Note that the mobility ratio defined in Craig *et al.* (1955) is the reciprocal of the standard definition used here.

Using 20 x 20 grid blocks, the water saturation profile was determined at the breakthrough. The sweep efficiency is found to be 0.755, which is very close to the experimental result, 0.72. This is an external verification for the streamline simulator for waterflooding.

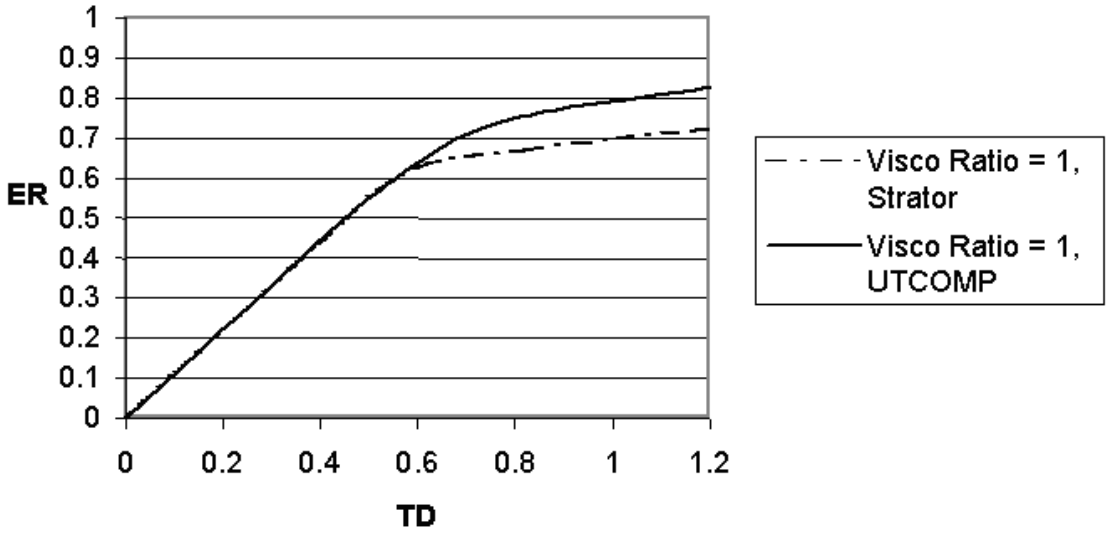

Fig. 48 Oil recovery when viscosity ratio is 1.

Streamline simulations were run by using 20 by 20 grid blocks for three different waterflood cases with viscosity ratios: 1, 33.28, and 66.56. Oil recovery is plotted against dimensionless time in Figs. 48-50, which show that results from Strator and UTCOMP are

comparable. The computational time for Strator is significantly less than that for UTCOMP. That is because large time steps can be taken for saturation updates along streamlines. The maximum time step that can be used in streamline simulation depends on the mobility ratio, physical dispersion, capillary pressure terms. Fig. 51 shows the in situ saturation distribution at 0.6 PVI. Small viscous fingers are observable on the saturation contours. The resolution of the fingers can be improved by using more than 20 x 20 grid blocks. The calculations have been conducted in heterogeneous fields. If the porous medium is heterogeneous, fingering is more severe.

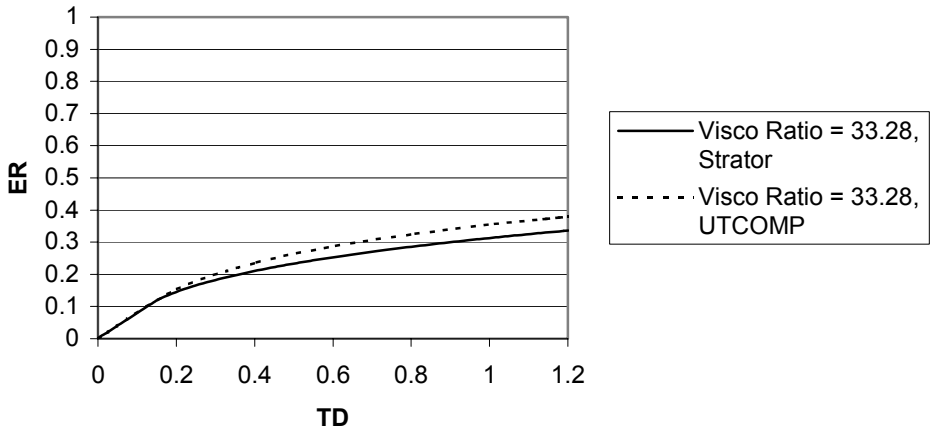

Fig. 49 Oil recovery when viscosity ratio is 33.28.

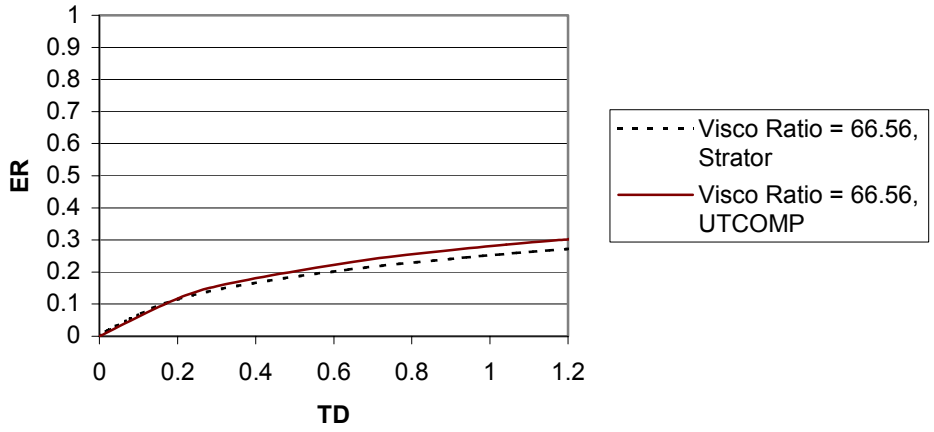

Fig. 50 Oil recovery when viscosity ratio is 66.56.

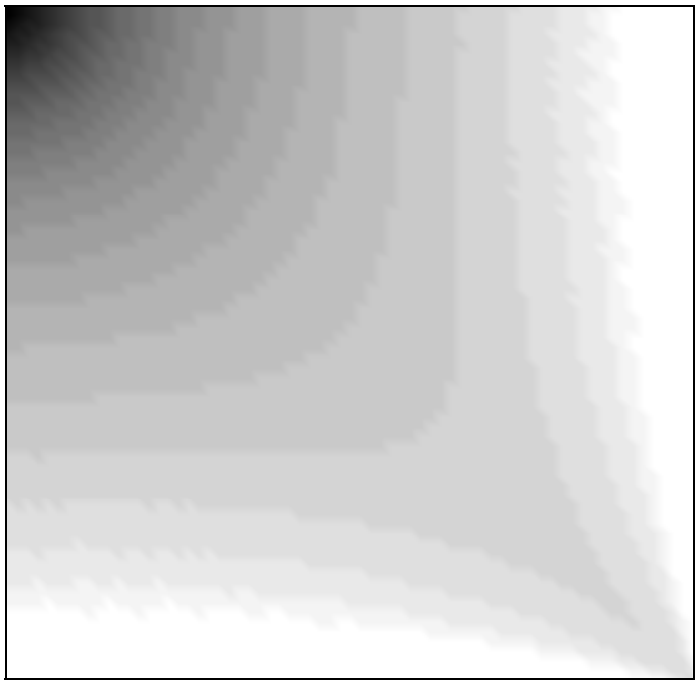

Fig. 51 Saturation distribution at 0.6 PVI.

Gasflood. To test gas injection simulation, injection of CO_2 into a reservoir with C_{16} was simulated at 700 psi and 69.38^{o}F. At 0.28 PVI, values of oil saturation obtained from Strator and UTCOMP are compared in Figs. 52 and 53, which show that the front generated by using Strator is sharper than that by using UTCOMP. The speed of solvent movement in the diagonal direction predicted by using Strator is faster than its counterpart by using UTCOMP while the results are comparable. Therefore, numerical dispersions from Strator are smaller than those from UTCOMP. Simulations were run in 70 by 70 grid blocks for the above case. Oil saturation at 0.47 PVI is shown in Fig. 54, which indicates a lot of viscous fingers.

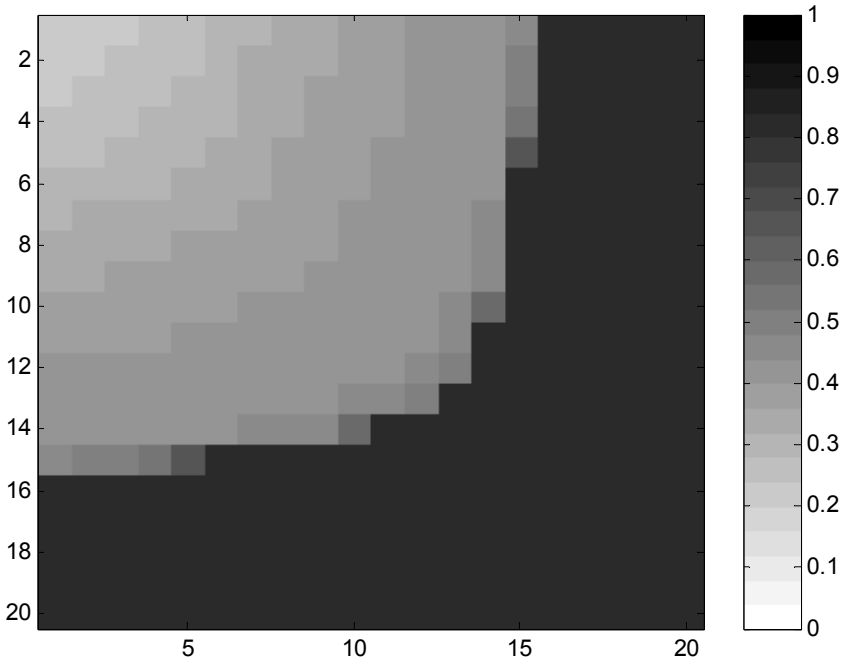

Fig. 52. Oil saturation from Strator at 0.28 PV injection of CO_2 into C_{16}

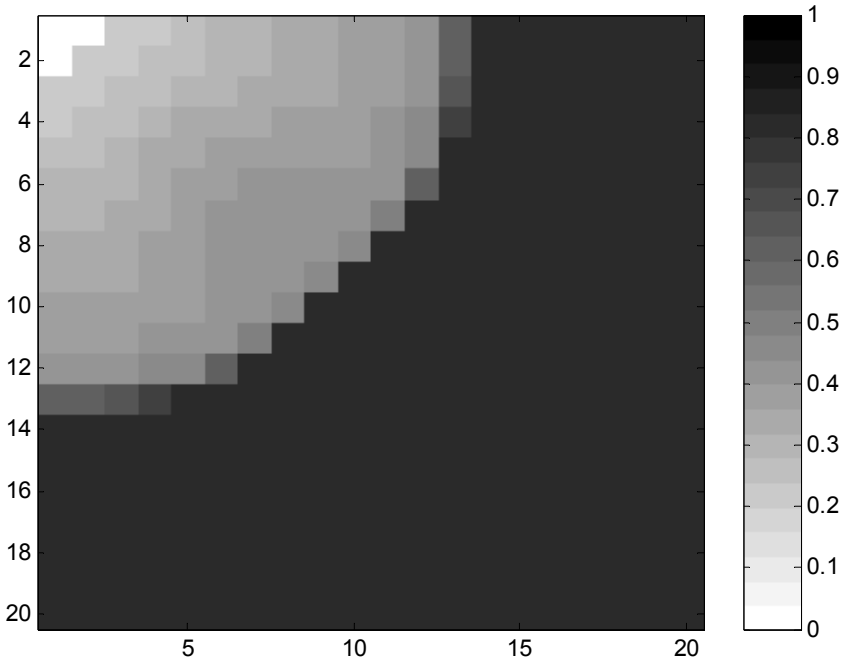

Fig. 53. Oil saturation from UTCOMP at 0.28 PV injection of CO_2 into C_{16}

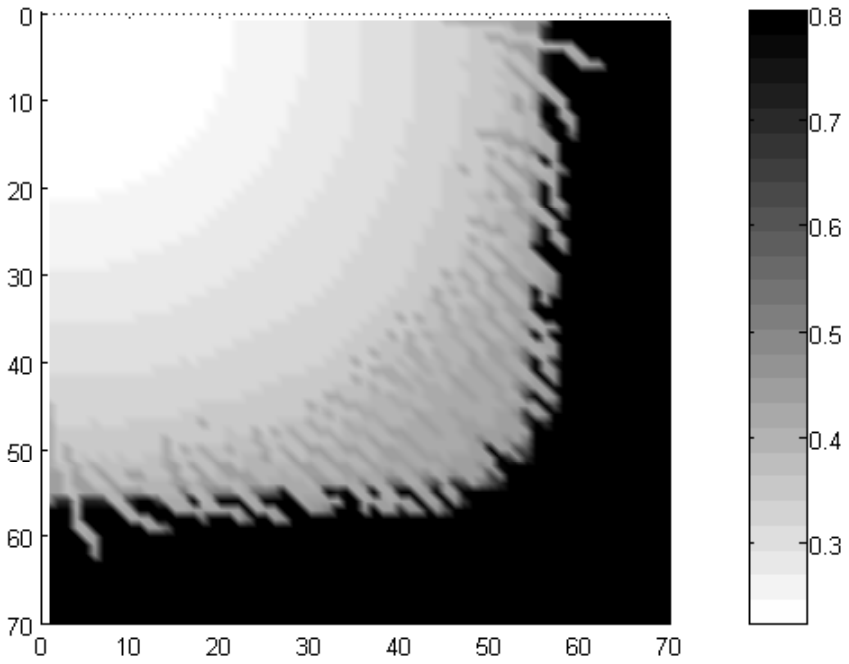

Fig. 54. Oil Saturation at 0.47 PVI

Simulations were run for 50-50 injection of PBG and NGL into a reservoir with Shrader viscous oil. Oil, gas, and second non-aqueous liquid saturations are shown in Figs. 55-60, which indicates that four phases can be simulated by Strator. This simulations show viscous fingering in these gasflood even with 20x20 grids. These simulations take a 366-MHz Pentium II computer 5 minutes and 21 seconds to run up to 1.2 PV by using Strator and about two hours to run up to 0.6 PV by using UTCOMP. Therefore, the speedup factor is about 43 in this case.

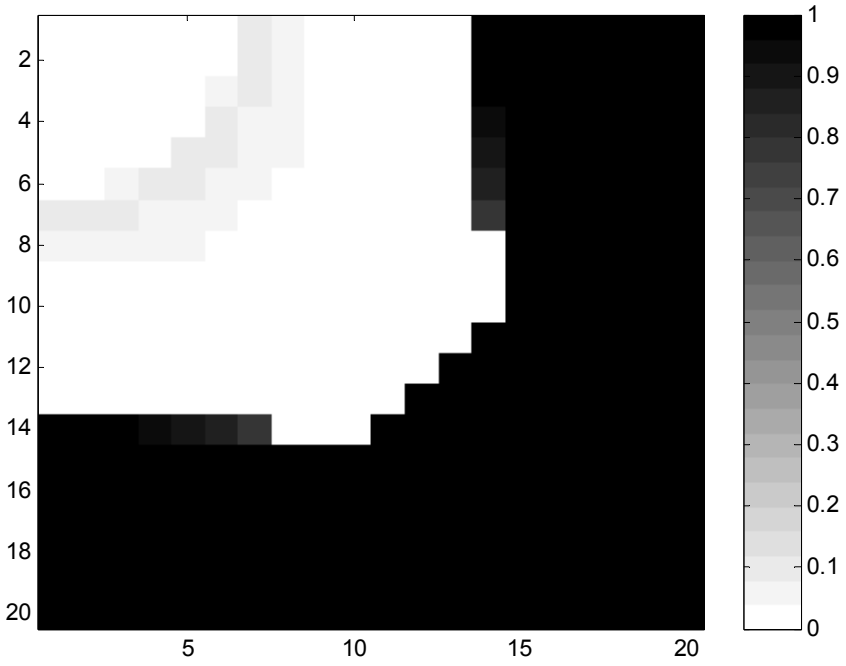

Fig. 55. Oil saturation from Strator at 0.33 PV of 50-50 injection of PBG and NGL into Shrader oil

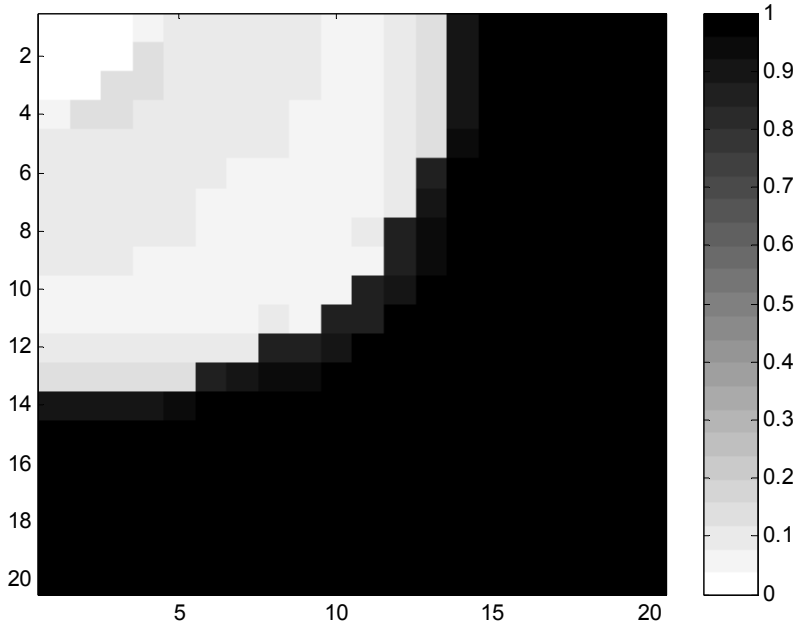

Fig. 56. Oil saturation from UTCOMP at 0.33 PV of 50-50 injection of PBG and NGL into Shrader oil.

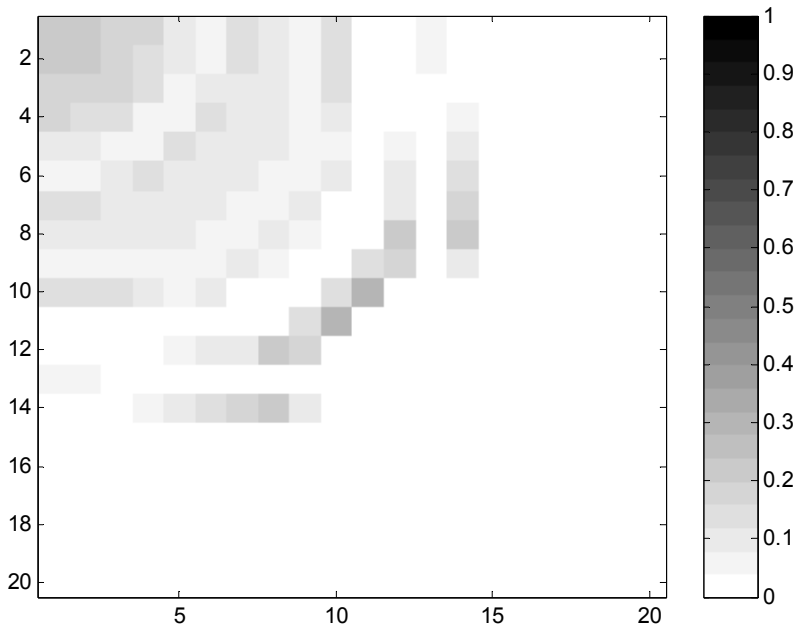

Fig. 57. Gas saturation from Strator at 0.33 PV of 50-50 injection of PBG and NGL into Shrader oil.

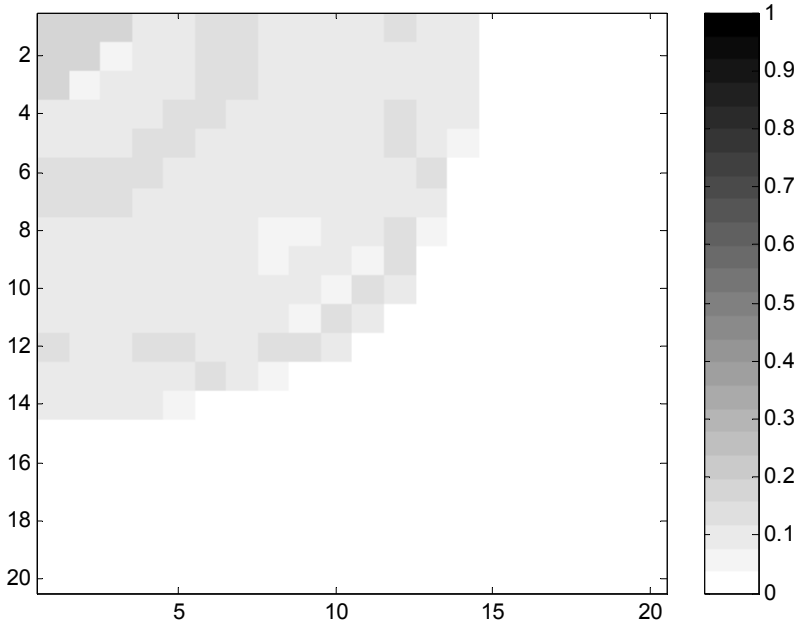

Fig. 58. Gas saturation from UTCOMP at 0.33 PV of 50-50 injection of PBG and NGL into Shrader oil.

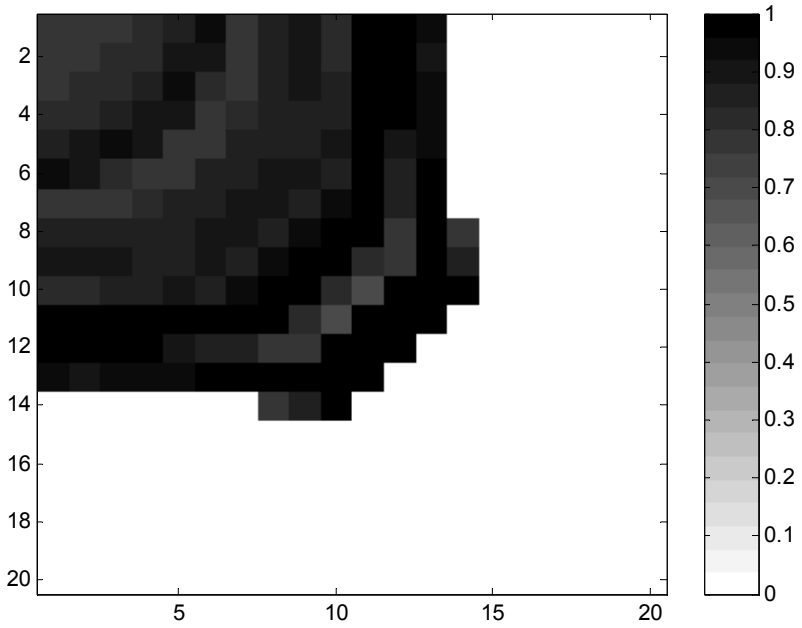

Fig. 59. Second non-aqueous liquid saturation from Strator at 0.33 PV of 50-50 injection of PBG and NGL into Shrader oil.

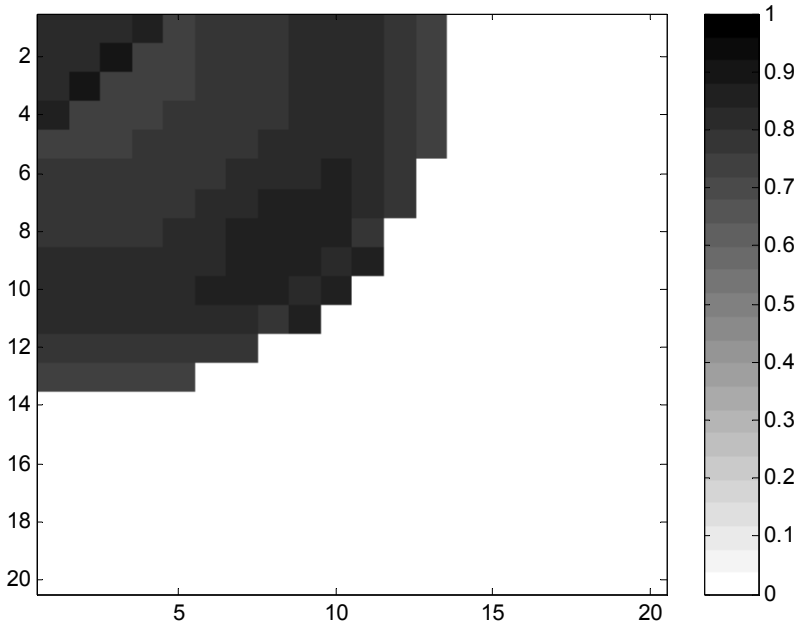

Fig. 60. Second non-aqueous liquid saturation from UTCOMP at 0.33 PV of 50-50 injection of PBG and NGL into Shrader oil.

WAG. Water-alternating-gas injection simulation has also been tested. A laboratory scale 5-spot initially at connate water saturation is considered. The injection gas is 85% CO2 and 15% NGL; its composition is listed in Table 15. Slug size of 0.05 PV and WAG ratio of 1 are used in the results shown.

Table 15. Composition of injection gas

	COMPOSITON
CO2	.85
COMPONENT	.006585
C4	.065055
C5	.038145
C6	.008985
C7-C10	.02382
C10- C13	.00741

Table 16. Flooding conditions

PAREMETER	VALUE
Initial Pressure	1067 psi
Pressure Drop	7 psi
Dimension	12* 12 * 1 (inches)
Porosity	.20
K	100 md
Initial water saturation	.2
Oil Viscosity	18 cp

Flooding conditions are listed in Table 16. The vertical injection well is at one corner of the quarter 5-spot and the vertical production well is at the diagonally opposite corner. In situ compositions and saturations at 0.17 PV total injection simulated in the streamline-based simulations are shown in Figs. 61-65. Two slugs of gas and one slug of water are already injected by this time. The second slug of water is being injected at 0.17 PV. The pressure is low in this example, thus only two hydrocarbon phases form. Fig. 61 shows the CO2 concentration distribution inside the 5-spot. The first slug of CO2 has dissolved inside the displaced oil to be visible, but the second slug is visible near the well bore. Fig. 62 shows the C14-C19 concentration distribution inside the 5-spot. This component is present in oil and not in the gas and represents the lighter part of the oil. This figure shows that these light oil components are being displaced by the WAG slugs in a stable manner.

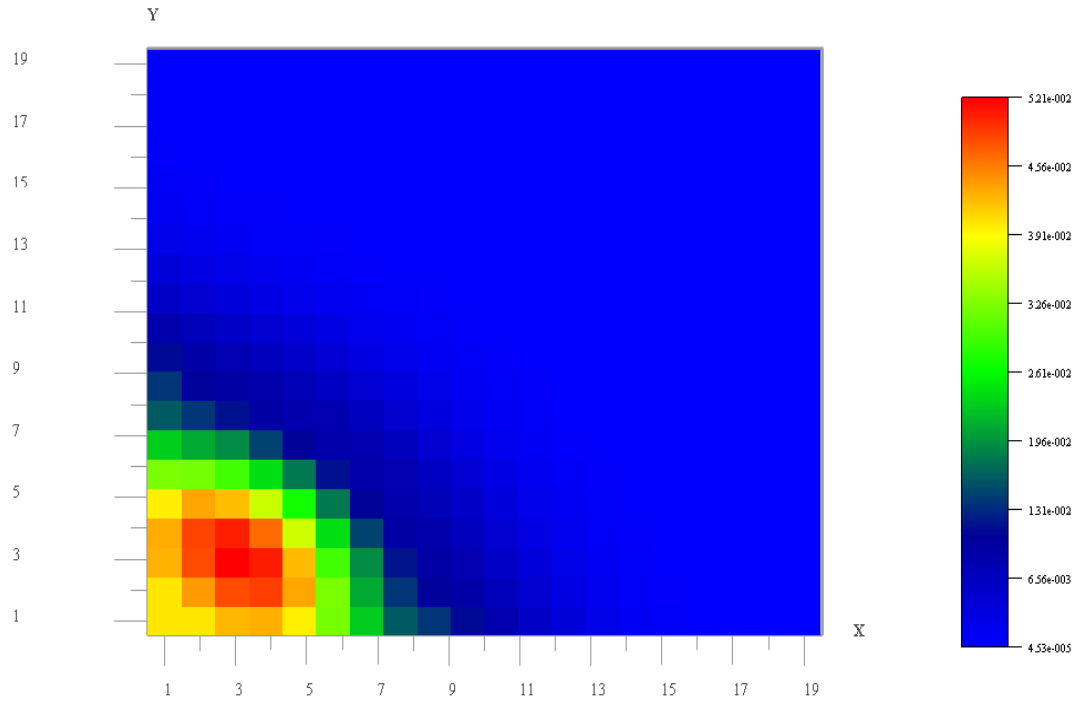

Fig. 61. CO2 concentration (moles/ft3) at 0.17 PV total WAG injection

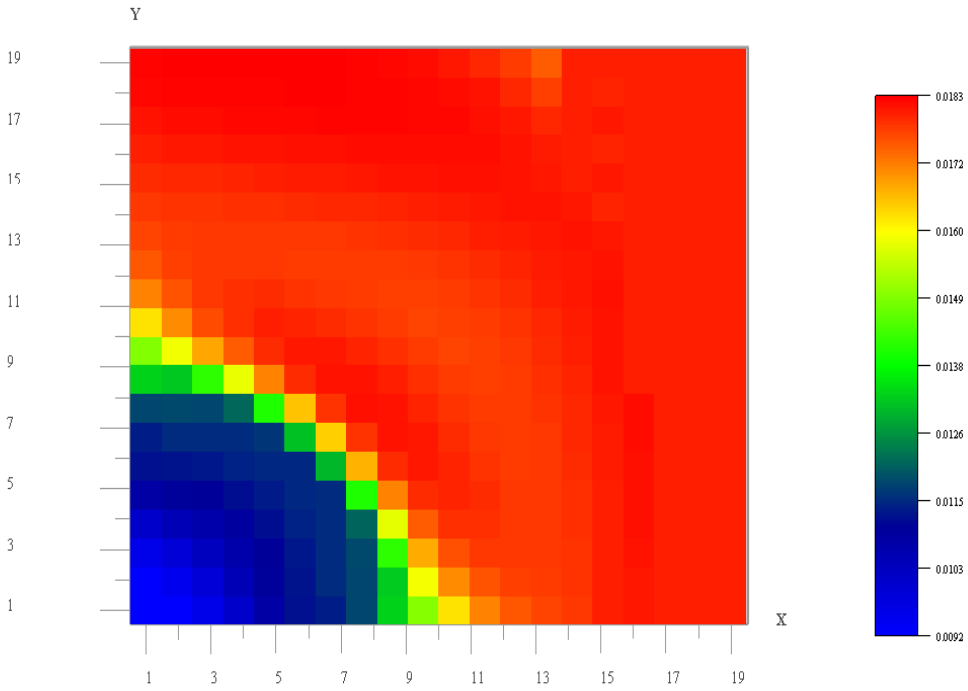

Fig. 62. C14-C19 concentration (moles/ft3) at 0.17 PV total WAG injection

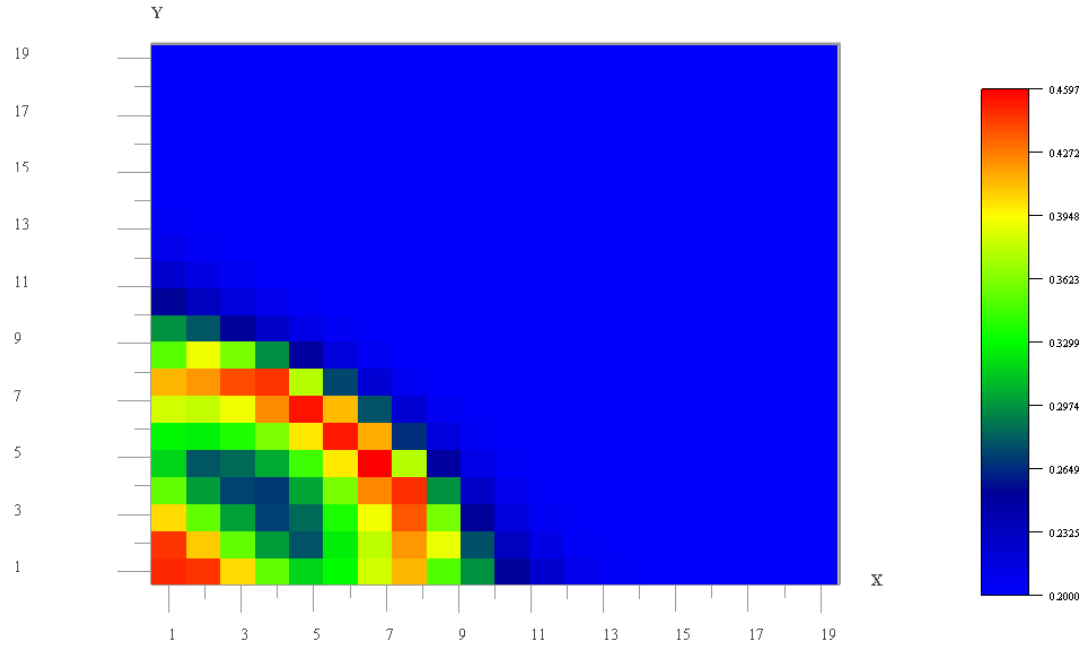

Fig. 63. Water saturation at 0.17 PV total WAG injection

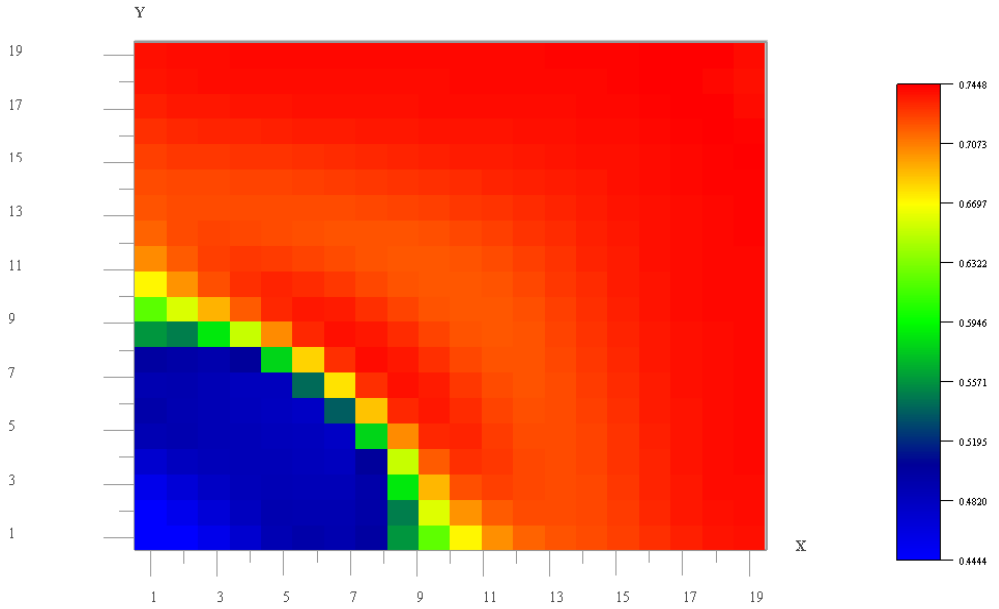

Fig. 64. Oil saturation at 0.17 PV total WAG injection

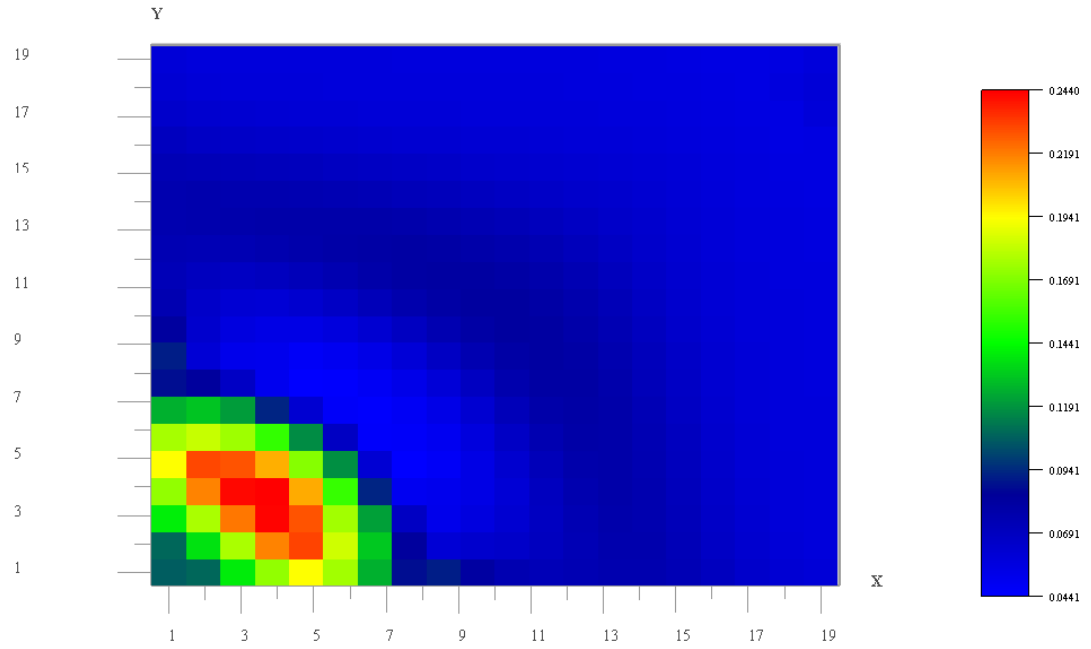

Fig. 65. Gas saturation at 0.17 PV total WAG injection

Fig. 63 shows the water saturation, which varies nonmonotonically along the diagonal due to alternate slugs of water and gas. Fig. 64 shows the oil saturation, oil is displaced very efficiently by this WAG process. Fig. 65 shows the gas saturation which also varies

nonmonotonically along the diagonal due to alternate slugs of water and gas. Such simulations has been conducted for different WAG ratios and slug sizes.

Well Architecture

Horizontal Production Well. Waterflood was simulated in a quarter 5-spot pattern. The parameters are listed in Table 17. The medium is assumed to be homogeneous and isotropic. The injector well was a vertical well in all cases. The producer well was either vertical or horizontal. The length of the horizontal well was varied from 50 to 600 ft. Fig. 66 shows the vertical injector well and the horizontal producer well combination.

Table 17 - Parameters for quarter 5-spot waterflood simulation

Initial Water Saturation	0.2
Initial Oil Saturation	0.2
Residual water Saturation	0.2
Residual Oil Saturation	0.3
Viscosity of Oil	52 cp
Number of Wells	2
Injector well	Vertical (Constant Bottomhole Pressure)
Producer Well	Vertical, Horizontal (Constant Bottomhole Pressure)
Number of Grid Blocks	40 * 40 * 5
Grid Size	15 ft * 15 ft * 15 ft
Porosity	0.352

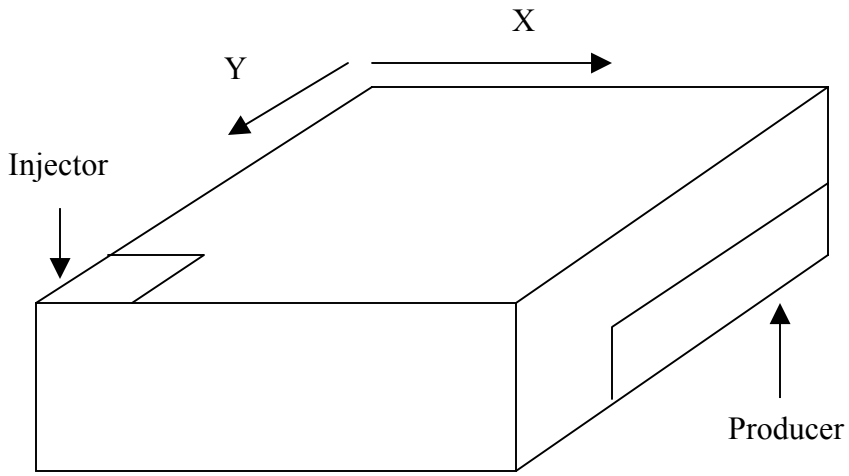

Fig. 66 - Waterflooding with a vertical injector and a horizontal producer

Fig. 67 shows the pressure distribution in the bottom most layer for different pore volumes of water injected for the vertical production well. Fig. 68 shows the same for the horizontal production well with a well length of 450 ft. The viscosity ratio is 3 for both the cases. The pressure contours are circular near the vertical wells. The pressure gradient near the production well is very high before breakthrough for the vertical well. For the horizontal well that pressure drop is lower because the flow enters the well through a bigger surface area. In these cases, the pressure drop in the horizontal well is small (~1 psi) compared to the well-to-well pressure drop (~1000 psi).

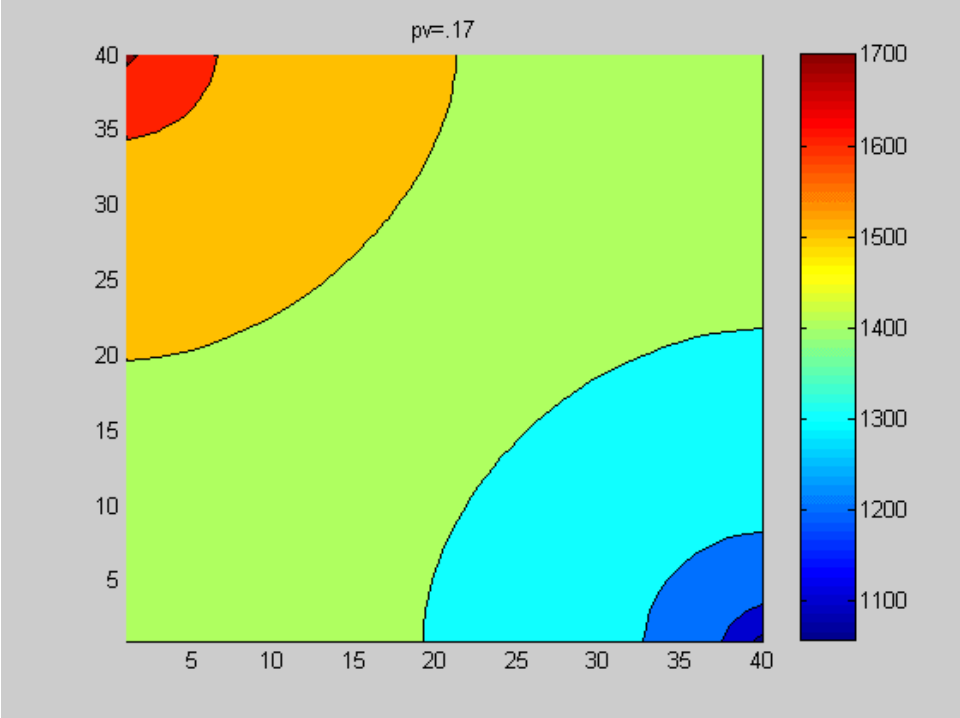

PVI = .17

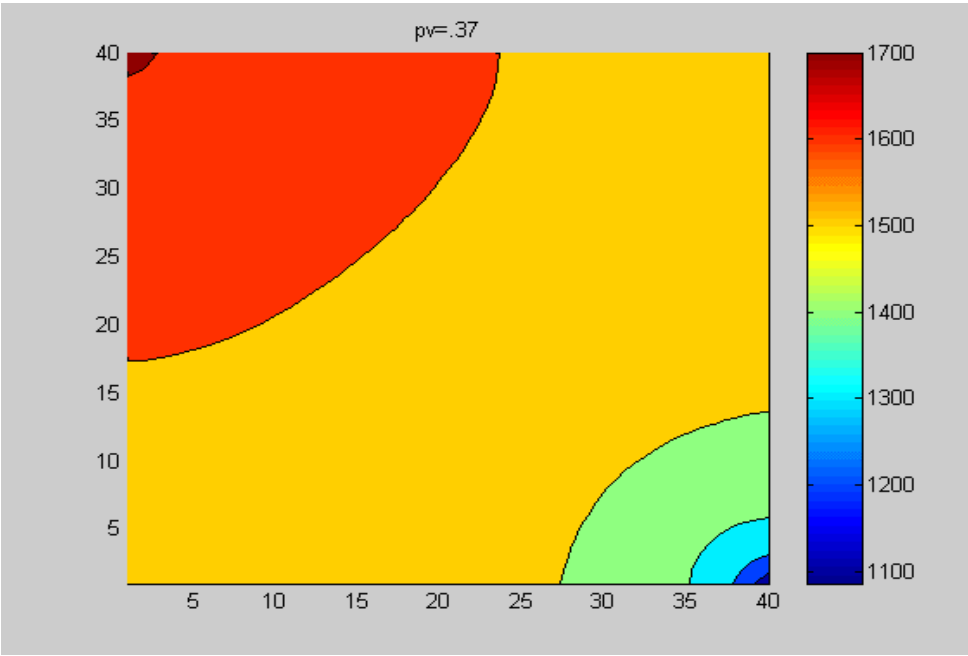

PVI =.37

Fig. 67 - Pressure profile in x-y plane for vertical injector and vertical producer

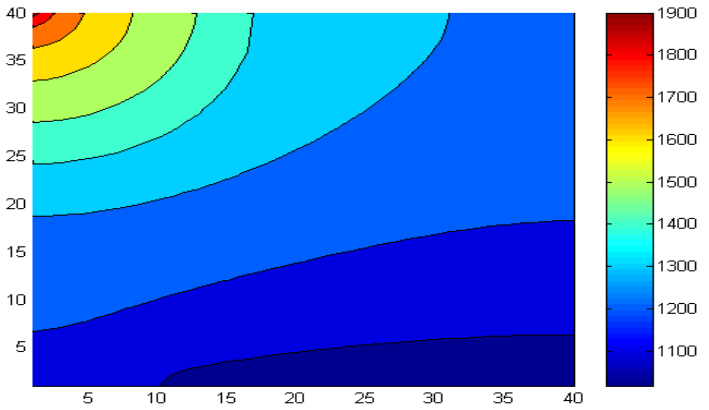

PVI = .05

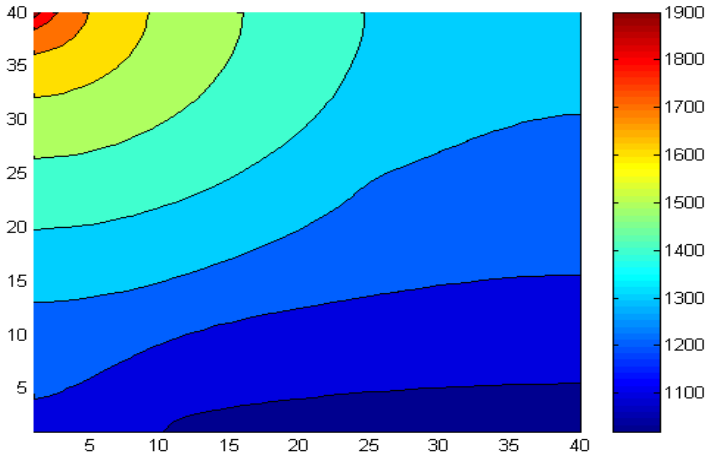

PVI =.17

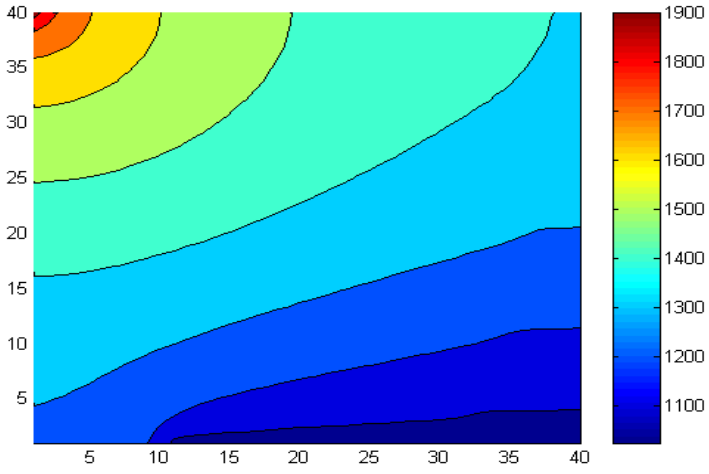

PVI = .45

Fig. 68 - Pressure profile in the bottom layer for the horizontal well producer

Saturations in the x-y plane for the bottom most layer is shown in Fig. 69 for different times for the vertical production well. The saturation distributions for the horizontal production well with a well length of 450 ft are shown in Fig. 70. It is observed that the contours of constant saturation are very different for the horizontal well from those with the vertical production well. Streamlines tend to bend towards the horizontal well located in the bottom most layer, which leads to earlier breakthrough. Saturations are also plotted in Fig. 71 for vertical x-z plane at y = L/8, where L is the length of the side of the quarter 5-spot. Water slumping is minimal in this example.

Mobility ratio is defined as the mobility of water at the average saturation behind the shock to the mobility of oil, which is inversely proportional to their viscosity ratio. Viscosity ratio was varied from 1 to 100. Water mobility is calculated at the average saturation in the water-contacted portion of the reservoir. Volumetric sweep efficiency at the breakthrough for different mobility ratios is plotted in Fig. 72 for both a horizontal (with a well length of 300 ft) and a vertical production well. As expected, the sweep efficiency decreases the mobility ratio increases. However, the sweep efficiency is lower for the horizontal well. Thus, the increase in production rate (with the horizontal well) comes with a price of decreased breakthrough sweep efficiency.

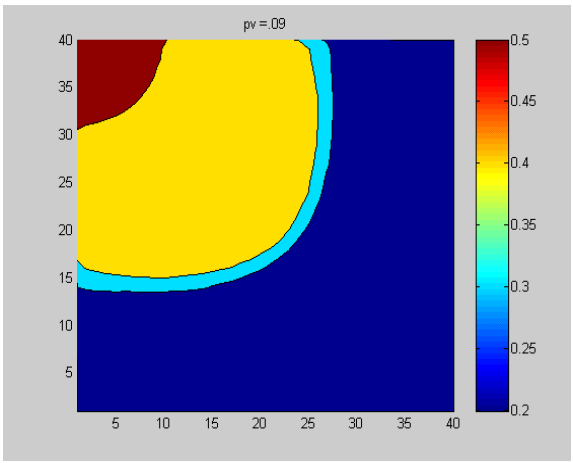

PVI= .09

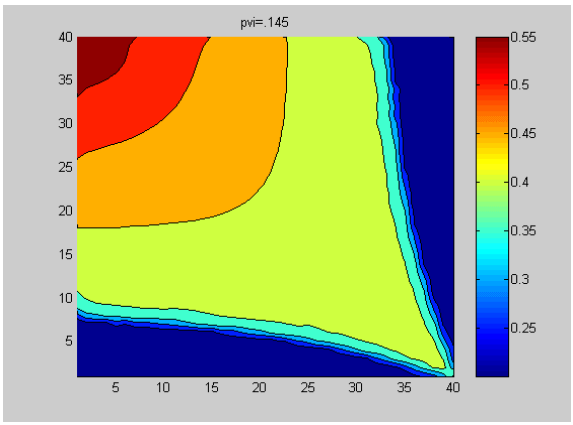

PVI= .145

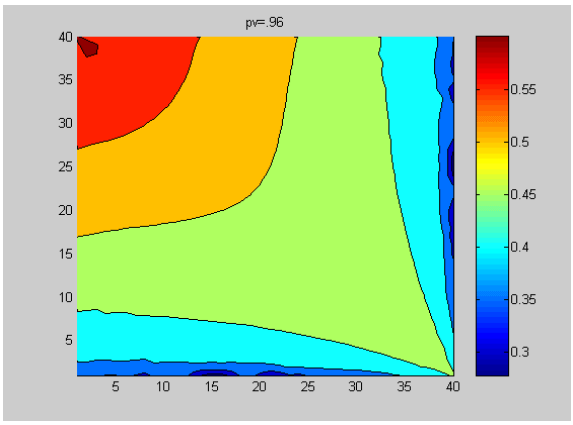

PVI = .35

Fig. 69 - Saturation profile in the bottom layer with a vertical producer

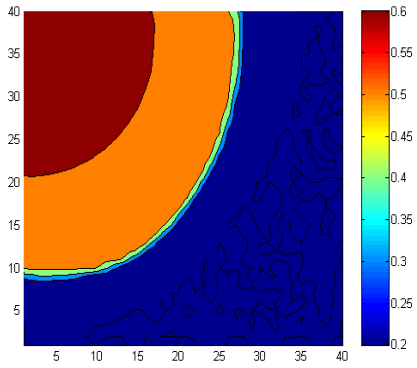

PVI = .17

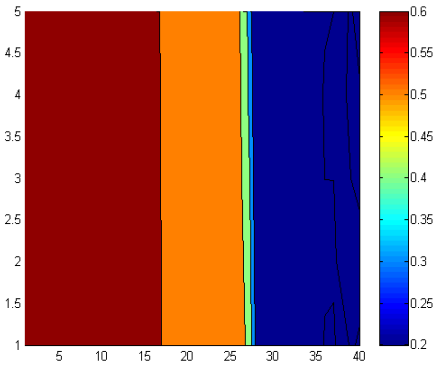

PVI= .17

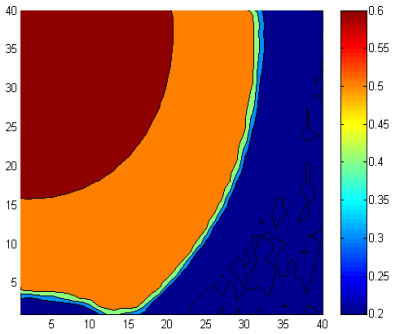

PVI =.25

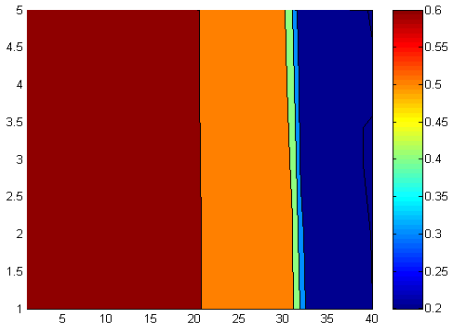

PVI= .25

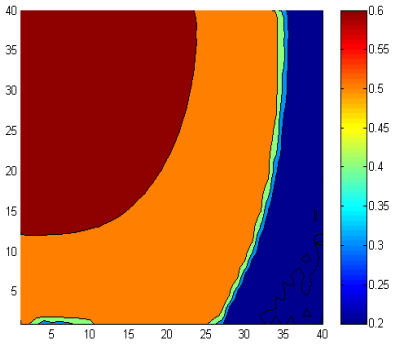

PVI= .34

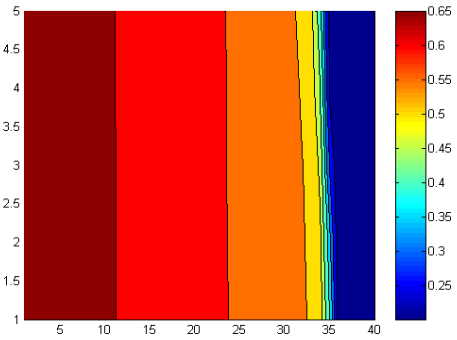

PVI= .34

Fig. 70 - Saturation profile in the bottom layer for horizontal producer

Fig. 71 - Saturation profile in a vertical section at y=L/8, horizontal producer

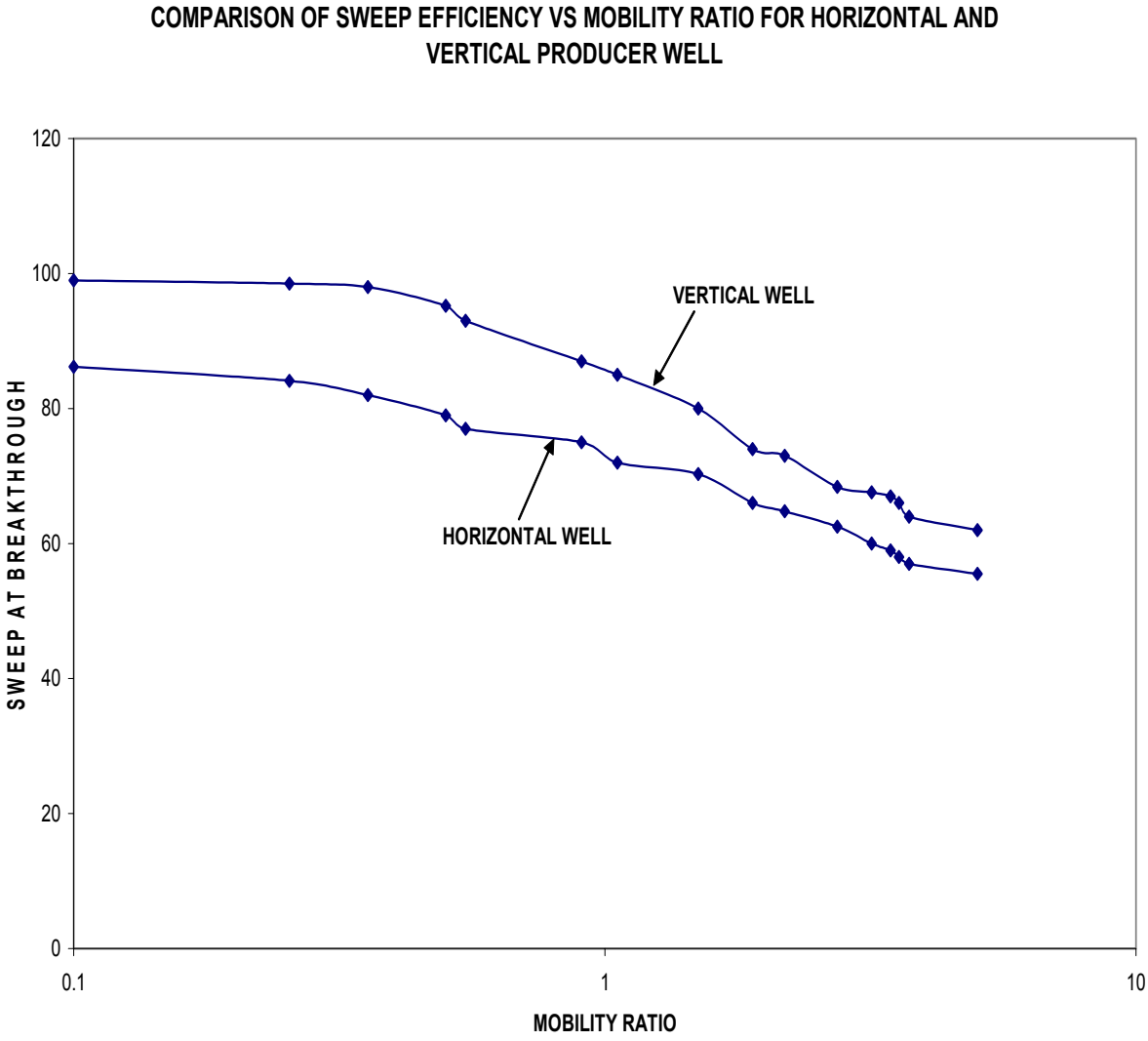

Fig. 72 - Comparison of sweep efficiency between horizontal and vertical producer wells

The oil production rates in the quarter 5-spot with the horizontal and the vertical production wells are compared in Fig. 73. The horizontal well has a higher initial oil flow rate than the vertical well. But after breakthrough, oil flow rate drops in the horizontal case. The breakthrough is later for the vertical production well. Therefore, oil flow rate is higher between 200 and 400 days for the vertical well. After breakthrough, the oil production rate in the vertical well falls below that of the horizontal well.

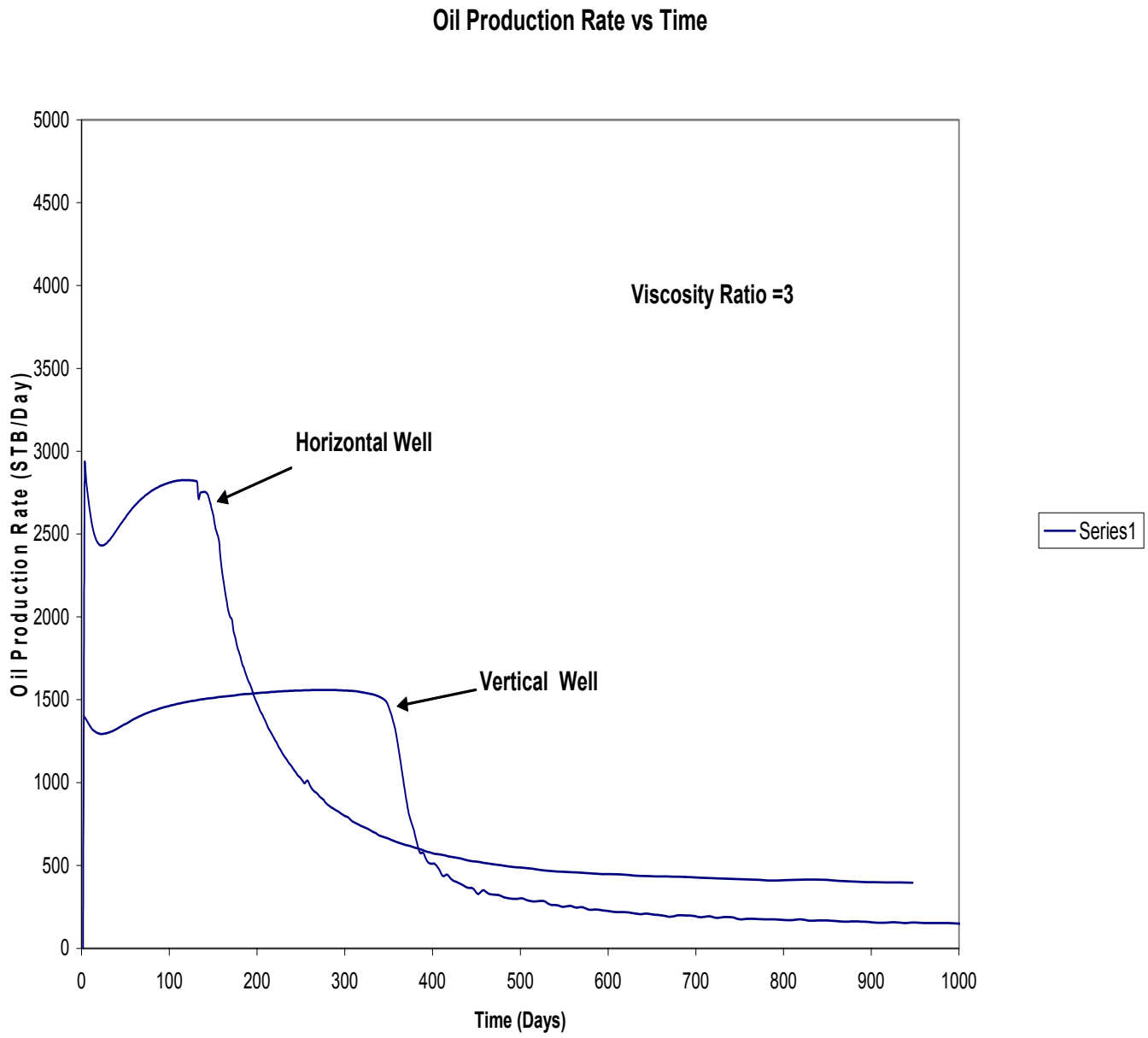

Fig. 73 – Comparison of oil production rate between horizontal and vertical producer wells

The influence of the well length on breakthrough sweep efficiency is shown in Fig. 74. As the length of the horizontal well is increased keeping everything else constant, volumetric sweep decreases. As the length of the well is increased, streamlines tend to go towards the toe of

the well thereby covering less volume of the reservoir. Again production rate increases at the expense of sweep efficiency.

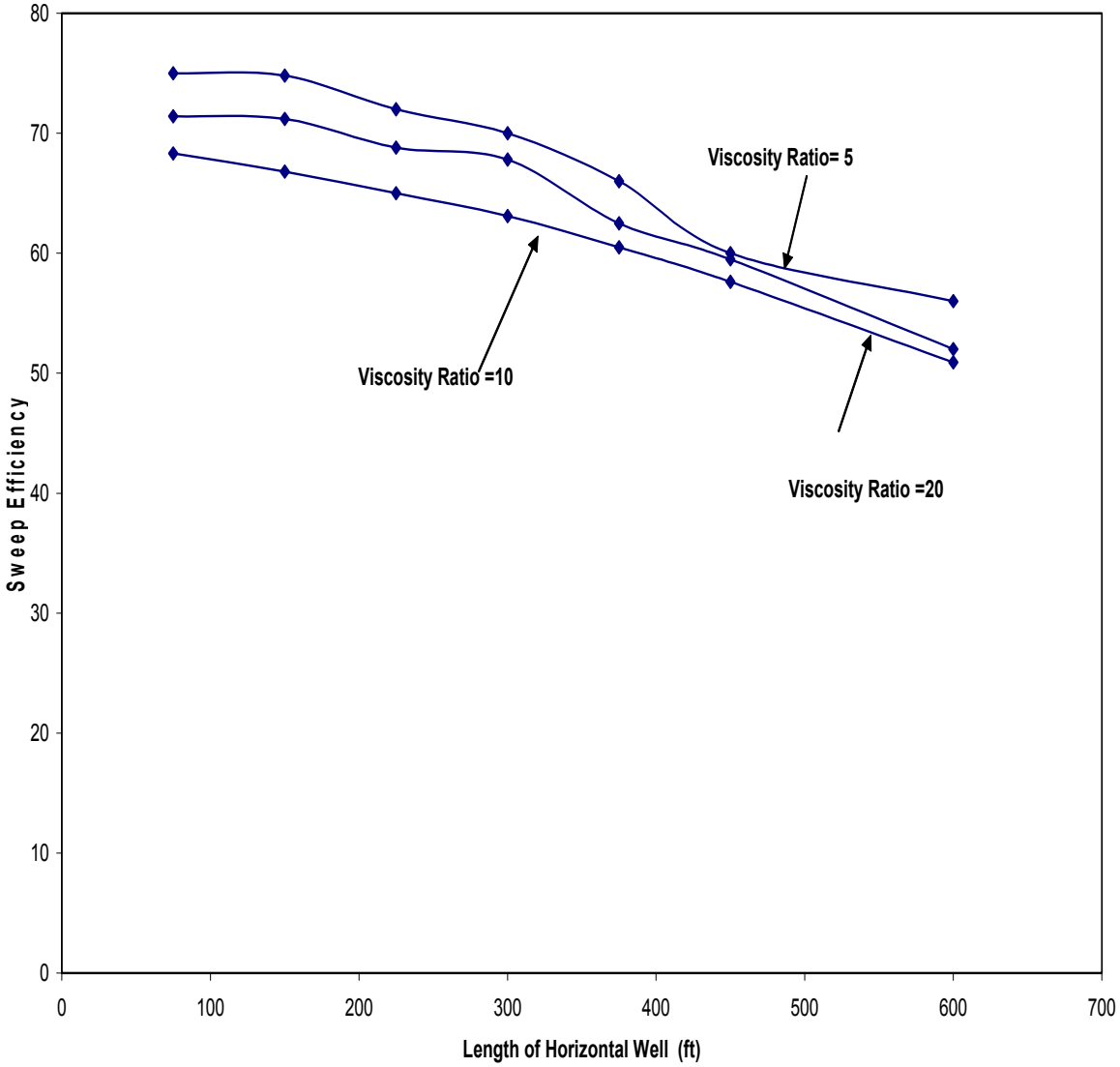

Fig. 74 - Sweep efficiency at the breakthrough for different lengths of horizontal well

Electromagnetic Heating. Electromagnetic heating is simulated in vertical wells. The parameters are listed in Table 18. The following viscosity (kg/m.sec) - temperature (K) correlation is used:

$$\mu = A \exp(3936.6/T). \quad (39)$$

The parameter A is adjusted to get the desired initial viscosity. In the cases considered, the heating extended to less than 10 m. Thus the governing equations are solved for the domain $0.15 \text{ m} < r < 15 \text{ m}$.

Power density, P_0	200-1000 W/m^3
Thermal conductivity of oil, k	1.56 W/m-K
Density of oil, ρ	999.648 kg/m^3
Specific heat of oil, C_P	1812.88 J/kg-K
Permeability, K	500 mDa
Density of rock, ρ_r	2162.5 kg/m^3
Specific heat of rock, C_{pr}	795.5 J/kg-K
Thermal conductivity of rock, k	2.25 W/m-K
Thickness of oil zone, H	13 m
Ambient Temperature, T_a	288 K
Absorption index, n_i	0.09
Wave-length of EM waves, λ	1 m
Heat transfer coefficient, h	100 W/m^2-K

Table 18 – Parameters for electromagnetic heating

Fig. 75 shows the temperature profile within the reservoir as a function of radial distance from the center of the well bore for a heating power level of 200 W/m^3 and a flow rate of about 44 b/d (vr = 10^{-6} m^2/s). The temperature at the well bore is about 301 K, 13 K above the ambient reservoir temperature. Temperature falls away from the well; temperature increase is negligible beyond about 6 m. This temperature profile is independent of the original viscosity of the oil as long as the flow rate is kept constant and Eq. 39 is valid for oil viscosity.

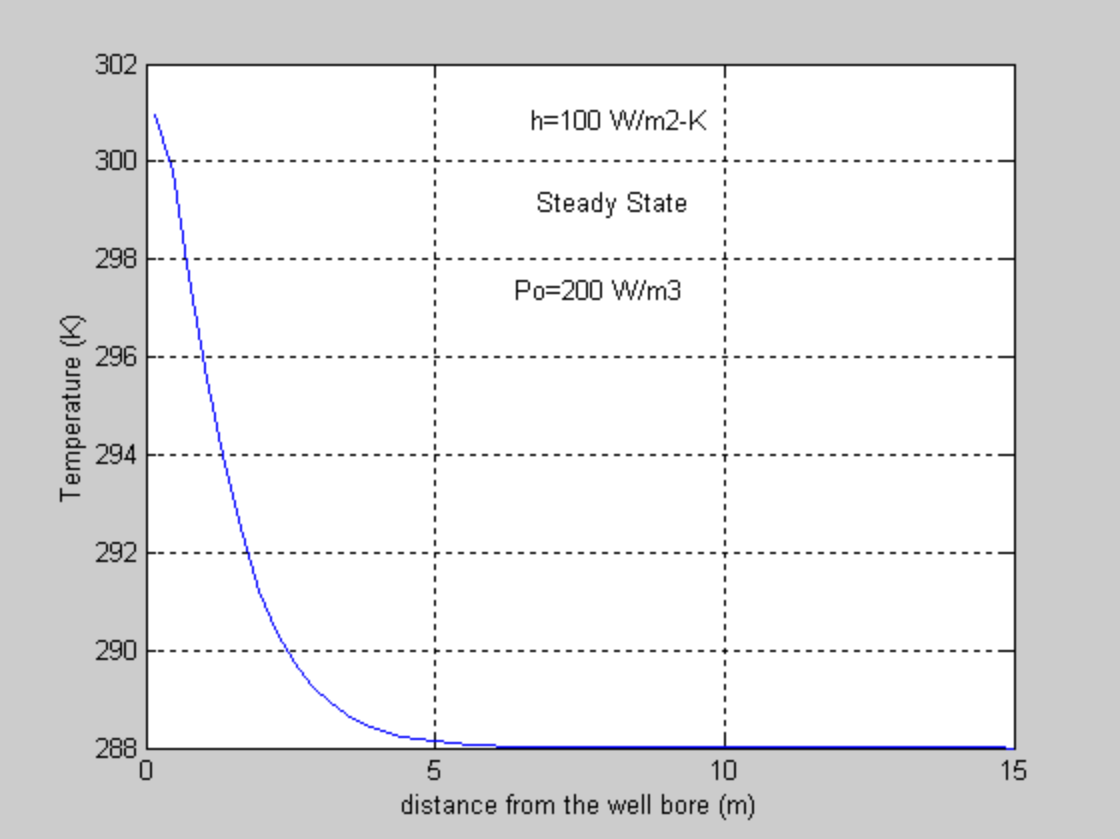

Fig. 75 - Temperature profile for low power-density parameter, Po = 200 W/m^3.

Fig. 76 shows the temperature profile for a higher power level, 950 W/m^3. The well bore temperature is 350 K, much higher than the lower power case, but the heated distance is about the same, ~6 m from the well bore. This distance is controlled by the frequency of the electromagnetic waves and the flow rate, but not by the power level. The increase in the well bore temperature with the power level is shown in Fig. 77 for constant flow rate. As expected, the well bore temperature increases almost linearly with the power level.

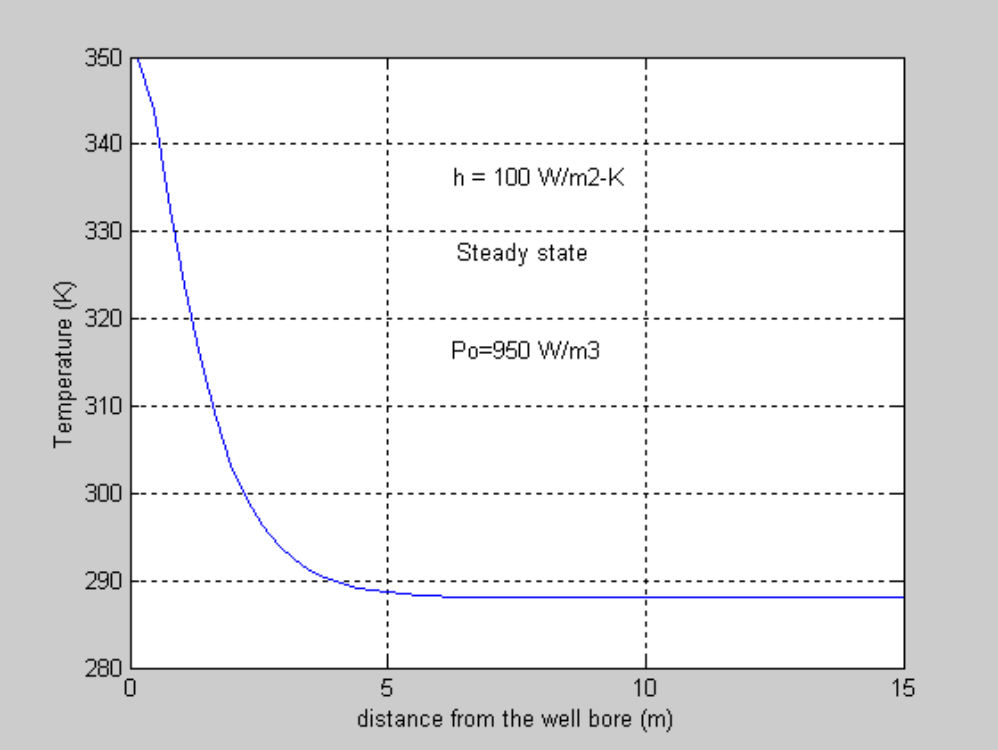

Fig. 76 - Temperature profile for high power-density parameter, Po = 950 W/m^3.

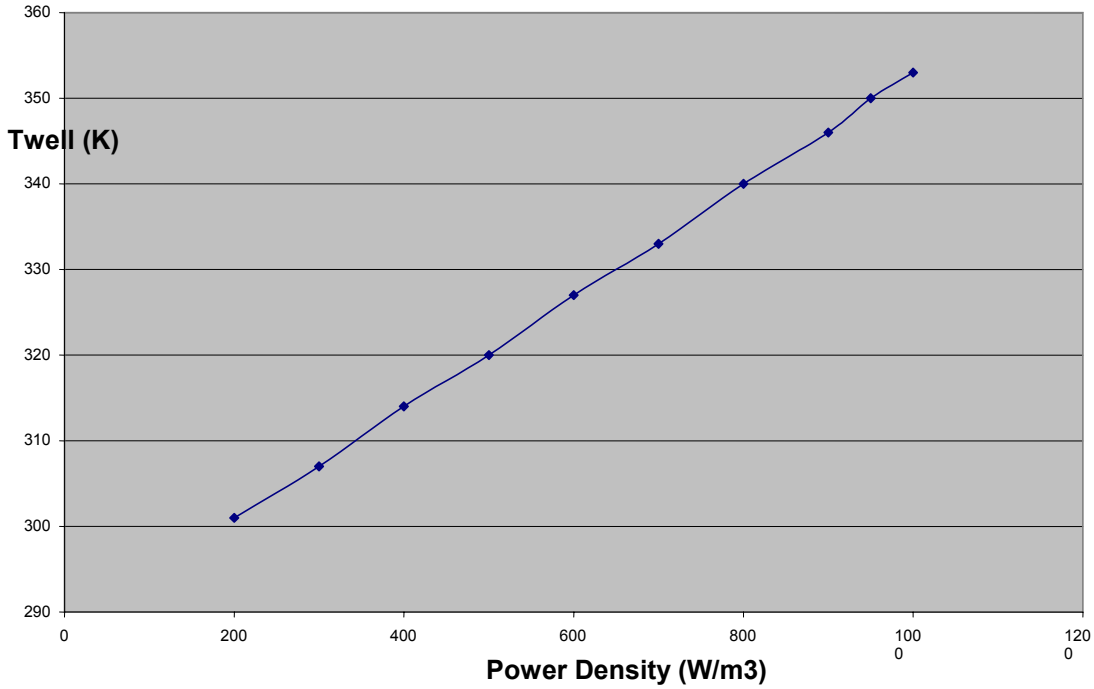

Fig. 77 - Well bore temperature (K) vs. power density (W/m^3) at 44 b/d flow rate.

Fig. 78 shows pressure drop in the first 15 m from the well-bore as a function of electromagnetic heating power density for three different initial oil viscosities for a constant well flow rate (44 b/d). As the power input increases, pressure drop falls because the oil viscosity decreases. For a power input of 1000 W/m3, the pressure drop is about the half of the pressure drop with no heating. Thus the productivity increase is a factor of 2 for a power input of 1000 W/m3. This productivity increase is independent of the original viscosity for a constant flow rate (assuming Eq. 39).

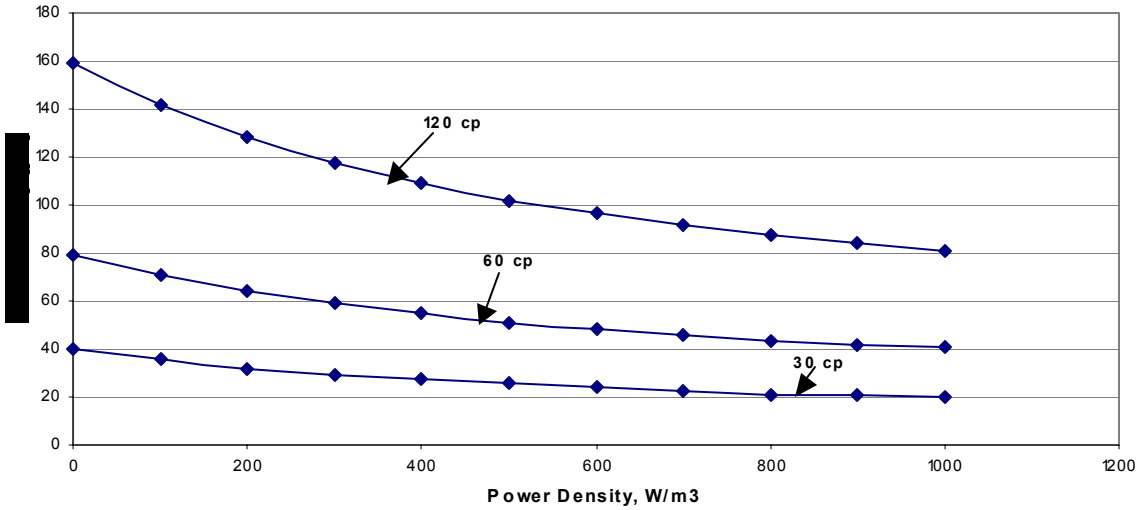

Fig. 78. Pressure drop around the well bore as a function of power input for 44 b/d flow rate for three different initial oil viscosities.

Waterflood was simulated in a quarter 5-spot pattern with vertical wells with or without heating at the production wells. The parameters are listed in Table 19. The medium is assumed to be homogeneous and isotropic. Fig. 79 shows the oil production rate in the five spot with and without electromagnetic heating. Heating increases the oil flow rate before breakthrough by about 10%. The water breakthrough is thus earlier by about 10%.

Initial Water Saturation	0.2
Initial Oil Saturation	0.2
Residual water Saturation	0.2
Residual Oil Saturation	0.3
Viscosity of Oil	52 cp
Number of Wells	2
Injector well	Vertical (Constant Bottomhole Pressure)
Producer Well	Vertical (Constant Bottomhole Pressure)
Number of Grid Blocks	40 * 40 * 5
Grid Size	15 ft * 15 ft * 15 ft
Porosity	0.352

Table 19 - Parameters for quarter 5-spot waterflood simulation

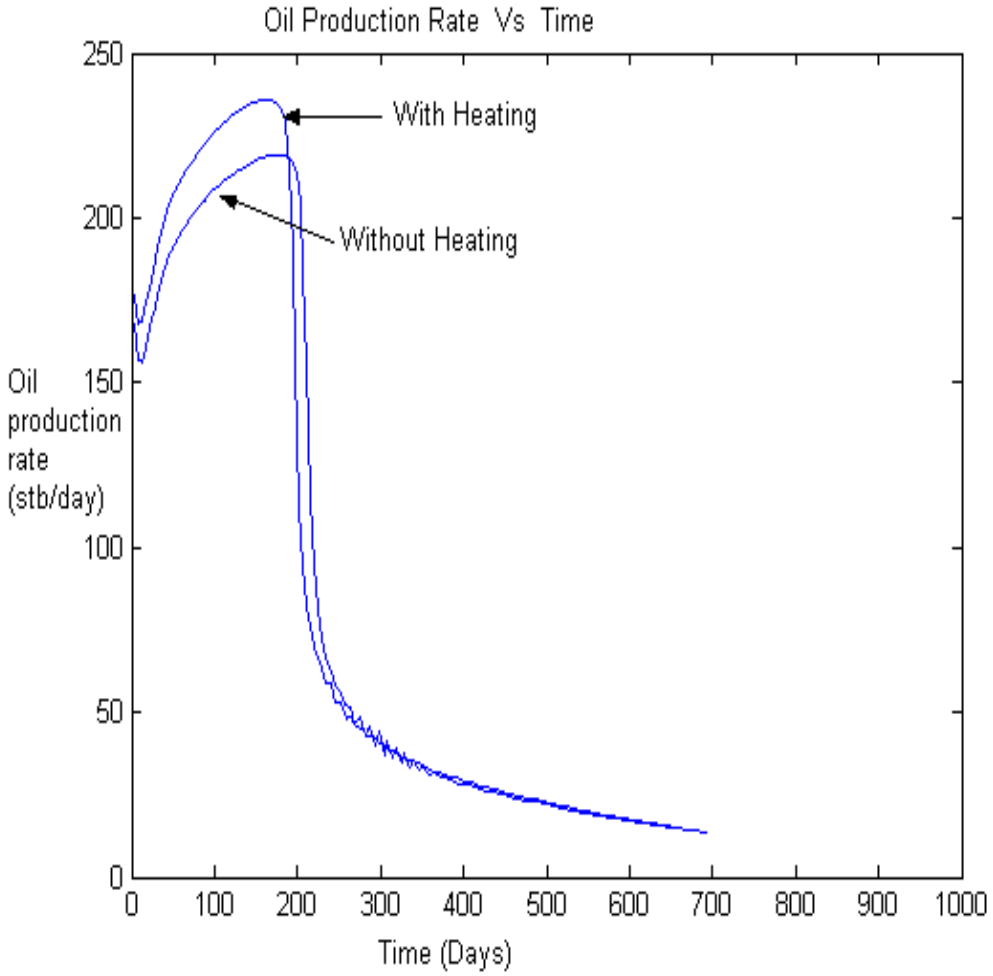

Fig. 79 - Oil production rate in the production well of a five spot; viscosity of oil = 52 cp.

WAG Optimization

The Berea core was flooded with live oil at steady flow of 0.15 mL/min. Then gas solvent was injected into the core at the same rate as soon as the live oil source was shut off. 0.6 PV of gas was injected followed by water. The composition of the injection gas is listed in Table 2; it is 50:50 mixture of NGL and PBG. This gas is multicontact miscible at the core pressure according to the slimtube studies. The pressure drop across the core as the function of gas injection is shown in Fig. 80. Pressure drop decreases sharply as the gas breaks through the core. The final pressure drop is very small indicating that there is no injectivity problem associated with the second hydrocarbon liquid phase.

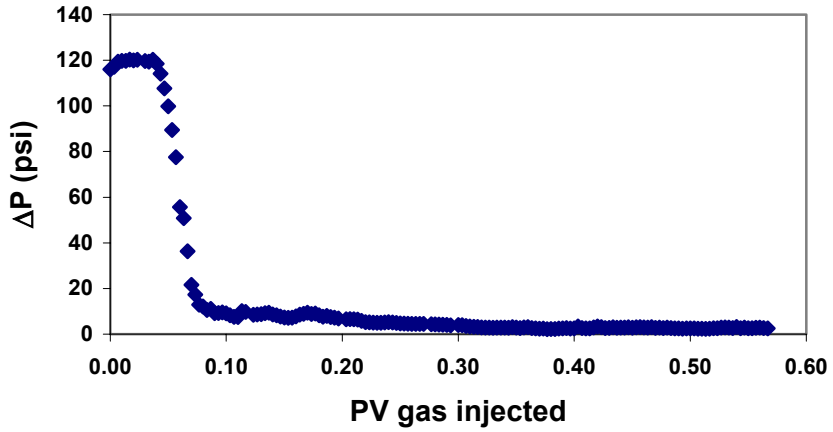

Fig. 80 – Pressure drop vs. PV gas injection

The cumulative oil production as a function of gas injection is shown in Fig. 81. Oil production rate is initially about constant indicating efficient displacement of oil by this miscible injectant. It falls after about 0.25 PV injection of solvent indicating breakthrough of solvent. The cumulative production of oil at the end of solvent injection is about 45% of the original oil. Water injection was continued for another 1.4 PV and the final recovery was about 67% OOIP.

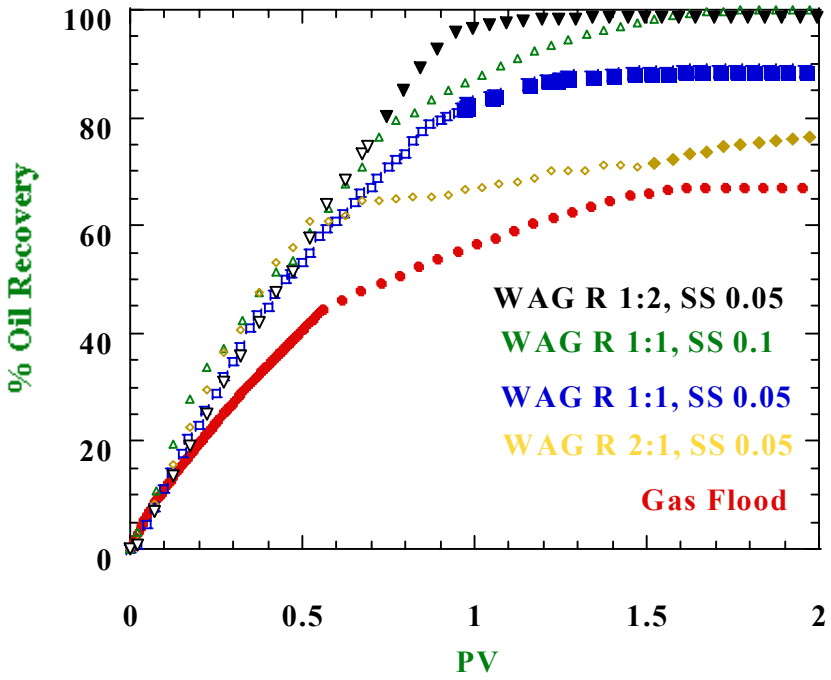

Fig. 81 – Cumulative oil production vs. PV gas injection

In 1D displacement (slimtube) of oil by this multicontact solvent, the recovery is often greater than 95%. The existence of a residual saturation of 33% in the coreflood implies bypassing in the core leading to immiscibility and residual oil trapping. Miscible flood in a core is not totally stable because of adverse mobility ratio. This adverse mobility and core-scale heterogeneity lead to bypassing. Water-alternating-gas slugs were injected in the following experiments to minimize bypassing.

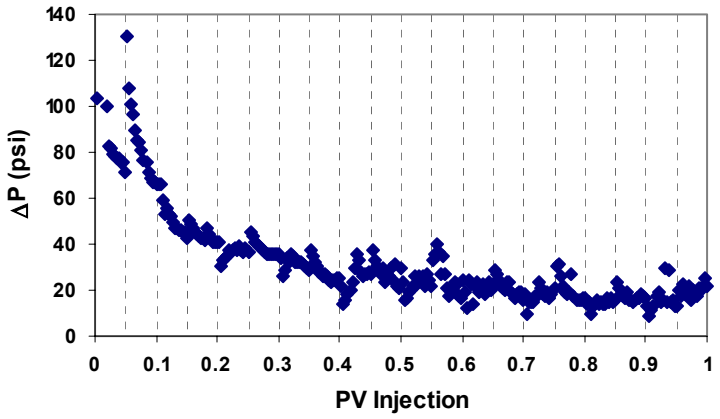

Fig. 82 – Pressure drop vs. cumulative injection for WAG flood.

The WAG ratio of 1:1 with the slug size of 0.05 PV was used in this experiment. About 0.5 PV of total solvent was injected. About 0.5 PV of brine was injected alternating with the gas slugs followed by another 1 PV of water. The pressure drop versus cumulative injection is shown in Fig. 82. Every time a gas slug is injected, the pressure drop decreases because gas is less viscous than oil or water. Every time a brine slug is injected, the pressure drop first increases and then decreases because of relative permeability effects.

The cumulative oil production is shown in Fig. 81. The oil production rate is about constant until about 0.35 PV injection. The oil production rate falls after 0.35 PV injection, but not as much as in the gas flood. Water is also produced before 0.35 PV injection, but the production rate increases after 0.35 PV injection. With the WAG flood ratio 1:1, about 80% of oil was recovered by the end of the end of WAG injection (i.e., 1 PV). By the end of the follow-up water injection (2 PV total injection), the oil recovery was 88%. This experiment shows that WAG injection stabilizes the displacement at the core-scale and gives recovery similar to 1D slimtube floods.

WAG ratio 1: 1 with the slug size of 0.1 PV was used in the next experiment. After 0.1 of pore volume gas injection, we switched to inject 0.1 pore volume of brine at the same rate. The procedure was repeated with gas and brine injection until a total 0.5 pore volume of gas was injected into the core. Additional brine injection was made up for a total of 2 pore volume of gas and brine injections. The pressure drop versus pore volume injection is shown in Fig. 83. The oil recovery is almost 100% OOIP.

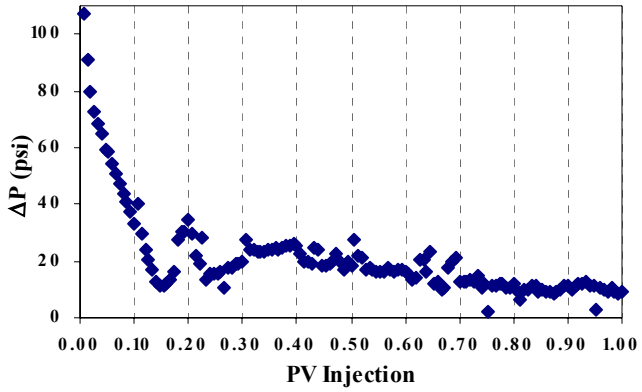

Fig. 83 – Pressure drop vs. PV gas injection for WAG ratio 1:1, slug size 0.1 PV

WAG ratio 2:1 with the slug size of 0.05 pore volume was used in the following experiment. Fig. 84 shows the pressure drop versus pore volume injection for the WAG flood with ratio 2 to 1. The experiment started with 0.05 PV of gas injection followed by 0.1 PV of brine. The total of 0.5 PV of gas mixture was injected into the core in this experiment. Pressure drop for the last water injection and additional water flooding is not shown in this plot. The oil recovery is about 77% OOIP.

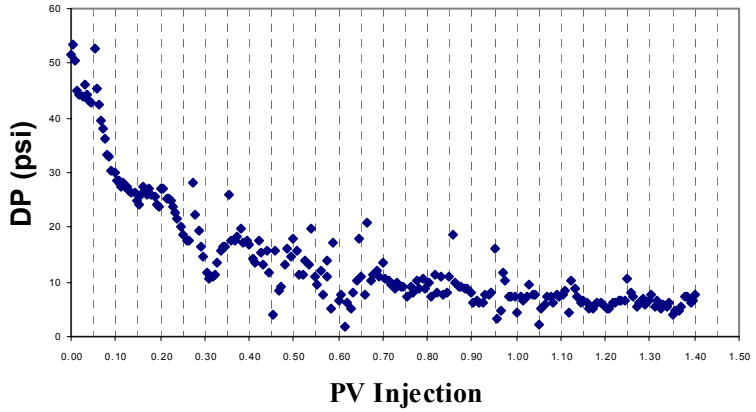

Fig. 84 – Pressure drop vs. PV gas injection for WAG ratio 2:1, slug size 0.05 PV

An additional linear WAG floods with slug size of 0.05 PV and WAG ratio 1:2 was conducted. After 0.1 of pore volume gas injection, we switched to inject 0.05 pore volume of brine at the same rate. The procedure was repeated with gas and brine injection until a total 0.5 pore volume of gas was injected into the core. Additional brine injection was made up for a total of 2 pore volume of gas and brine injections. The pressure drop versus pore volume injection is shown in Fig. 85. The oil recovery is about 100% in this WAG flood.

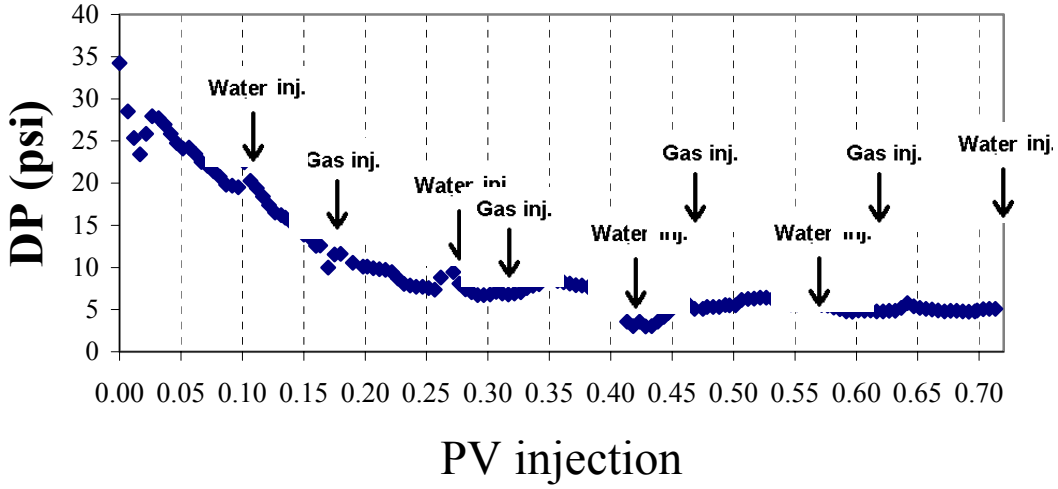

Fig. 85 – Pressure drop for WAG ratio 1:2, slug size 0.05 PV

Fig. 81 shows the comparison in percentage oil recovery for gas flood with different WAG ratio as a function of pore volume injection. As the WAG ratio increases, the oil recovery decreases, but it is the lowest for the gasflood. Thus the optimum WAG ratio for the core is about 0.5. The oil recovery increases with the slug size for constant WAG ratio.

Gas flood in the laboratory 5-spot cell. The residue water saturation was determined to be 9 % in this cell. The injection flow rate was 22.5 mL/hr for oil, solvent and water. The back pressure regulator pressure was set at 1700 psi. Fig. 86 shows the pressure drop between the inlet and the outlet of the sand-pack cell as a function of PV injection. Only the pressure drop for 0.5 PV of solvent injection is shown. Fig. 87 shows the oil recovery as a function of solvent and water injection. About 83 % of oil was recovered after 0.5 PV of solvent and additional two PV of water injection.

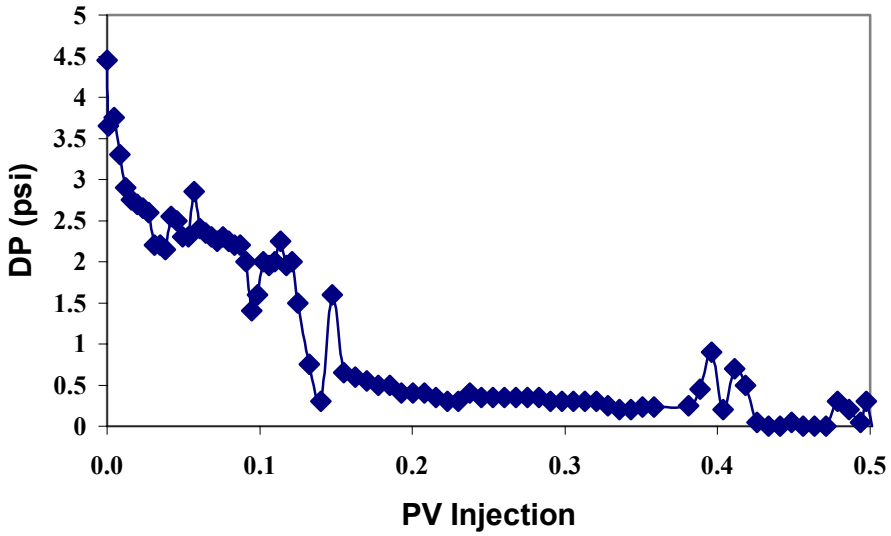

Fig. 86 – Pressure drop vs. PV injection in the quarter 5-spot model

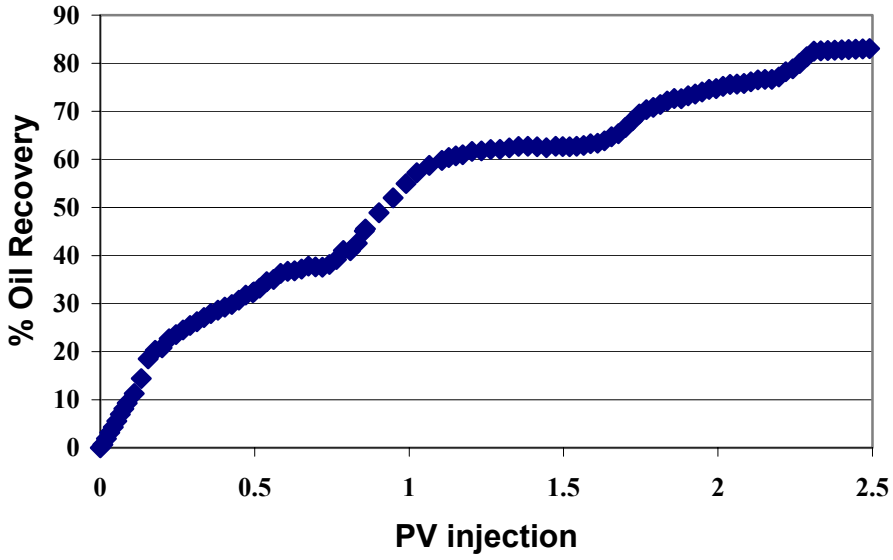

Fig. 87 – Percentage oil recovery vs. PV injection in the quarter 5-spot model

Field Case Simulations. 1D simulations of solvent flooding suggest that two mixtures (85% CO2-15% NGL and 60% PBG-40% NGL) reach miscibility with Schrader viscous oil in situ. WAG simulations were conducted with the mixture of 85% CO2-15% NGL as the solvent. For field cases, effects of both WAG ratios and slug sizes on oil recovery were investigated. WAG was performed on a reservoir by using a 20-acre five-spot pattern. Due to symmetry, only one quarter of the pattern was studied in the simulations. A 20 × 20× 1 grid was used in the simulations. Thus, gravitational effects are totally neglected.

Homogeneous Cases. Conditions of the field WAG cases are listed in Table 20, which shows the reservoir is homogeneous with a permeability of 250 md.

Table 20 - Conditions for the Field WAG Cases		
Parameter	Value	Unit
$X_{1/4}$	466.6905	ft
$Y_{1/4}$	466.6905	ft
Z	1	ft
S_{wi}	0.4	unitless
K_x	250	md
K_y	250	md
K_z	250	md
T	86	^{o}F
P_i	1750	psi
ϕ	0.352	unitless
P_{inj}	1800	psi
P_{pro}	900	psi

First, the effect of WAG ratio was investigated. While slug size was set as a constant (0.05 PV), four WAG ratios were used: 0.5, 1, 2, and 4. The total amount of solvent injected was kept at 0.5 PV in these simulations. Water, oil, gas, and the second non-aqueous liquid saturations at 0.5 PVI for the WAG ratio of 0.5 are shown in Fig. 88, which indicates the gas phase exists only in several grid blocks on the flanks of the displacement front, similar to what was observed from slim tube simulations. The second liquid phase is present in most of the swept grid blocks. Injection of water increases the sweep of the second phase liquid, but it still breaks though the production well fairly early. Oil saturation profile at 0.5 PVI for the WAG ratio of 4 is shown in Fig. 89. It can be compared with that of Fig. 88 (b). As WAG ratio increases, solvent breakthrough is delayed in terms of cumulative (total) injection. Oil recovery is shown in Fig. 90, which indicates that oil recovery is faster with decreased WAG ratio. More solvent is injected for a lower WAG ratio than for a higher WAG ratio at any given time because of the WAG schedule and lower resistance to flow. Miscible solvent is more effective than water

in recovering oil. The ultimate recovery at 0.5 PV injection of solvent is very similar. Economical analysis can be conducted to find the optimum WAG ratio.

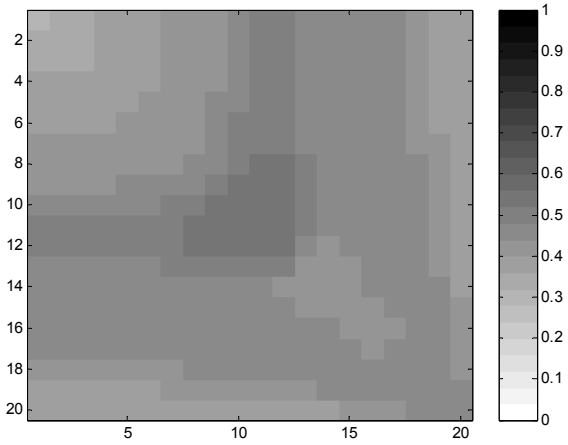

a) Water.

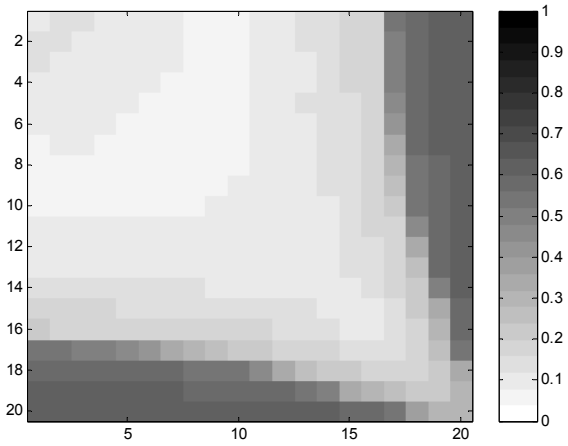

b) Oil.

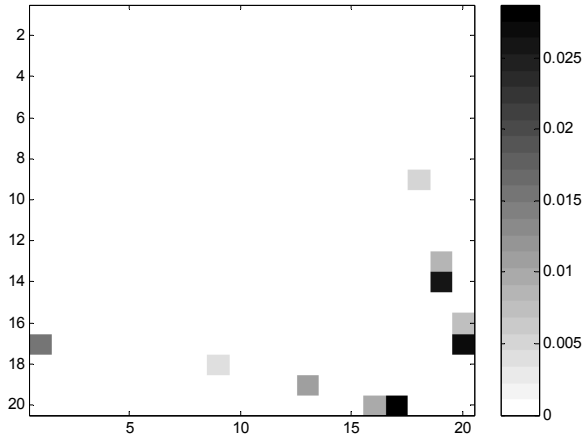

c) Gas.

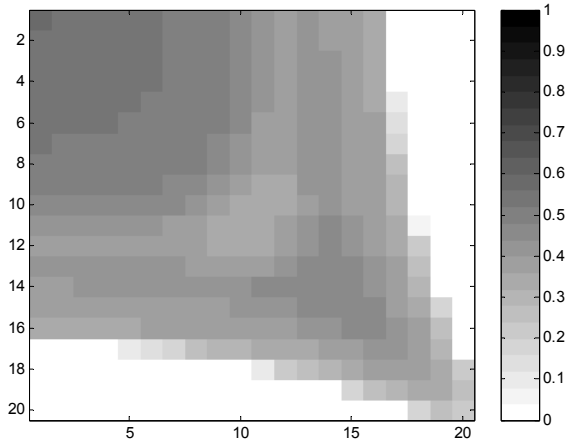

d) Second non-aqueous liquid.

Fig. 88 - Saturation profiles at 0.5 PVI for 2D homogeneous field WAG processes with a constant slug size (0.05 PV) and a WAG ratio of 0.5.

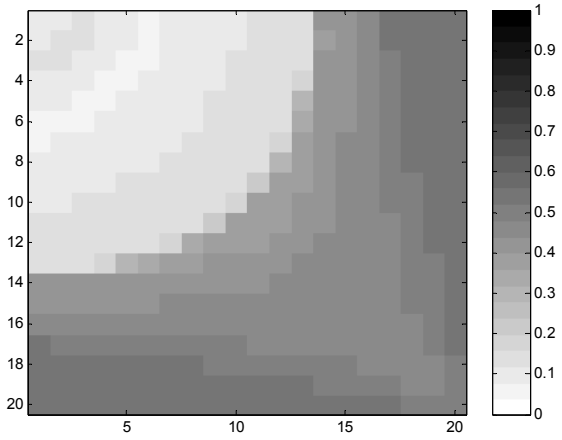

Fig. 89 - Oil saturation profiles at 0.5 PVI for 2D homogeneous field WAG processes with a constant slug size (0.05 PV) and WAG ratio = 4.

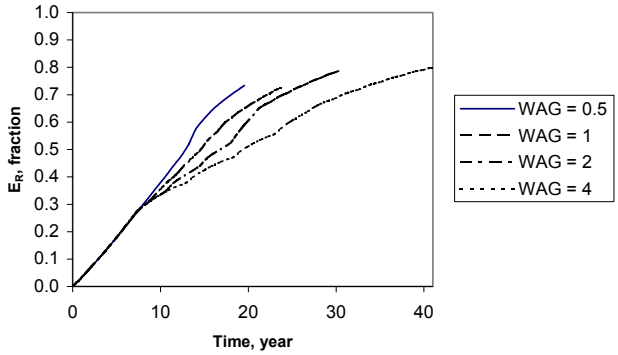

Fig. 90 - Oil recoveries for 2D homogeneous field WAG processes with a constant slug size (0.05 PV) and varied WAG ratios.

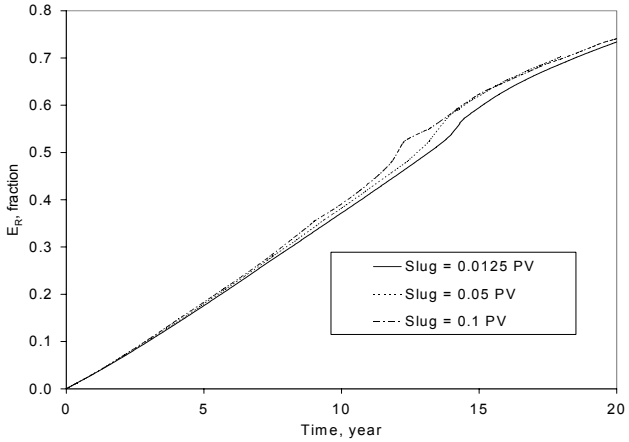

Fig. 91 - Oil recoveries for 2D homogeneous field WAG processes with a constant WAG ratio (0.5) and varied slug sizes.

Second, the effect of slug size on oil recovery was investigated. While WAG ratio was kept constant (0.5), slug size was varied: 0.0125 PV, 0.025 PV, 0.05 PV, and 0.1 PV. The total amount of solvent injected was kept at 0.5 PV in these simulations. The resulting oil recovery is shown in Fig. 91, which indicates that oil is recovered faster with increased slug size although the differences are not large. The increased oil recovery is due to the increase of solvent injected at a certain time as slug size increases.

Heterogeneous. By using a Dykstra-Parsons coefficient of 0.5, an average permeability of 250 md, and a dimensionless correlation length of 0.5, a heterogeneous permeability field was generated as shown in Fig. 92. Conditions other than permeabilities are the same as those used for the homogeneous cases, as shown in Table 20. Simulations for a constant slug size (0.05 PV) and varied WAG ratios (0.5, 1, 2, and 4) were run for this heterogeneous quarter five-spot. Results are shown in Fig. 93, which indicates that as WAG ratio increases, oil recovery decreases, similar to what was observed from the homogenous reservoir. Note that fluids are injected and produced faster in the heterogeneous field compared with the homogeneous field. The oil recoveries are, however, similar. The injected fluids find the higher permeability regions to move through the pattern faster than the homogeneous case.

The field simulations were run in 2D ignoring gravitational effects that are extremely important in these WAG floods. The spatial resolution is very low in the above simulations, thus leading to severe numerical dispersion. It is prohibitively time-consuming to run multi-dimensional, compositional simulations with four fluid phases on fine grids. Efforts are under way to speed up compositional simulations that can turn high-resolution simulation into reality.

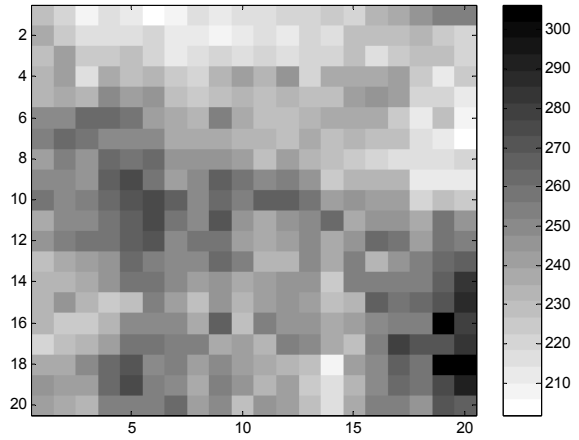

Fig. 92 - Permeability distribution for a heterogeneous reservoir.

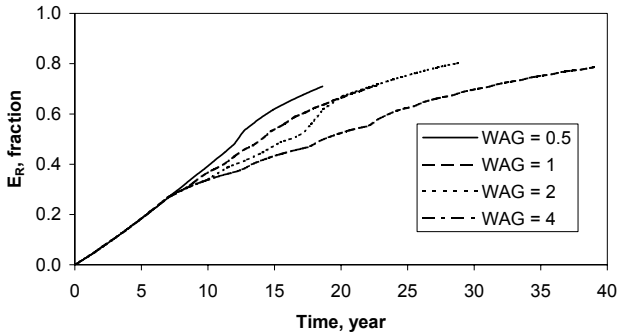

Fig. 93 - Oil recoveries for 2D heterogeneous field WAG processes with a constant slug size (0.05 PV) and varied WAG ratios.

Technology Transfer

The following papers have been presented (or to be presented) in conferences or in peer-reviewed journals.

Li, D. et al., "Compositional Simulation of WAG Processes for a Viscous Oil," SPE 84074, Proceedings of SPE ATCE, Denver, Oct. 5-8, 2003.

Kumar, K. et al., "Mechanism of Oil Wettability by AFM," AIChE Conference, San Francisco, Nov. 16-21, 2003.

Mohanty, K. K., "Challenges for Gas Injection Processes," Keynote Presentation, SPE ATCE, Houston, Sept. 26-29, 2004.

Bhambri, P. et al., "3-D Streamline Simulation of Adverse Viscosity Displacements," AIChE Conference, Austin, Nov. 7-12, 2004.

Kumar, K. et al., "AFM Study of Oil Reservoir Wettability," submitted to J. of Coll. & Interf. Sci. (2004).

Kumar, K. et al., "Atomic Force Microscopy Study of Wettability Alteration," SPE 93009, Proceedings of SPE Intl. Symp. on Oil Field Chemistry, Houston, Feb. 2-5, 2005.

We also presented the research results in the annual industrial reviews of the Institute for Improved Oil Recovery at the University of Houston from 2002-2004.

Conclusions

- 1D Compositional simulation results agree reasonably well with those of the slim tube experiments. Injection of CO2-NGL is preferable over that of PBG-NGL. MME is sensitive to pressure (in the range of 1300-1800 psi) for the injection of PBG-NGL, but not for CO2-NGL. Three hydrocarbon phases form in this pressure range. (Task 1)
- As the mean thickness of the adsorbed organic layer on minerals increases, the oil-water contact angle increases. The adsorbed organic films left behind after extraction of oil by common aromatic solvents used in core studies, such as toluene and decalin, are thinner than those left behind by non-aromatic solvents, such as cyclohexane. The force of adhesion for minerals aged with just the asphaltene fraction is similar to that of the whole oil. The force of adhesion for the minerals aged with just the resin fraction is highest of all the SARA fractions. (Task 2)
- A new relative permeability model for a four-phase system has been proposed. The new model can be used for mixed-wet formations. The new relative permeability model proposed in this paper is more conservative than the Guler *et al.* (2001) model in the prediction of oil recovery in 1D simulations, but not in 2D simulations. (Task 2)
- A streamline module is developed which can be incorporated in an existing finite-difference based compositional simulator to model water flood, gas flood and WAG flood. (Task 3)
- Horizontal wells increase well deliverability over vertical wells, but sweep efficiency can decrease. The well performance depends on the well length, position, heterogeneity, and viscosity ratio.(Task 4)
- The productivity increase due to electromagnetic heating is a function of power intensity, flow rate, and frequency etc. The productivity of a well can be doubled by electromagnetic heating. (Task 4)

- A high-pressure quarter 5-spot model has been constructed to evaluate the sweep efficiency of miscible WAG floods. WAG displacement reduces bypassing compared to gas floods and improves oil recovery in cores. As the WAG ratio decreased and slug size increased, oil recovery increased. Oil was recovered faster with increased slug size and decreased WAG ratio in the simulations for field cases studied. (Task 5)

References

Baker, L.E.: "Three-Phase relative Permeability Correlations," paper SPE 17369 presented at the 1988 SPE/DOE Enhanced Oil Recovery Symposium, Tulsa OK, April 17-20.

Batycky, R.P., "A Three-Dimensional Two-Phase Field Scale Streamline Simulator," Ph.D. Dissertation, Stanford University, Stanford, CA (1997).

Bidinger, C. R. & Dillon, J. F., "Milne Point Shrader Bluff: Finding the Keys to Two Billion Barrels," SPE 30289, International Heavy Oil Symposium, Calgary, June 19-21, 1995.

Blunt, M.J.: "An empirical Model for Three-Phase Relative Permeability", paper SPE 67950, *SPEJ* (Dec. 2000), 435-445.

Buckley, J. S. & D. L. Lord, J. Petrol. Sci. Eng. 39 (2003) 39, 261.

Capella, B. & G. Dietler, Surf. Sci. Reports 34 (1999) 1.

Chang, Y.-B.: "Development of Application of an Equation of State Compositional Simulator," Ph. D. Dissertation, the University of Texas at Austin, Austin, TX (Aug. 1990).

Craig, F.F., Jr., Geffen, T.M., and Morse, R.A., "Oil Recovery Performance of Pattern Gas or Water Injection Operation from Model Tests," *Trans.*, AIME, **204**, 7-15 (1955).

Delshad, M. and Pope, G.A.: "Comparison of the Three-Phase Oil Relative Permeability Models," Transp. Porous Media (1989) **4**, 59.

Fayers, F.J. and Mathew, J.D.: "Evaluation of Normalized Stone's Methods for Estimating Three-Phase Relative Permeabilities," *SPEJ* (April 1984) 225.

Fenwick, D.H. and Blunt, M.J.: "Network Modeling of Three-Phase in Porous Media," *SPEJ* (March 1998) 86.

Foerester, C. et al., "West Sak Field Development: Analysis of a Marginal Project," SPE 37946, *SPE Hyd. Econ. & Eva.*, Dallas, March 16-18, 1997.

Freer, E.M., T. Svitova, C. J. Radke, J. Petrol. Sci. Eng. 39 (2003) 137.

Guler, B. *et al.*: "Three- and Four-Phased Flow Compositional Simulations of CO_2/NGL EOR," paper SPE 71485 presented at the 2001 SPE Annual Technical Conference and Exhibition held in New Orleans, LA, Sept. 30-Oct. 3.

Hirasaki, G. J., Soc. Pet. Form. Eval. (June 1991) 217.

Jerauld, G.R.: "General Three-Phase Relative Permeability Model for Purdhoe Bay", *SPERE* (Nov. 1997), 255-263.

Khataniar, S. *et al.*: "CO_2 and Miscible Gas Injection for Enhanced Recovery of Schrader Bluff Heavy Oil," paper SPE 54085 presented at the 1999 SPE International Thermal Operations and Heavy Oil Symposium held in Bakersfield, CA, March 17-19.

Land, C.S.: "Calculation of Imbibition Relative Permeability for Two- and Three-Phase Flow from Rock Properties", *SPEJ* (June 1968) 149; *Trans.*, AIME, 243.

Meldrum, A. H. and Nielsen, R. F., "A Study of Three-Phase Equilibria for Carbon Dioxide-Hydrocarbon Mixtures," Producers Monthly, August 1955, 22-35.

Mohammed, R. A., A. I. Bailey, P. F. Luckham, S. E. Taylor, Colloids Surf. A 80 (1993) 223.

Mohanty, K.K. *et al.*: "Role of Three-Hydrocarbon-Phase Flow in a Gas Displacement Process," paper SPE 24115 presented at the 1992 SPE/DOE Symposium on Enhanced Oil recovery held in Tulsa, OK, April 22-24.

Mohanty, K. et al., "Role of Three-Hydrocarbon –Phase Flow in a Gas Displacement Process," *SPE Reservoir Engineering*, 214-221, August 1995.

Osako, I., Datta-Gupta, A., and King, M.J., "Timestep Selection during Streamline Simulation via Transverse Flux Correction. Paper SPE 79688 to be presented at the 2003 SPE Reservoir Simulation Symposium to be held in Houston, Feb. 3-5 (2003).

Peaceman, D.W.: "Representation of Horizontal Well in Numerical Reservoir Simulation," paper SPE 21217 presented at the 1991 SPE Symposium on Reservoir Simulation, Anaheim, CA, Feb. 17-20, 1991.

Penmatcha, V.R., Arbabi, S. and Aziz, K: "Effects of Pressure Drop in Horizontal Wells and Optimum Well Length", SPE 37494 presented at Production Operations Symposium, Oklahoma City, OK, 9-11 March 1997.

Pollock, D.W., "Semianalytical Computation of Path Lines for Finite-Difference Models," *Ground Water*, **26**, No. 6, 743-750 (1988).

Sahni, A., Kumar, M., and Knapp, R. B., "Electromagnetic Heating Methods for Heavy Oil Reservoirs," SPE 62550, SPE/AAPG Western Regional Meeting, Long Beach, CA, 19-23 June 2000.

Schneider, J., W. Barger, G. U. Lee, Langmuir 19 (2003) 1899.

Stone, H.L.: "Probability Model for Estimating Three-Phase Relative Permeability," *JPT* (Feb. 1970) 214; *Trans.*, AIME, **249**.

Stone, H.L.: "Estimation of Thee-Phase Relative Permeability and Residual Oil Data," *J. Cdn. Pet. Tech.* (1973) **12**, 53.

Van der Vegte, E. W. & G. Hadziioannou, Langmuir 13 (1997) 4357.

Van Dijke, M.I.J. et al.: "Three-Phase Flow in WAG Processes in Mixed-Wet Porous Media: Pore-Scale Network Simulations and Comparisons with Micromodel Experiments," paper SPE/DOE 75192 presented at the 2002 SPE/DOE Improved Oil Recovery Symposium, Tulsa, OK, April 13-17.

Yang, S. Y., G. J. Hirasaki, S. Basu. R. Vaidya, J. Petrol. Sci. Eng. 24 (1999) 63.